IMPROVED DROUGHT EARLY WARNING AND FORECASTING TO STRENGTHEN
PREPAREDNESS AND ADAPTATION TO DROUGHTS IN AFRICA
DEWFORA

A 7th Framework Programme Collaborative Research Project

Implementation of improved methodologies in comparative case studies

Final report for the Eastern Nile case study

WP6-D6.2
July 2013

Coordinator:	Deltares, The Netherlands
Project website:	www.dewfora.net
FP7 Call	ENV-2010-1.3.3.1
Contract no.	265454

Page intentionally left blank

DOCUMENT INFORMATION

Title	Final report for the Eastern Nile case study
Lead Author	NFC
Contributors	DCER, GFZ, JRC
Distribution	CO: Confidential, only for members of the consortium (including the Commission Services)
Reference	WP6-D6.2

DOCUMENT HISTORY

Date	Revision	Prepared by	Organisation	Approved by	Notes
13/05/2013		Alaa Eldin	NFC		
13/05/2013		Modathir Zaroug	DCER		
14/05/2013		Mathias Seibert	GFZ		
16/06/2013		Alaa Eldin	NFC		
18/06/2013		Modathir Zaroug	DCER		
20/06/2013		Mathias Seibert	GFZ		
28/06/2013		Gustavo Naumann	JRC		
11/07/2013		Alaa Eldin	NFC		

ACKNOWLEDGEMENT

The research leading to these results has received funding from the European Union's Seventh Framework Programme (FP7/2007-2013) under grant agreement N°265454

Page intentionally left blank

SUMMARY

Drought is one of the greatest natural hazards which affect many sectors and systems with major impacts on agriculture, water resources and natural ecosystems. Drought conditions are much more difficult to identify than other natural hazards because drought is commonly the result of a number of factors that are only apparent after a long period of precipitation deficit. Drought is often classified into four types: meteorological, agricultural, hydrological, and socioeconomic. Droughts are a normal part of climate variability for virtually all regions.

The Eastern Nile Region covers a large portion of the Nile Basin encompassing three major sub-basins of the Nile: the Sobat, the Blue Nile, and the Atbara in the north. Together, the contribution of the three sub-basins to the total annual Nile flow is about 85%. There are some organizations in the Eastern Nile countries (Ethiopia, Sudan, South Sudan and Egypt) which are responsible for drought management whether in drought prediction or in adaptation to the consequences of drought events.

In the study area, there are models which could be useful in studying the droughts from the meteorological and hydrological perspectives. This case study aims to test the available tools and provide improved tools for forecasting droughts and hence water availability in the region. The study will focus on the Blue Nile and Atbara River basins, and will pay particular attention to the expected effects of climate change on drought hazard. A number of statistical analyses of the teleconnections between climatic indices and precipitation as well as runoff is also performed. The case study is led by the Nile Forecast Center (NFC) with contributions from DCER (already active in the region), GFZ, and JRC.

Drought indices are typically single numbers that are calculated including observed and proxy data related to rainfall, soil moisture, or water supply and provide a comprehensible synthesis of a situation for the decision maker that may be more useful than raw data. The use of a particular index to characterize drought depends on the objectives of the analysis, the study region, and the availability of data. Most water supply planners find it useful to consult one or more indices before making a decision.

For assessing meteorological drought, the Standardized Precipitation Index (SPI) has been applied to three “observed” rainfall datasets to assess its applicability in the study area. These are the Climatic Research Unit (CRU) rainfall dataset, the ECMWF Rainfall Reanalysis dataset (ERA40), and the gauge-satellite merged rainfall dataset produced by the Nile Forecast System (will be referred to as the NFS dataset). The historical study period in 1961-1990 or beyond has been selected (except for the NFS dataset which starts in 1992). Future rainfall is taken from an ensemble of 6 dynamically downscaled climate simulations

for the period 2021-2050 performed using the PRECIS regional climate model. The SPI has been calculated for different lead times from 1 month to one year.

The analysis shows that ERA40 rainfall is overestimated for the Eastern Nile region compared to CRU and NFS rainfall datasets for the early part of the record, distorting the rainfall distributions, and to a lesser extent the SPI distributions. CRU rainfall is higher than NFS for the region during the peak rainfall period, and thus has higher flood probabilities but similar drought probabilities. When PRECIS is run using ERA40 boundary conditions (which do not include precipitation), it overestimates rainfall over the whole year, resulting in different seasonal rainfall distributions compared to ERA40 rainfall. This has its effect on the SPI as some dry years may be seen as wet and vice versa. Such biases need to be corrected, but their effect is somewhat reduced in calculating SPI because it involves normalization of rainfall distributions.

The current set of climate simulations indicate a general increase in rainfall over the region but this does not exclude the increase of drought probability for some lead times especially longer ones and on the scale of the hydrologic year. The uncertainty bandwidth (defined by the range across the different simulations) increases near the ends of the SPI probability distributions but not for all lead times.

The SPI proved to be a useful way to characterize meteorological drought across different catchments and at different time scales. Because it normalizes the rainfall distribution, it is less sensitive to systematic biases in the data (i.e. systematic overestimation or underestimation – shifts in the mean).

In terms of hydrological drought, a set of three indices has been applied to observed as well as simulated and forecasted flows using the Nile Forecast System (NFS) hydrological and forecasting components respectively. This helped assessing the applicability of these indices and evaluating the NFS in predicting drought.

The first of these indices is the drought classification of the Ministry of Water Resources and Irrigation (MWRI) of Egypt which was developed by the Nile Yield Committee in 2010 based on different ranges of natural flow of the Nile at Aswan. The classification has been extended to other important stations on the Blue Nile and the Atbara by considering the average irrigation abstractions in Sudan and the contribution of those basins to the flow at Dongola. The classification has been applied to observed and forecasted flow records for the Blue Nile at Khartoum and Diem and for the Atbara at its mouth near Atbara town. The results show that the MWRI classification has been successfully adjusted for the application to the selected sub-basins. However, the small flow range of the Atbara has resulted in small bounds for the categories which make it difficult to get the right drought characterization. The results show a general agreement of drought classification between observed and forecasted flows for the Blue Nile but with some discrepancies for some years. The results for the Atbara have more discrepancies indicating that the hydrological model or forecasting parameters of the Atbara basin need to be revisited.

The second index used is the Surface Water Supply Index (SWSI) which combines hydrological and climatic features in a single index and allows for the consideration of reservoir storage. The revised SWSI is computed using expected streamflow and initial reservoir storage only, which is more advantageous than the original formulation which required weights for the different hydrologic components (snowpack, precipitation, streamflow, and reservoir storage). The revised SWSI has been calculated for the Blue Nile and Atbara Basins using forecasted streamflows starting for the period May 1992 - October 2011 by using the median ESP (Ensemble Streamflow Prediction) forecast. The forecasted flow was accumulated from the first of May till the end of October for each year (to get the flow forecast over the season). The period May-October denotes the rainy season for the Eastern Nile basins. This flow forecast is added to the actual storage in reservoirs at the end of April for both the Atbara and Blue Nile basins.

The results have not reflected the actual situation of the flood season for some years for both sub-basins but the results for the Atbara are worse than those of the Blue Nile because of the reduced forecast quality for that basin compared to the Blue Nile. Flow forecast values need to be corrected to enhance the results of the SWSI values. In addition, longer records need to be used because SWSI values are a function of the probability of non-exceedance which is obtained based on the rank of the year.

The third index used in the Standardized Discharge Index (SDI) which is very similar to SPI but uses the streamflow instead of precipitation. The SDI has been calculated using the observed discharge time series, NFS simulated flow, and the median of ESP forecasted flow. The simulated and forecasted SDI at Atbara in many years did not have the same direction of the observed SDI, indicating that the hydrological model of Atbara should be calibrated and it is clear that the bad simulation of Atbara could be the reason for the poor results of the ESP used to calculate SWSI above. The results of the Blue Nile at Diem and Khartoum show that the observed SDI, Simulated and forecasted SDI have the same sign for most years.

The impact of sea surface temperature (SST) in the Pacific Ocean (Nino 3.4 region) on droughts and floods was investigated in the upper catchment of the Blue Nile. Discharge measurements (1965-2011) at the outlet of the upper catchment of the Blue Nile in relation to the El Niño index were analyszed. Regarding the teleconnections between ENSO and rainfall, the important conclusion is that JJAS rainfall in the upper catchment of the Blue Nile is highly sensitive to the sea surface temperatures (SST) in the early season of AMJ in Niño 3.4. Additionally, the performance of the regional climate model RegCM4.1 was tested for a 28 years period (1982-2009). The model succeeds in reproducing the observed negative correlation between Pacific SST and the Blue Nile flow, and in particular the high correlation with El Nino that start during (April-June) period. We propose that observations as well as global models forecasts of SST during this season should be used in seasonal forecasting of the Blue Nile flow.

A wavelet analysis applied to the runoff and the Oceanic Niño index showed that the two time series share signal properties of longer periods of ca. 16 years. Shorter periods are also common to both series but non-stationary. Both signals are linked but the non-stationarity can be an obstacle for statistical seasonal prediction. Nevertheless a statistical approach was followed to investigate the forecasting quality which can be achieved by building solely upon teleconnections of sea surface temperatures to model runoff in the Blue Nile at the station in Khartoum. Three different forecasting schemes were set up with statistical models for the Blue Nile station in Khartoum. The best forecasting skill was achieved for one month ahead forecasts of runoff in the late rainy season from September to November. The predictability for June to August runoff was lower than for September to April in this study.

Page intentionally left blank

TABLE OF CONTENTS

LIST OF FIGURES

LIST OF TABLES

Page intentionally left blank

1. INTRODUCTION: EASTERN NILE BASIN CASE STUDY

Drought is one of the greatest natural hazards, with effects on many sectors and systems, and major impacts on agriculture, water resources and natural ecosystems. Droughts affect many people worldwide, are responsible for famine, epidemics and land degradation in developing countries (Obasi, 1994; Nicholson, 2001), and cause large economic losses in developed regions (Meehl et al., 2000; Fink et al., 2004; UN, 2008). Drought is a natural phenomenon that occurs when water availability is significantly below normal levels over a long period, and cannot meet demand (Redmond, 2002).

Drought conditions are much more difficult to identify than other natural hazards because drought is commonly the result of a number of factors that are only apparent after a long period of precipitation deficit. Drought differs from other natural hazards in that it has a slow onset, evolves over months or even years, affects a large spatial region, and causes little structural damage. Its onset and end, and the severity of drought are often difficult to determine (Wilhite, 1993). In contrast to other natural hazards including floods, which are typically restricted to small regions and occur over well-defined temporal intervals, drought is difficult to pinpoint in time and space because it affects wide areas over long time periods. Moreover, it is very difficult to objectively quantify drought severity, which is a combination of the duration, magnitude and spatial extent (Dracup et al., 1980).

Drought is often classified into four types: meteorological, agricultural, hydrological, and socioeconomic. Meteorological drought refers to a precipitation shortage from average; agricultural drought results when the precipitation shortage results in a deficit of soil moisture and therefore produces agricultural impacts derived from the water deficit in the vegetation; hydrological drought results when the deficit in precipitation extends to large periods and therefore there is a shortfall on surface or subsurface water supply. Finally, socioeconomic drought is often referred to when the deficit precipitation or water shortage has an impact on the economy and society.

Droughts are a normal part of climate variability for virtually all regions. The Eastern Nile region is no exception. This region, as most of Nile sub-catchments, exhibits large climatic variability that results in even larger hydrological variability. The high variability leads to high exposure to floods and droughts. Coupled with low adaptive capacity in terms of socio-economic systems and infrastructure, the region is highly vulnerable to floods and droughts. Droughts have led to famine in several occasions in Ethiopia.

1.1 THE EASTERN NILE BASIN

The Eastern Nile Region covers a large portion of the Nile Basin (Figure 1-1). The region encompasses three major sub-basins of the Nile: the Sobat in the south, the Blue Nile in the middle, and the Atbara in the north. Together, the contribution of the three sub-basins to the total Nile flow is about 85%. Most of that flow is generated in the Western Ethiopian highlands during the rainy summer season (July-September) with some minor contribution to the Sobat from South Sudan. The Eastern Nile region is characterized by heavy rainfall (up to 1800mm/year) and steep slopes in the headwater areas of the mountains and less rainfall and mild slopes in the Sudanese plains near the outlets of the three rivers. In this study, the focus is on the Blue Nile and the Atbara sub-basins which are described briefly in the coming sections in terms of their hydrology, climate, and water resources utilization.

1.1.1 The Blue Nile Basin

The Blue Nile (Figure 1-2) has a total catchment area of about 314,000 km^2. The river and all of its tributaries rise on the Ethiopian Plateau at elevations of 2,000 to 3,000m a.m.s.l. The average elevation is about 2,400 m with peaks up to 4,200 m. The main source of the river is generally considered to be a small spring at Gish Abbay at an altitude of approximately 2,744 metres flowing into the Little (or Gilgel) Abbay, which flows into Lake Tana. Lake Tana has a water area of 3,000 km^2 and a catchment area of 15,082 km^2. The average rainfall and evaporation over the lake balance each other at 1,300 mm and the annual lake outflow is about 3.93 BCM (1920-1933 – Shahin, 1985). The hydrograph at the exit of Lake Tana has one peak in September.

The Blue Nile leaves Lake Tana and flows to the south east in a large circle for about 935 km before reaching Roseires in Sudan near the border between Ethiopia and Sudan. The slope of the river changes drastically upon entering Sudan from 1.6 m/km to 15 cm/km. The Roseires river gauge was moved upstream to Diem after the construction of the Roseires dam in 1961. The river receives several tributaries on its way from Lake Tana to Roseires, which increase the flow tenfold. The total basin area up to Diem is about 182,000 km^2 with annual average rainfall and PET (Potential Evapotranspiration) of 1,166 mm and 1,427 mm respectively. The mean discharge at Roseires/Diem for the period 1940-1982 is about 49.5 BCM. The hydrograph at Roseires still has one peak, but this time it occurs in August. The river continues its journey to Sennar at a much milder slope for another 270 km where rainfall reaches 460 mm. There are no tributaries in this reach; therefore the flow at Sennar is about 2 BCM less than that at Roseires.

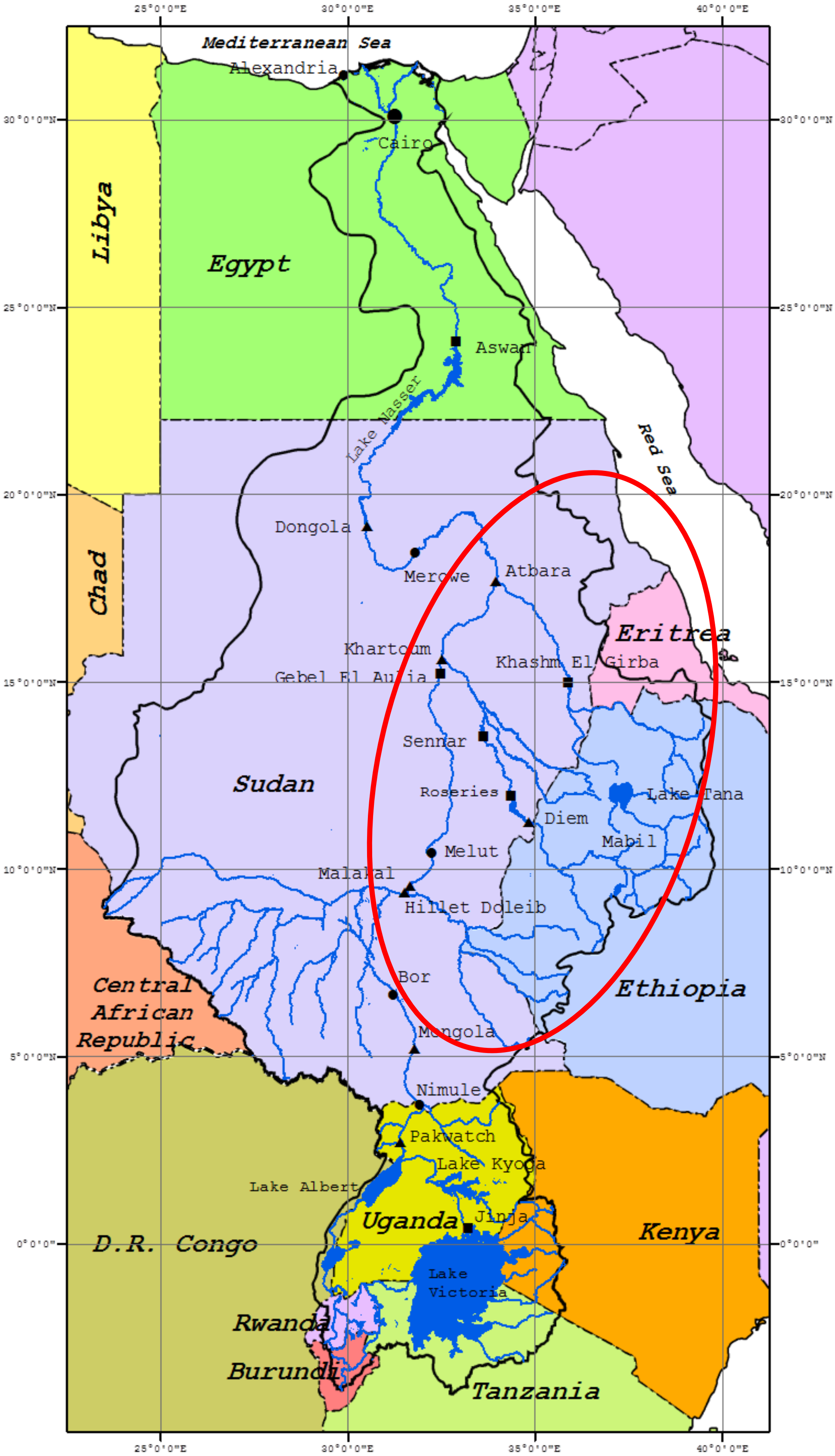

Figure 1-1 Nile Basin Map - Eastern Nile Region Marked

Between Sennar and the basin outlet to the Nile at Khartoum, the Blue Nile receives two major tributaries, the Dinder and the Rahad. Both of these rivers originate in the Ethiopian Highlands. The Dinder has a drainage basin of 16,000 km^2 while the Rahad has a smaller catchment of only 8,000 km^2. Both tributaries run dry during the winter/spring months (January to May). The mean annual precipitation and PET for the Blue Nile basin between Diem and Khartoum are 521 mm and 2,157 mm respectively. The observed flow record at Khartoum has an average annual of 46 BCM. This is less than that at Diem because the irrigation diversions along the reach and losses from the Roseires and Sennar reservoirs outweigh the contributions of the Dinder and the Rahad.

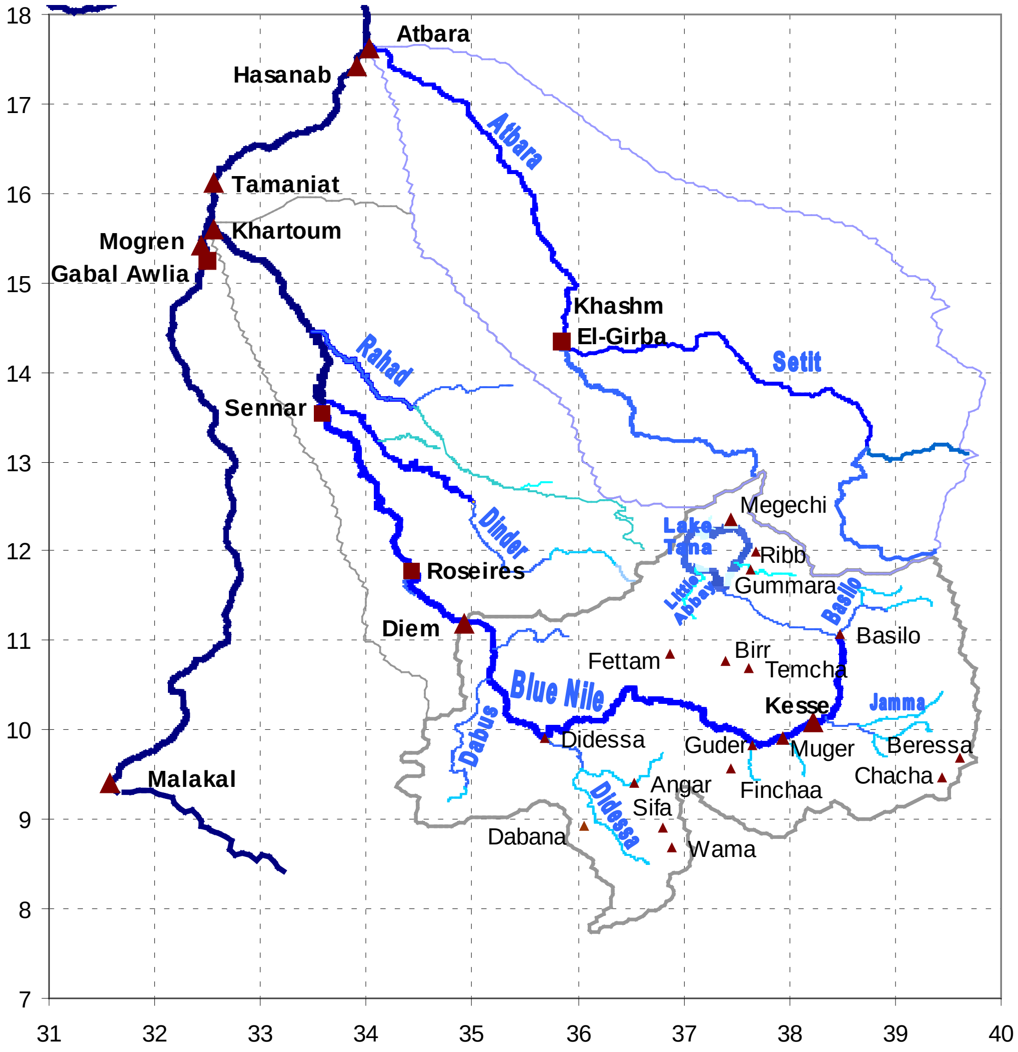

Figure 1-2 Map of the Blue Nile and Atbara Basins

The climate in the basin varies from humid to semi-arid and is mainly dominated by latitude and altitude. This is reflected in the high variability of local climates, ranging from hot and arid in Sudan to temperate at the highlands and even humid-cold at the mountain peaks in Ethiopia. Within the Blue Nile Basin, there is significant variability in terms of sub-catchment sizes, slopes, climatic patterns, topography, drainage patterns, geological formations, soils and vegetation. In general, three broad topographical divisions are identifiable: the highland plateau, steep slopes adjoining the plateau that tilt to the west and the western low lands with gentler topography comprising the remainder of the Basin. The Blue Nile Basin hydrology is characterised by seasonal and annual variability, very steep catchment and channel gradients and rapidly eroding watersheds, which result in very high sediment loads. This is exacerbated by poor agricultural practices, overgrazing and deforestation. The dominant land cover in the Blue Nile Basin is rainfed agriculture. Wood and shrubland are minor compared to the other land cover types (Teferi et al., 2010). The dominant soil texture of the Basin is clay. The soil type in the basin is dominated by Alisols and Leptosols, followed by Nitosols, Vertisols and Cambisols. The Nitisols are deep non swelling clay soils with favourable physical properties like drainage, workability and structure, while the Vertisols are characterized by swelling clay minerals with more unfavourable conditions. The basin geology is characterized by basalt rocks, which are found in the Ethiopian highlands, while the lowlands are mainly composed of basement rocks and metamorphic rocks such as gneisses and marbles (ENTRO, 2007).

Currently, there is limited irrigation in Ethiopia around Lake Tana and along the Beles tributary as most agriculture depends on rainfall. There are some proposed irrigation schemes on some of the Blue Nile tributaries and around Lake Tana. The largest irrigation scheme in the Blue Nile basin is the Gezira-Managil Scheme in Sudan with an area of about 8000 km^2.

There are currently two major dams on the Blue Nile supplying water for irrigation and hydropower. These are the Roseires and Sennar dams in Sudan. The Roseires Dam downstream of El Diem was completed in 1966 and was heightened very recently (2012). Before heightening, it had a full supply capacity of 2100 million m^3. Roseires is operated primarily for hydropower but also to supplement irrigation demands downstream in case of need. It has an installed power capacity of 280 MW. The Sennar Dam downstream of Roseires was built in the 1920s and is used primarily for irrigation of the Gezira and Managil irrigation schemes. Two canals from Sennar Dam supply water to the schemes. Sennar dam also generates hydropower with an installed capacity of 15 MW.

Releases are made from Roseires to Sennar in order to maintain the water level in Sennar for irrigation supply to the Gezira and Managil canals. At present Roseires is operated to maintain electrical supply from the dam, although the storage is also reduced in July and August to try to reduce the rate of sedimentation in the dam. The dam is allowed to start filling at the earliest at the beginning of September or when the flow at dam drops to 350 Million m^3/d or at the latest on the 26th September and fill for 26 days.

In Ethiopia, there are few and more recent hydropower plants. These include the Beles Hydroelectric Power Plant, sometimes referred to as Beles II or Tana-Beles, which is a run-of-the-river hydroelectric power plant in Ethiopia near Lake Tana. The power plant receives water from the lake and after utilizing it to produce electricity; the water is then discharged into the Beles River. The plant will eventually have an installed capacity of 460 MW and when fully operational and will be the largest power plant in the country. It is also expected to help provide water for the irrigation of 140,000 ha (350,000 acres) It was inaugurated in May 2010.

Below the natural outlet of Lake Tana, the Tis-Abbay hydroelectric power plants are located on the Abbay River (Abbay is the Blue Nile in the Ethiopian Amharic language) where the head of the Tis Issat Falls has been used to generate electricity since 1964. Tis-Abbay I has an installed capacity of 11 MW and Tis-Abbay II has increased the installed capacity at this location to 73 MW.

In addition, the Fincha'a Dam on the Fincha'a River, a tributary of the Blue Nile has an installed capacity of 128 MW. It was constructed in 1973 and is now also connected to the Amerti River via a tunnel.

Currently, the Grand Ethiopian Renaissance Dam is under construction near the Ethio-Sudanese border with a capacity of about 74 BCM and installed hydropower capacity of 5,250 MW. When completed, it will be the largest on the Blue Nile in terms of storage and the largest on the Nile in terms of hydropower production. Several other "mostly" hydropower dams along the main Blue Nile and on some of its tributaries are also proposed and some were studied to the pre-feasibility level.

1.1.2 The Atbara Basin

The River Atbara is the last tributary that joins the Nile. It originates in the Ethiopian Highlands to the north of Lake Tana. There is little consensus upon the area of the Atbara basin. Hurst (1959) reports an area of 100,000 km^2 which is taken forward by Shahin (1985) and Sutcliffe and Parks (1999), while Conway and Hulme (1993) reported a larger area of about 137,000 km^2. Recent estimates using GIS delineation techniques based on recent digital elevation models gives an extremely larger area of more than 200,000 km^2. The River Setit (called Tekeze in Ethiopia), the major tributary to Atbara, has a catchment area of 68,000 km^2 (Hurst, 1950). The upper basin (including the Setit) area is about 148,000 km^2 and has an average annual rainfall and PET of 556 and 1,774 mm respectively. The area of the lower basin is about 61,000 km^2 and has a low rainfall of 208 mm and a higher PET of

2,313 mm. The total annual contribution of the Atbara, as measured at its mouth near the junction with the Nile is 10.95 BCM (1940-1982 average). All of this flow comes from the upper basin as the lower reach is a source of loss due to the high evaporation rate and due to irrigation diversions and losses from the reservoir of Khashm El-Girba dam. The hydrograph of the Atbara is almost triangular with a very high peak in August and almost zero flow during January till May in most years.

Extreme variations in the climatic conditions exist across the Atbara-Tekeze river basin. While the average monthly temperatures are in the range of 12°C to 18°C in the highlands the monthly average at the confluence with the main Nile is more than 29°C with minimum and maximum temperatures from 5°C to 46°C. The rainfall varies from 1500mm on the highlands to 500mm at the Ethiopia/Sudan border and to less than 100mm at the confluence with the main Nile. The rainy season extend over 8 months on the highlands to 5 months at the border, but is mainly concentrated in the period June to September.

There are two dams on the Atbara: TK5 on the Tekeze (Setit) tributary in Ethiopia with a capacity of 9 BCM inaugurated in 2009, and Khashm El-girba dam (1964) on the Main Atbara in Sudan with a design capacity of 1.3 BCM but dropped to almost half of that due to sedimentation. The TK5 has a hydropower capacity of 300 MW. The TK5 reservoir is operated primarily for hydropower and the water is available for irrigation projects in the surrounding area. Because of the large storage capacity of the TK5 reservoir compared to river yield, regulating the releases from the dam can provide a high reliability of supply for hydropower and for downstream irrigation schemes.

Khashm El-Girba is a multipurpose reservoir which supplies irrigation water through a canal system to the New Halfa Scheme (190,000 ha) and also generates a small amount of hydropower (18.2 MW turbine capacity). The Khashm El-Girba reservoir is drawn down to almost empty before the high flow season in order to reduce sediment build up.

On the Ethiopian side of the Tekeze basin, the arable land is mostly situated in the border zone with an identified potential of over 70,000 ha. Around 135,000 ha irrigation area is planned under the Upper Atbara Project in Sudan. In Sudan land resources is not a limitation.

The nature of the topography in Ethiopia offers several dam sites for minor to large scale hydroelectric power generation and multipurpose use. The rainfall is poorly distributed over the year with 70% in the months of July to Oct. Seasonal storage in dams would be necessary for hydropower generation and multipurpose use. Adequate survey of the topography and hydrometrical records would reveal the full extent of the hydropower potential of the basins. This could be combined with the purposes of river regulation, sedimentation reduction, and creation of livelihood and protection of the watershed. The long term harnessing of the river could possibly include a cascade like series of several dams with regional power interconnection programs and irrigation opportunities.

1.2 DROUGHT MONITORING AND MANAGEMENT WITHIN THE BASIN

There are some organizations in the Eastern Nile countries (Ethiopia, Sudan, South Sudan and Egypt) which are responsible for drought management whether in drought prediction or in adaptation to the consequences of drought event. Some of these organizations are important to this study in one or more of the main three prospective: agriculture, water resources and human health. Some of them focus only on drought monitoring and early warning while others aim to provide aid to mitigate drought impacts in affected regions. In the next section, the main organizations and their main mandates will be explained stressing the drought-related activities for each.

1.2.1 Ethiopia

Contingency Planning and Financing Committee of the Somali Region

Also known as Disaster Prevention and Preparedness Committee (DPPC), it is currently mandated with contingency planning that involves food and non-food sectors, consider the effects of food crises like increased incidence of diseases, and that would consider mitigation and recovery interventions to ensure the continued development of a more robust emergency response system is in process. Some agencies working in Ethiopia have contingency plans for their own operations. For example Oxfam international has a drafted a contingency plan for humanitarian operation in Ethiopia. There are also contingency plans of agencies for specific areas like the contingency plan for Somali Region that was initiated by a multi-agency team working in the Region and supported by UNDP in 1997.

Under the umbrella of the committee of the Somali Region in Ethiopia, in many seriously drought affected areas of the country, especially in the lowlands of Somali region and Borena Zone of Oromiya region, there is little alternative to the emergency tankeing of water from permanent sources of water to where people have congregated. Tankering operations need to be supported with the provision of storage and delivery systems. The repair and rehabilitation of boreholes is feasible in some areas and also needs support.

The DPPC has a lot of activities in related to human health protection and quality; some of these activities are as follows:

- **Migration and Population Tracking:** A mechanism for tracking and monitoring migratory movements in order to understand the determinants to displacement is urgently needed. The data and findings thus generated can be applied to design interventions and to optimize the allocation of resources to areas with urgent needs.
- **Emergency Education:** Three years of poor rains have placed a serious economic burden on many poor rural families. In drought-affected areas, school attendance has been low and drop-out rates have been accelerating. The aim is to assist children whose parents might not otherwise be able to afford to send their children to school.
- **Special Protection Needs of Women and Children:** The severe drought in the Somali region, in particular, has led to the migration of at least 10,000 people in the Gode area. The most vulnerable segments of the displaced population, especially women and children, have a greater need for special help under such circumstances.
- **Shelter and Logistics Requirements:** The migration of communities in search of water and food significantly increases the risks associated with exposure to wind, sun and rain. The aim is to mitigate the effects of exposure, and to provide some basic household requirements to the most vulnerable families.

One of the main components of the National Disaster prevention and preparedness commission (DPPC) in Ethiopia is an early warning system (EWS) which has been in place since 1976 to monitor and warn against the threat of disasters ahead of time, and to trigger timely, appropriate, and preventative measures. It monitors closely factors which affect food security at household, regional and national levels.

The system is an inter-agency activity involving different relevant government institutions. It is led at the national level by a committee with the DPPC acting as its secretariat. Since 1993, The EWS has been decentralized in line with the regionalization policy and bottom-up planning approach. Training in data collection for early warning and analysis has been given to functionaries at regional and lower levels.

As part of the regular activity of the program, all relevant indicators of food security are monitored on a monthly basis culminating in an annual nation-wide pre and post-harvest crop assessments. Pastoral assessments are also carried out in the livestock dependent regions, while disaster assessments are conducted in an emergency situation.

Early warning reports are regularly issued to Government, donors and the international community. Efforts are now underway to improve the system through the introduction of enhanced methodologies, and tools for data analysis. The system enhancement work which is in progress focuses on six major components: The monitoring of national food security, and crop, livestock, market and agro-metrology assessments.

The DPPC has now evolved to be the Early Warning and Response Directorate (EWRD) which is also through PSNP and under DRMFSS, provides accurate and timely early warning information for the PSNP Risk Financing (RF) (see Section 0) and ensures adequate linkages between PSNP RF and other humanitarian response activities. The EWRD is responsible for the timely delivery of food resources.

1.2.2 Relief and Rehabilitation Commission

The relief and rehabilitation commission (RRC) was established in 1974 (RRC, 1984). It was set up to organize and coordinate government's relief and rehabilitation measures for the millions of people affected by the 1973/74 famine. The awkward manner in which RRC was created, the magnitude of tasks (reaching out millions of victims, inexperienced and unprepared staff, archaic government bureaucracy with little skills in sheltering victims, warehousing, stockpiling and emergency operations), the rampant corruption inherent in the administrative system and absence of a clear policy and/or legal framework had all operated to undermine disaster management efforts. A tumultuous social and political milieu coupled with a series of disaster situations never allowed sufficient breathing space to look towards a coherent, integrated and comprehensive DM system. The arrival of another famine in 1983/84 made the work of the agency (RRC) all the more intractable.

Absence of coordinated and integrated prevention, preparedness and response effort between central government and local government institutions on the one hand, and RRC and line ministries on the other were the major predicaments facing the EDM system (PDRE, 1989). Lack of organized information system and planned logistical support undermined the post-disaster response and recovery efforts of the agency, let alone thinking strategically towards mitigation and preparedness measures. This trend during the period from 1974 to 1989, therefore, the disaster management machinery in Ethiopia heavily invested in response and recovery rather than in preparedness and prevention.

Productive Safety Net Program

The PSNP was established as a government led program where government systems and personnel implement the activities with coordinated donor support. The objective of the

PSNP is to span the mandates of two Ministries and multiple departments within each Ministry.

The Ministry of Agriculture and Rural Development (MOARD)

In Ethiopia, the MOARD is responsible for the management of the PSNP, with the Disaster Risk Management and Food Security Sector (DRMFSS) responsible for overall program coordination. Within the DRMFSS, the Food Security Coordination Directorate (FSCD), previously called the Food Security Coordination Bureau, facilitates the day-to-day management and coordination of the PSNP. It is directly responsible for the timely delivery of transfers to beneficiaries and supports the implementation of public works.

For drought affected farmers in the central highlands of Ethiopia, assistance is needed in the form of seeds. In some areas small-scale irrigation can be supported through the provision of pumps. Lowland farmers in the Somali region, especially those living along the permanent rivers (in Gode, Liben and Afder zones) also need help with seeds, farm tools and irrigation pumps. Livestock and pastoralists in the drought-affected lowlands of Somali region, the Borena zone of Oromiya and South Omo Zone of the SNNP region are also being targeted for special emergency assistance. The provision of feed for animals, the provision of adequate veterinary services in the drought affected areas, and the establishment of slaughter facilities for the preparation of dried meat are all elements of the planned programme.

Through the PSNP in Ethiopia, the Natural Resource Management Directorate (NRMD) NRMD is responsible for coordination and oversight of the public works. This includes capacity building and technical support, supervision of environmental guidelines, liaising with FSCD and other PSNP partner institutions on coordination and management of public works, and participation in PSNP design and management forums, including policy issues and the roll out of the pastoral PSNP. The Ministry of Finance and Economic Development (MOFED) oversees financial management of the program and disburses cash resources to implementing federal ministries and to the regions based on the annual plan submitted by MOARD.

National Meteorological Services Agency (NMSA)

The agency has started as a small Meteorological unit which was established in 1951 within the Civil Aviation department (now Civil Aviation Authority) to deliver only the needed data for aeronautical purposes. Thirteen years later and due to more requests for meteorological information the unit was promoted to be the Meteorological Department under the auspices of civil Aviation Authority. The National Meteorological Services Agency is responsible for the control and operations of short-medium-and long-range forecasts and early warnings. The NMSA Develops ways and means for adopting new systems, better techniques and simplified procedures so as to render an efficient and effective weather forecast services.

The NMSA prepares and disseminates Agro-Meteorological Advisory Bulletins on a real-time basis, which can assist planners, decision makers and farmers at large. The agency disseminates agro meteorological reports on ten daily, monthly and seasonal in which all the necessary current information relevant to agriculture is compiled. NMSA also issues agro-meteorological bulletins through World Agro Meteorological Information Service Web site. The government decision-makers are using their recommendations to alter agricultural practices on relatively short notices in order to maximize the value of the forecasted rains and minimize the impacts of forecasted droughts (Nicholls & Katz, 1991).

1.2.3 The Sudan (including South Sudan)

Sudan Meteorological Authority

The Sudan Meteorological Authority (SMA) is a governmental body working on monitoring, forecasting of weather parameters and it is considered as an advisor for policy makers in all issues about climate and weather. The SMA also provides data and information for the public and for scientific researches and also work as consultants for some organizations and companies.

Desertification Research Institute, Sudan (DRI)

The research focuses on two axis: Socio-economic and Basic and Applied research to achieve the institute objectives which are: Formulation and execution of basic and applied research in dry and desertified lands putting livelihood in top agenda; Applied research to develop drought and disease resistant crops and improve productivity and dissemination of research results and developed techniques.

Institute of Environmental Studies

The institute of Environmental Studies (IES) has special interest and experience in educational and research in monitoring, environmental awareness and how the community's response to drought.

1.1.1 Egypt

After the completion of the High Aswan Dam in the late 1960s, Egypt became protected to a large extent from flood and drought risks. As Egypt depends mainly on the river Nile to provide most of its water supply and because rainfall in limited and unreliable, drought forecasting and management in Egypt focus on hydrological drought and is mainly taken care of the Ministry of Water Resources and Irrigation (MWRI).

Nile Forecasting Centre

The general aim of the centre is to provide tools and information for water planning and management. To this end, the Nile Forecast Centre through various tools including the Nile Forecast System (NFS) will provide to planners and decision-makers in Egypt with:

- Timely forecasts of the Nile River inflows into the High Aswan Dam reservoir;
- Real-time information about hydrological and meteorological processes occurring in the whole Nile Basin; and
- Assessment of climate change and future development impacts on the flow regime of the Nile.

The information available from the NFC is only internally published to the different departments in the Ministry of Water Resources and Irrigation (MWRI) in Egypt and most importantly to the Nile Yield Committee.

Nile Yield Committee

This a standing committee within the Ministry of Water Resources and Irrigation with representatives from the Nile Water Sector (NWS), the Nile Forecasting Center, the High Aswan Dam Authority (HADA), the Irrigation Sector and other sectors and research institutions of MWRI. It meets on a monthly basis, or more frequently as circumstances demand, especially prior to and during the flood season to review the flood forecasts and adjudicate on operational decisions. In addition to NFC, other sectors in MWRI such as NWS and HADA also make forecasts of inflows to Lake Nasser for short-term operational decisions using simple regression techniques. The lead time from the monitored river station at Eddeim on the Blue Nile is of the order of 17 days. Depending on the water level of Lake Nasser, and the expected flows, the committee may take measures to discharge water from the reservoir or open the Toshka spillway to accommodate high expected floods, or to cut some supplies if some drought is expected.

1.3 HISTORICAL INFORMATION ON DROUGHTS

Ethiopia faces a heightened vulnerability to extreme weather events such as droughts and floods. According to EM-DAT, the International Disasters Database, in the last 30 years there have been ten periods of drought (see Table 1-1) and 43 floods. One of the most serious drought events, which occurred in 2003, affected approximately 12.6 million people. In addition to the direct impact on human lives, natural disasters have been also detrimental to Ethiopia’s economy. Total economic damage costs due to the three major droughts since 1969 are estimated at US$ 92.6 million (EM-DAT, 2010).

In 2008, two successive seasons of minimal rain events left Ethiopia in drought, and millions of people across the country hungry as crops failed and food prices soared (NASA Earth Observatory, 2008). With close to half of Ethiopia's GDP attributable to the agricultural sector, managing food and economic security in the face of an uncertain climate continues to be an issue.

Table 1-1 List of the main droughts in the Blue Nile in Ethiopia and the total number of affected people

Disaster	Date	Total affected (Millions)
Drought	2003	12.6
Drought	May-83	7.8
Drought	Jun-87	7.0
Drought	Oct-89	6.5
Drought	May-08	6.4
Drought	Sep-99	4.9
Drought	Dec-73	3.0
Drought	Nov-05	2.6
Drought	Sep-69	1.7
Drought	Jul-65	1.5

[Source: Africa Water Atlas]

During the last 100 years, the Sahel Zone (extending into Sudan) had witnessed drought and famine years of crisis which claimed millions of animal and human lives. British records refer to several periods of serious drought (Table 1-2).

Table 1-2 List of the main droughts in Blue Nile in Sudan

Disaster	Date	Comment
Drought	1888-89	no rain for a year
Drought	1904	
Drought	1910-1911	
Drought	1925-1927	
Drought	1941-1942	

Drought	1948-1949	
Drought	1955- 1958	
Drought	1984	no rain
Drought	1990	no rain

[Source: http://adroub.net/default.aspx?page=Climate.%20Drought%20A]

1.4 STUDY OBJECTIVES

In the study area, there are models which could be useful in studying the droughts from the meteorological and hydrological perspectives. On the other hand, there is no model available to assess he impacts of droughts on agriculture. It will be useful if such a model is developed and tested within this study. This case study aims to test the available tools and provide improved tools for forecasting droughts and hence water availability in the region. The study will focus on the Blue Nile and Atbara River basins, and will pay particular attention to the expected effects of climate change on drought hazard. The case study is led by the Nile Forecast Center (NFC) in collaboration with other partners already active in the region. The following sections will shed more light on the sub-basins under study, the current drought monitoring and management practices within the region, and the approach used to assess current and future drought risk in the region in order to achieve the objectives of the study.

Drought indices are typically single numbers that are calculated including observed and proxy data related to rainfall, soil moisture, or water supply and provide a comprehensible synthesis of a situation for the decision maker that may be more useful than raw data. The use of a particular index to characterize drought depends on the objectives of the analysis, the study region, and the availability of data. Most water supply planners find it useful to consult one or more indices before making a decision.

For assessing meteorological drought, in section 3, the approach is to apply the Standardized Precipitation Index (SPI) to different rainfall datasets to assess its applicability in the study area. In addition, it will be applied to several climate change scenarios to evaluate the possible future change in drought risk.

In terms of hydrological drought, a set of indices are to be applied to observed as well as simulated and forecasted flows. This will assess the applicability of these indices and allows the evaluation of the current hydrological forecasting tool (the NFS) available at NFC in predicting drought.

In sections 4 and 5, the river flow, and rainfall observations were analyzed, and the impact of El Niño on the drought and flood in the upper catchment of the Blue Nile was evaluated. The suitable seasonal SST conditions were identified over the Pacific Ocean to be recommended as input to seasonal forecasting by water resources managers in the region. A simulation of an ensemble of 9 members describing the regional climate to study the impact of Niño on the drought and flood in the upper catchment of the Blue Nile was made.

Furthermore, in section 6, three runoff forecasting schemes were tested with different models for the Blue Nile station in Khartoum. Hence, the first forecasting scheme was established for June to August at a one month lead time. The second scheme was forecasting the flow of September to November at a one month lead time. The last forecasting scheme forecasted the runoff of the whole rainy season at a three month lead time.

2. METEOROLOGICAL DROUGHT ASSESSMENT

2.1 INTRODUCTION

Meteorological droughts are periods of less than normal rainfall over a specified region. Several indices have been developed to quantify the severity of meteorological droughts. One of the most commonly used of these is the Standardized Precipitation Index (SPI). This chapter presents the application of the SPI to assess droughts in the Eastern Nile sub-catchments of Atbara and Blue Nile under current and projected future climates. The methodology, including a description of the SPI and used models, is presented in the coming section (2.2) followed by the results of applying SPI to the selected basins in Section 2.3 and finally these results are discussed in Section **Error! Reference source not found.**.

2.2 METHODOLOGY

Historical and future meteorological drought occurrence over the Eastern Nile sub-catchments is assessed through calculating the Standardized Precipitation Index – SPI using the catchment rainfall from several sources. For historical rainfall, three datasets are used and results are compared in terms of drought frequency for a period starting in 1961 and ending in 1990 or beyond (except for the NFS dataset which starts in 1992). Future rainfall is taken from an ensemble of 6 RCM simulations for the period 2021-2050. The baseline rainfall series from the ensemble members (1961-1990) are first compared to observed rainfall and SPI before the impact of climate change on the frequency of drought is assessed. The following sections give more details about the different models and datasets used in the analysis.

2.2.1 The Standardized Precipitation Index

The Standardized Precipitation Index (SPI, McKee et al. 1993; 1995) assigns a single numeric value to the precipitation which can be compared across regions with markedly different climates. The SPI is the number of standard deviations by which an observed value deviates from the long-term mean, for a normally distributed random variable. Since precipitation is not normally distributed, a transformation is first applied so that the transformed precipitation values follow a normal distribution. SPI can be applied to monitor both droughts and floods.

The SPI is designed to be a relatively simple index, based on precipitation alone. Its fundamental strength is that it can be calculated all year round for a variety of time scales, either locally at a given point, or for precipitation averages over larger areas. This versatility allows the use of the SPI to monitor short-term water supplies, such as soil moisture, which is important for agricultural production, and longer-term water resources such as ground water supplies, stream flow, and lake and reservoir levels. The ability to examine different time scales also allows droughts to be readily identified and monitored for the duration of the drought. According to McKee et al. (1993), a drought event occurs any time the SPI is continuously negative and reaches an intensity of -1.0 or less. The event ends when the SPI becomes positive. Each drought event, therefore, has a duration defined by its beginning and end, and intensity for each month that the event continues. The positive sum of the SPI for all the months within a drought event can be termed the drought's "magnitude".

The SPI can be used as the basis for the analysis of the climatic input. Although the requirement for a transformation to a normal distribution could be a challenge in certain areas with highly skewed precipitation distributions, it offers the advantage of homogeneity across different areas covered by the DEWFORA consortium and can be used as the basis to generate global or continental maps of drought occurrence. The SPI can be very difficult to calculate in arid climates since the marginal distribution of precipitation is really non-symmetrical. In some regions the number of rainy days with very low precipitation is very high and the number of rainy days with very high precipitation is very low. In order to calculate the SPI it is necessary to find a previous transformation that gives rise to a marginal distribution. In many cases this can be difficult to implement and it could be an argument to adopt the percentile index. The SPI is normalised, since if transforms the precipitation to a normal distribution, and therefore permits comparison among drought values in different locations.

The program to calculate SPI was obtained from:
http://www.drought.unl.edu/monitor/spi/program/spi_program.htm
The method of calculation includes the following steps:

- Data preparation. Generation of a time series of the precipitation value of interest is generated. At least 30 years of data are needed.
- Determination of a probability frequency distribution that statistically fits the time series of precipitation data.
- Calculation of the cumulative probability distribution from the fitted frequency distribution.
- Transformation of the frequency distribution to the normal or Gaussian frequency distribution with a mean of zero and standard deviation of one so that values of the SPI are expressed as standard deviations.

Table 2-1 SPI Values and Corresponding Drought Intensity - McKee et al. (1993)

SPI Value	Drought Intensity
2.0 or more	Extremely wet

1.5 to 1.99	Very wet
1.0 to 1.49	Moderately wet
-.99 to .99	Near normal
-1.0 to -1.49	Moderately dry
-1.5 to -1.99	Severely dry
-2 and less	Extremely dry

Because SPI values are normally distributed, the frequencies of extreme and severe drought classifications for any location and any time scale are consistent. An extreme drought according to this scale (SPI = -2.0) occurs approximately 2-3 times in 100 years, an acceptable frequency for water planning. Fourth, because it is based only on precipitation and not on estimated soil moisture conditions as is the Palmer Drought Severity Index (PDSI), the SPI is just as effective during the winter months.

2.2.2 Observed Rainfall Datasets

The SPI has been calculated for catchment rainfall over the Blue Nile and Atbara sub-basins for the current climate from three different sources. These are the Climatic Research Unit (CRU) rainfall dataset, the ECMWF Rainfall Reanalysis dataset (ERA40), and the gauge-satellite merged rainfall dataset produced by the Nile Forecast System (will be referred to as the NFS dataset). The following sub-sections shed more light about each dataset. For the future climate, dynamically downscaled rainfall from an ensemble of 6 simulations is used. These were produced by the PRECIS regional climate model described in Section 2.2.3.

CRU Dataset

The Climatic Research Unit (CRU) of the University of East Anglia has been producing this dataset since the 1990s (New et al. 1999, 2000). This dataset has a global coverage at 0.5° spatial resolution. It has a monthly time step and comprises a set of important climatic variables including precipitation, temperature, humidity, diurnal temperature range, cloud cover, and potential evapotraspiration making it one of the most comprehensive climate datasets available. The CRU dataset is based only on observations interpolated to a regular grid in a two-tier process; first a climatology is interpolated for the period 1961-1990; then anomalies are interpolated to the same grid for other years creating a time series covering the period 1901-2009 by the latest version of the CRU dataset (3.1). The dataset creation methodology has changed slightly since it was first produced as documented by the various responsible scientists at the CRU – see for example Mitchel and Jones (2005).

For this study, precipitation from the CRU dataset version 3.0 was used covering the period up 2006 to calculate the SPI over the Eastern Nile sub-catchments. The CRU Dataset is available for download from (http://badc.nerc.ac.uk/browse/badc/cru/data/cru_ts_3.00). At the time of download, the latest version was not yet available. The starting date was selected to be 1961 to coincide with the available baseline data from the RCM simulations as the observed datasets (CRU, ERA40, and NFS) to allow cross-comparisons.

ERA40 Dataset

ERA-40 is an ECMWF (Eurpoean Center for Medium-range Weather Forecasting) re-analysis of the global atmosphere and surface conditions for 45-years, over the period from September 1957 through August 2002 by ECMWF. Many sources of the meteorological observations were used to produce this dataset, including radiosondes, balloons, aircraft, buoyes, satellites, scatterometers. These different data were assimilated through the ECMWF medium-range forecast model at 125 km resolution (about 1.125°). The data is stored in GRIB/NetCDF format. The reanalysis was done in an effort to improve the accuracy of historical weather maps and aid in a more detailed analysis of various weather systems through a period that was severely lacking in computerized data. For more information about the dataset refer to Uppala et al. (2004). The ERA40 rainfall was analysed as one of the "observed" datasets. ERA40 boundary conditions were also used to run PRECIS (described below in Section 2.2.3) and the resulting rainfall series was compared to original dataset to assess the quality of RCM simulations and the impact of that on SPI calculations.

NFS Dataset

The NFS rainfall dataset has been obtained from the NFS database as gridded daily rainfall fields (at a resolution of 20x20 km^2) for the period 1992–2011 (in fact, it is available in real-time but the analysis was limited to end of 2011). Although this period does not overlap with the selected baseline period (1961-1990), it is the historical period available with near-observed daily data, especially satellite data. The effect of this difference on the SPI frequency is found to be small – see the results below.

These rainfall fields were created by merging satellite-based and gauge-based gridded fields using a spatially fixed set of monthly weights. These weights were obtained from rainfall analysis over the Blue Nile and thus give more weight to satellite estimates during the rainy season (May-Oct) over the Ethiopian Plateau. The satellite-based estimate is inferred from half hourly infrared images received from the METEOSAT satellite (and quarter hourly images since 2007). These give the cloud-top temperature which is used to delineate rainfall areas using a threshold temperature of −40°C. Assuming that very cold temperatures correspond to very high clouds, which in turn are associated with rainfall, the daily rainfall rate over a pixel is calculated as a linear function of the Cold Cloud Duration (CCD). That is the duration for which that pixel is covered with a cold cloud computed by accumulating all the half-hourly counts. Initially, existing satellite estimation methods at the time of NFS development (early 1990s) were investigated for use within the NFS including the GOES Precipitation Index (GPI) (Arkin, 1979), the READING technique (Milford and Dugdale, 1990), the PERMIT technique (Barrett et al., 1989), the Convective-Stratiform Technique (CST) (Adler and Negri, 1988), and the Progressive Refinement Technique (PRT) (Bellerby and Barrett, 1993). Currently satellite rainfall is estimated by the Nile Hybrid technique (Green-Newby, 1992, 1993) which merges strengths of the CST and PRT Techniques to form a strategy designed to combine short-term and long-term satellite rainfall estimates to produce a high resolution (20 km) daily rainfall estimate.

Gauge estimates are obtained using the Nile Inverse Distance (NID) interpolation (Cong and Schaake, 1995) technique based on WMO synoptic gauge data downloaded daily from the Florida State University website (http://www.met.fsu.edu/rawdata/syn/). The NID is a variant of the inverse distance method in which rainfall at an ungauged location is estimated as the weighted average of rainfall at surrounding gauges where weights are the inverse distance between the gauges and the ungauged location (which are selected here to fall on the same grid as the satellite estimate). The final gauge estimate is the weighted sum of the interpolated estimate and the long-term mean rainfall at the ungauged location. Those weights are calculated such that the influence of the long-term mean increases with the distance to the nearest gauge with recorded rainfall on the day. This is similar to the climatologically aided interpolation (CAI) technique of Willmott and Robeson (1995). This method overcomes the sparseness and discontinuity of the records because, on any particular day, usually data from about 40 stations are available. These are not necessarily the same ones received on another day. The observed daily database has 236 entries while only 142 of these lie within or close to the basin. In the early stages of NFS development, gauge-based fields were used to calibrate the satellite estimation equations but operationally, the two estimates are calculated separately and then a weighted average is computed as the final rainfall estimate. More details about the NFS rainfall estimation component can be found in the operations manual (Nile Forecast Center, 1999) and Elshamy (2006).

This satellite-gauge merged dataset has a daily time step and was therefore aggregated to produce a monthly time series and spatially averaged over each of the studied basins.

2.2.3 RCM Simulations

The PRECIS regional modelling system developed by the UK Met Office (UKMO) / Hadley Centre has been used in this study to project future climate. This application considers uncertainties in the regional climate response to global climate change through the construction of an ensemble of 6 RCM runs, but not those arising from different emissions scenarios nor those arising from different downscaling methods (e.g. different RCMs or statistical methods). Results from the GCM were all derived for one emission scenario (SRES A1B) as previous studies (e.g. Elshamy et al., 2009) indicated that the uncertainty across climate models is much larger than that across emission scenarios, at least till 2050. Baseline simulations (1961-1990) from the ensemble are compared to the observed datasets mentioned above.

The study followed the UK Met Office (UKMO) procedure to select a subset of 6 scenarios out of the 17 QUMP (Quantifying Uncertainty in Model Predictions) ensemble members (UKCP09 - Murphy et al., 2009) for which boundary date are available from the UKMO. The different members of the QUMP ensemble are obtained by running the same GCM by slightly altering some physical parameters in the climate model to sample the range of climate sensitivity and produce a range of uncertainty similar to using multiple GCMs. The following sections provide a brief description of the history and development of PRECIS and an introduction to the different components of the model.

RCM Description

A regional climate model (RCM) is a high resolution climate model that covers a limited area of the globe, typically 5,000 km x 5,000 km, with a typical horizontal resolution of 50 km. RCMs are based on physical laws represented by mathematical equations that are solved using a three-dimensional grid. Hence RCMs are comprehensive physical models, usually including the atmosphere and land surface components of the climate system, and containing representations of the important processes within the climate system (e.g., cloud, radiation, rainfall and soil hydrology). Many of these physical processes take place on much smaller spatial scales than the model grid and cannot be modelled and resolved explicitly. Their effects are taken into account using parameterisations, by which the process is represented by relationships between the area or time averaged effect of such sub-grid scale processes and the large scale flow.

Given that RCMs are limited area models they need to be driven at their boundaries by time-dependent large scale fields (e.g., wind, temperature, water vapour and surface pressure). These fields are provided either by analyses of observations or by GCM integrations in a buffer area that is not considered when analysing the results of the RCM (Jones et al., 1995).

The Hadley Centre’s current version of the RCM (HadRM3P) is based on HadAM3H, an improved version of the atmospheric component of the Hadley Centre coupled AOGCM, HadCM3 (Gordon et al., 2000). HadRM3P has been used with horizontal resolutions of 50 and 25 km with 19 levels in the atmosphere (from the surface to 30 km in the stratosphere) and four levels in the soil. The RCM uses the same formulation of the climate system as in the GCM which helps to ensure that the RCM provides high-resolution regional climate change projections generally consistent with the continental scale climate change projected by the GCM.

Dynamical flow, the atmospheric sulphur cycle, clouds and precipitation, radiative processes, the land surface and the deep soil are all described in PRECIS. Boundary conditions are required at the limits of the model's domain to provide the meteorological forcing for the RCM. Information about all the climate elements as they evolve through being modified by the processes represented in the model is produced.

PRECIS Development

Under Article 4.1 and 4.8 of the UN Framework Convention on Climate Change (UNFCCC), all Parties to the convention are required to assess their national vulnerability to climate change and to submit regular National Communications. To this effect, the National Communications Support Unit (NCSU) of UNDP is developing an integrated package of methods to assist developing countries to develop adaptation measures to climate change. Assessments of vulnerability are informed by estimates of the impacts of climate change, which in turn are often based on scenarios of future climate.

These scenarios are generally derived from projections of climate change undertaken by Global Climate Models (GCMs). These GCM projections may be adequate up to a few hundred kilometres or so, however they do not capture the local detail often needed for impact assessments at national and regional levels. One widely applicable method for adding this detail to global projections is to use a regional climate model (RCM). Other techniques include the use of higher resolution atmospheric GCMs and statistical techniques linking climate information at GCM resolution with that at higher resolution or at point locations.

The idea of constructing a flexible regional modelling system originated from the growing demand of many countries for regional-scale climate projections. Only a few modelling centres in the world have been developing RCMs and using them to generate projections over specific areas as this task required a considerable amount of effort from an experienced climate modeller and large computing power. Both these factors effectively excluded many developing countries from producing climate change projections and scenarios. The Hadley Centre has configured the third-generation Hadley Centre RCM so that it is easy to set up. This, along with software to allow display and processing of the data produced by the RCM, forms PRECIS. The provision of a flexible RCM is thus part of an integrated package of methods, which would also include a range of GCM projections for assisting countries to generate climate change scenarios and hence to inform adaptation decisions. It can be run over any area of the globe on a relatively inexpensive, fast PC.

PRECIS (Providing REgional Climates for Impacts Studies, pronounced pray-sea, i.e. as in French), has been developed at the Hadley Centre and is sponsored by the UK Department for Environment, Food and Rural Affairs (DEFRA), the UK Department for International Development (DFID) and the United Nations Development Programme (UNDP). PRECIS runs on a personal computer (PC) and comprises:

- An RCM that can be applied easily to any area of the globe to generate detailed climate change projections,
- A simple user interface to allow the user to set up and run the RCM, and
- A visualisation and data-processing package to allow display and manipulation of RCM output.

To conduct thorough assessments, impact researchers need regional details of how future climate might change, which in general should include information on changes in variability (e.g. Arnell et al., 2003) and extreme events. An RCM is a tool to add small-scale detailed information of future climate change to the large-scale projections of a GCM. RCMs are full climate models and as such are physically based and represent most or all of the processes, interactions and feedbacks between the climate system components that are represented in GCMs. They take coarse resolution information from a GCM and then develop temporally and spatially fine-scale information consistent with it using their higher resolution representation of the climate system. In general they do not model oceans, as this would substantially increase the computing cost yet, in many cases, would make little difference to the projections over land where most impact assessments are conducted.

2.3 RESULTS

As mentioned earlier, the SPI was calculated for 1, 3, 6, 9, and 12 months lead times for the three mentioned historical rainfall time series as well as rainfall time series from 6 PRECIS simulations over the baseline period (1961-1990) and the future period (2021-2050). All calculations are made at the catchment scale for the Atbara and the Blue Nile catchments. The following section (2.3.1) compares precipitation across the three “observed” datasets while Section 2.3.2 shows the impact of climate change on rainfall and SPI.

2.3.1 Observed Rainfall Comparisons

Figure 2-1 shows the annual total rainfall series from the three observational datasets: CRU, ERA40, and NFS for the Blue Nile and the Atbara while Figure 2-2 shows the mean monthly distributions for the catchments. CRU dataset is close to that of the NFS for both catchments except during the peak rainfall months (July and August). ERA40 overestimates rainfall up to 1988 for the Blue Nile and up to 1978 for the Atbara compared to CRU rainfall. This overestimation occurs mainly during the recession period of the rainy season (Figure 2-2). The ERA40 PRECIS results are further overestimated but this occurs all year round resulting in about 32% more annual rainfall for the Blue Nile and about 70% more rainfall for the Atbara on average compared to original ERA40 dataset (which is already overestimated). This casts doubts on the use of this dataset for drought detection.

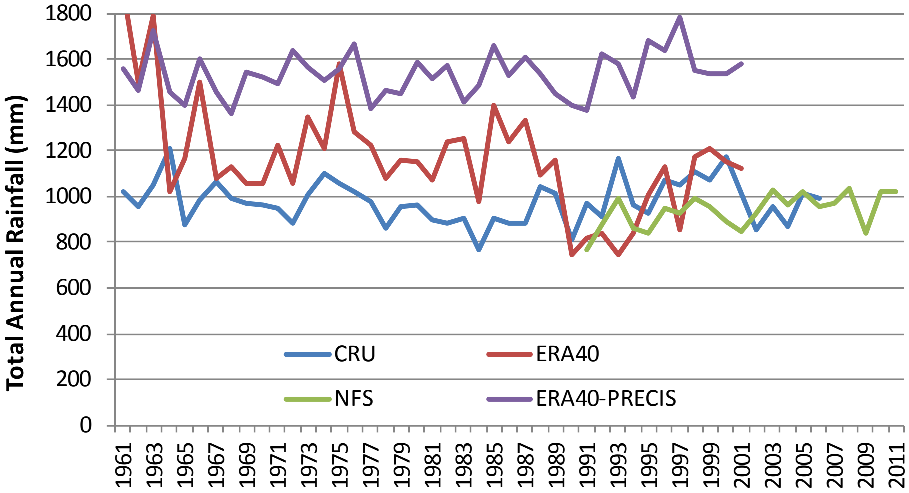

a) Blue Nile at Khartoum

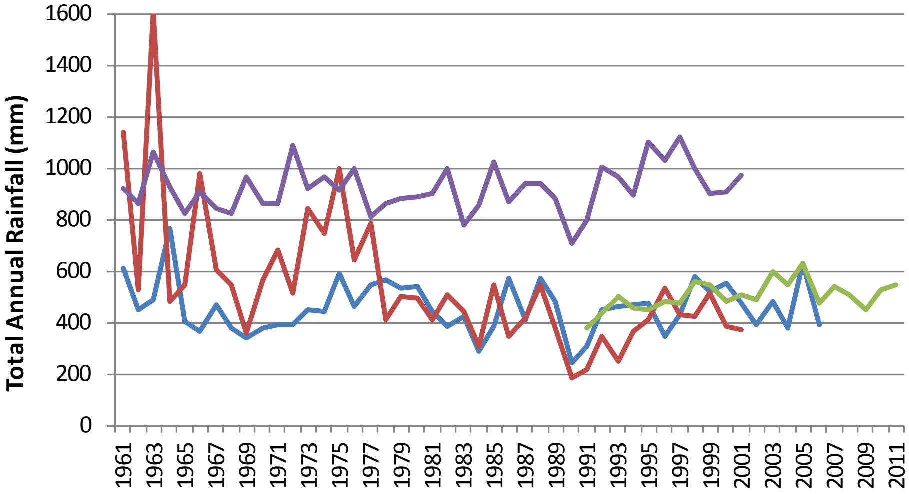

b) Atbara at Atbara Town

Figure 2-1 Annual “Observed” Rainfall Series for the Blue Nile and the Atbara

Figure 2-3 shows the calculated SPI time series for the hydrologic year (12-months SPI calculated at the end of July each year) for the ERA40 rainfall. The results clearly shows that PRECIS, having its climate evolving freely within its domain (which covers North Africa and Southern Europe) distorts the pattern in such a way that some dry years are predicted as wet and vice versa. This clearly shows the requirement for correcting the systematic overestimation bias that occurs for the seasonal distribution as shown in Figure 2-2. However, this was not done for this study.

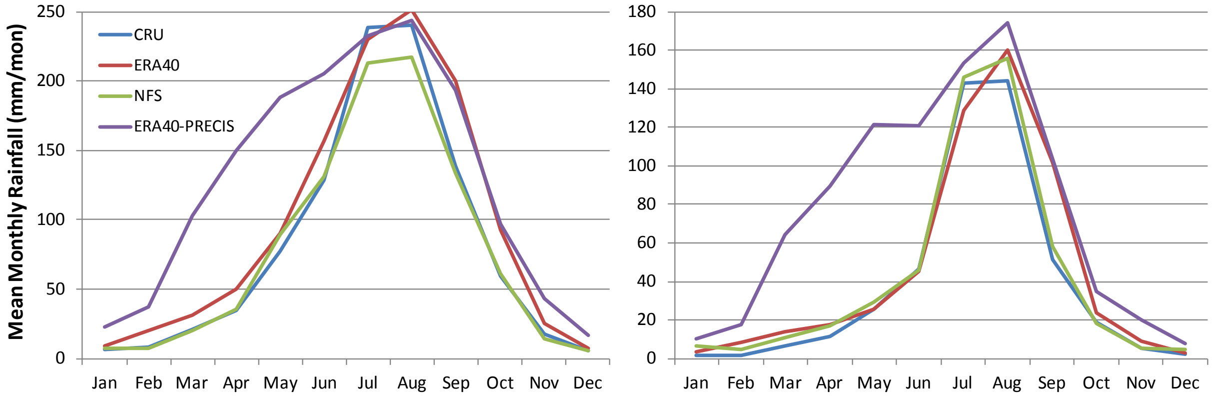

a) Blue Nile at Khartoum

b) Atbara at Atbara Town

Figure 2-2 Mean Monthly Distribution of "Observed" Rainfall Series for the Blue Nile and the Atbara

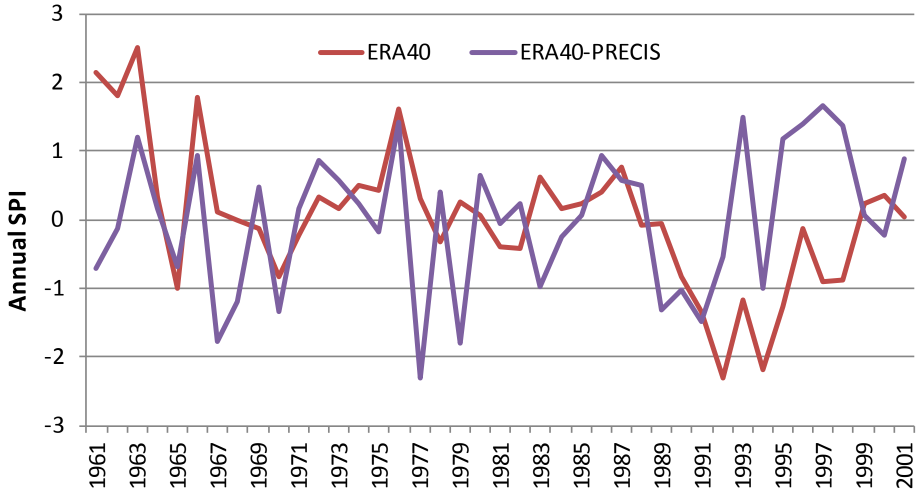

a) Blue Nile at Khartoum

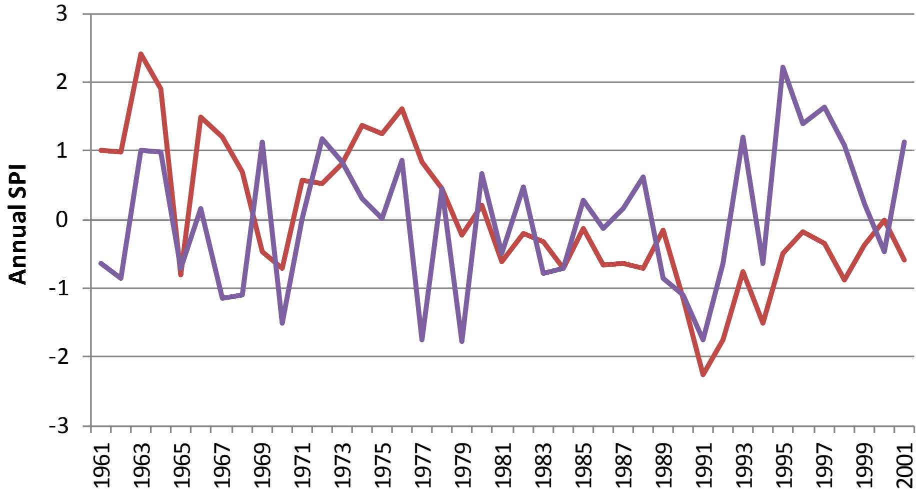

b) Atbara at Atbara Town

Figure 2-3 Hydrologic Year SPI for ERA40 Rainfall Series for the Blue Nile and the Atbara

2.3.2 Climate Change Impacts

Figure 2-4 shows the impact of climate change on the cumulative frequency distribution of the rainfall over the Blue Nile and Atbara sub-catchments. The distributions of the ERA40 are higher than those of both CRU and NFS datasets for both sub-catchments resulting from the overestimation shown above. The CRU deviates from the NFS for high rainfall (at 20% probability of exceedance) but the distributions are very close elsewhere indicating similar probabilities for droughts. The distributions of the PRECIS rainfall (shown as a range from the 6 simulations) take the shape of the ERA40-PRECIS with slight increase in the future for both basins (about 6% on average for both basins). This further indicates that the source of the bias is the RCM itself.

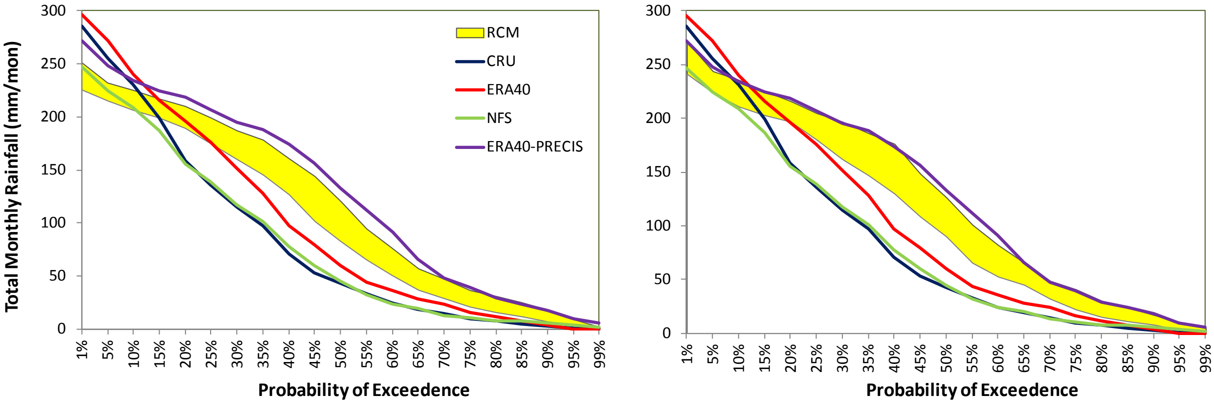

a) Blue Nile - Present (1961-1990)

b) Blue Nile - Future (2021-2050)

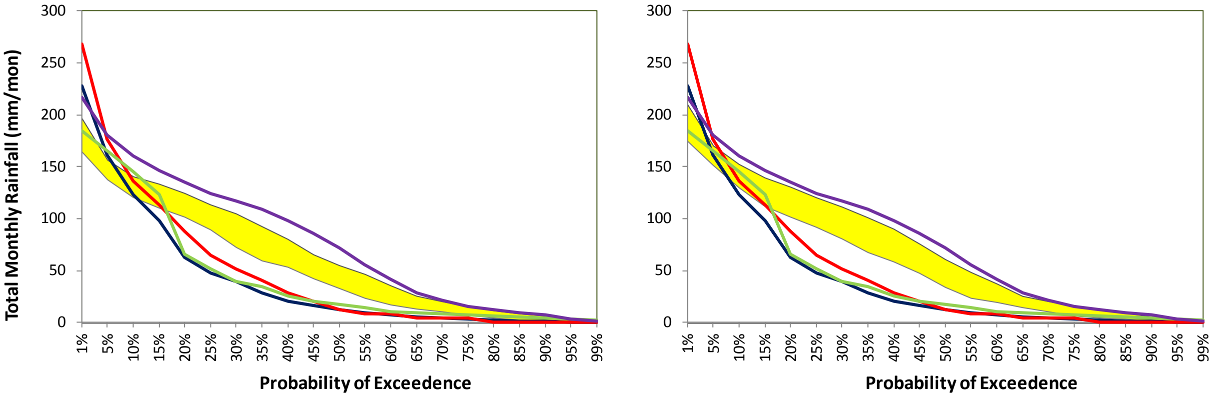

c) Atbara - Present (1961-1990)

d) Atbara - Future (2021-2050)

Figure 2-4 Impact of Climate Change from 6 RCM Simulations on Rainfall Frequency Distribution of the Blue Nile and Atbara. (The yellow band indicate the range across the 6 PRECIS simulations)

Because the SPI normalizes rainfall, SPI distributions of all three observed datasets (CRU, ERA40, and NFS) in addition to the ERA40 PRECIS simulation take similar shapes as shown in Figure 2-5 for annual SPI series calculated over the hydrologic year (August to July). Climate change as depicted by the 6 PRECIS simulations raises the whole distribution indicating more rainfall over all probabilities, especially for the Blue Nile. For the Atbara, though, the uncertainty (as indicated by the bandwidth) seem to increase at the low end of the distribution indicating that some scenarios still predict increases in drought despite the general increase in rainfall.

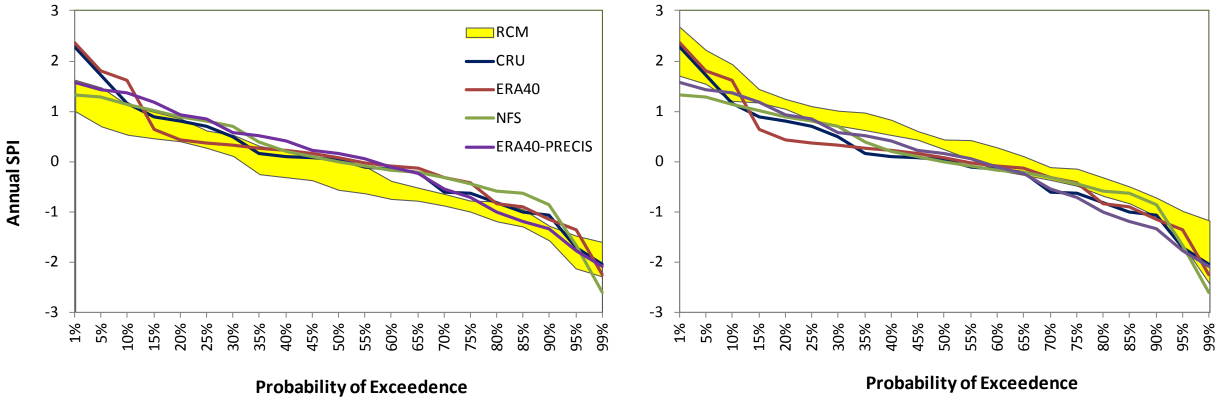

a) Blue Nile - Present (1961-1990)

b) Blue Nile - Future (2021-2050)

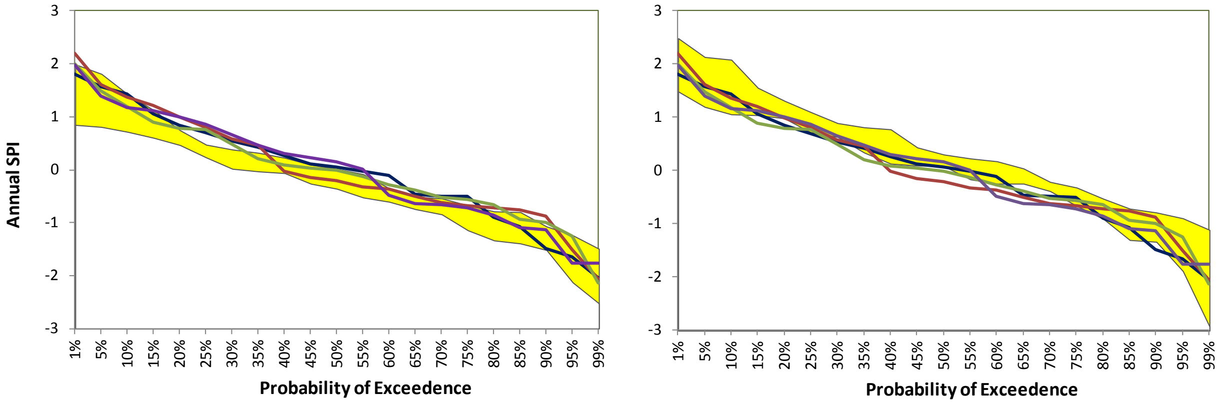

c) Atbara - Present (1961-1990)

d) Atbara - Future (2021-2050)

Figure 2-5 Impact of Climate Change from 6 RCM Simulations on Hydrologic Year SPI Frequency Distribution of the Blue Nile and Atbara

Figure 2-6 to 3-10 show similar results to what is seen for the annual series (Figure 2-5) above except that the bandwidth across PRECIS simulations is smaller because of the increased sample size – these are monthly time series. In fact the bandwidth increases with the lead time. The figures show the SPI distributions calculated for 1, 3, 6, 9, and 12 months in sequence. Probability distributions shift upwards in the future indicating more rainfall over the different probability bands, however, with some increases in both flood and drought probabilities at the edges of the distribution, i.e. increased probability of extremes. This is clear for droughts of the Blue Nile SPI at one month lead time (compare Figure 2-6 a and b), flood probability of the Blue Nile at 3 months lead time (compare Figure 2-7 a and b), and both drought and flood probabilities of the Atabara at 6 and 9 months lead times (compare Figure 2-8c vs. d and Figure 2-9c vs. d).

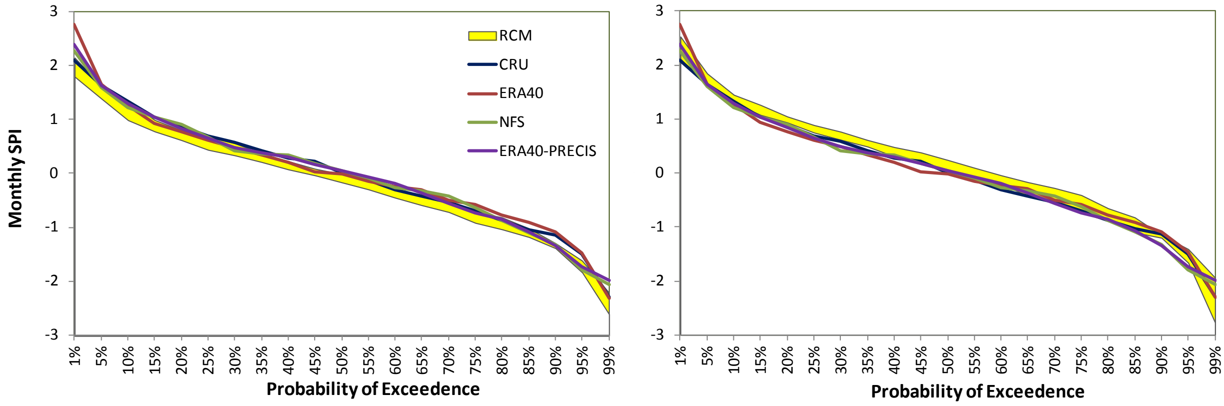

a) Blue Nile - Present (1961-1990)   b) Blue Nile - Future (2021-2050)

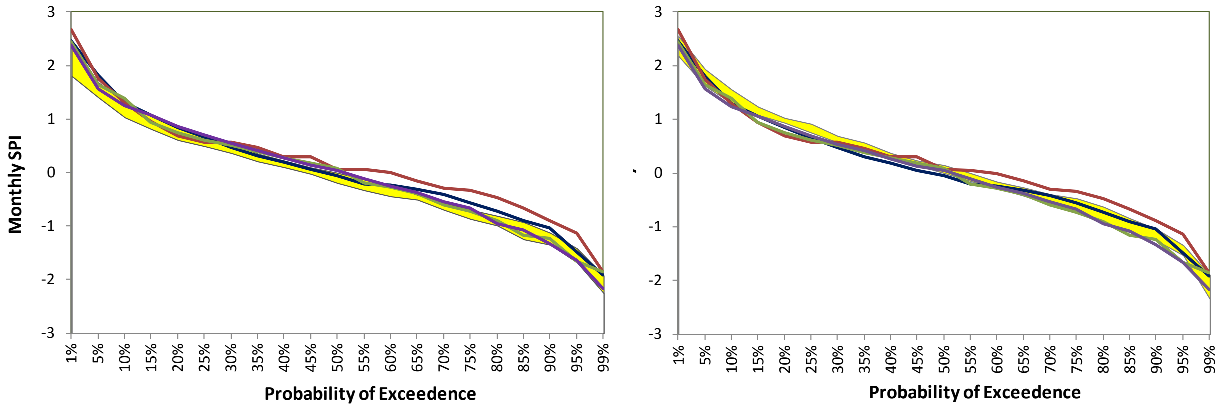

c) Atbara - Present (1961-1990)   d) Atbara - Future (2021-2050)

Figure 2-6 Impact of Climate Change from 6 RCM Simulations on Monthly SPI Frequency Distribution of the Blue Nile and Atbara

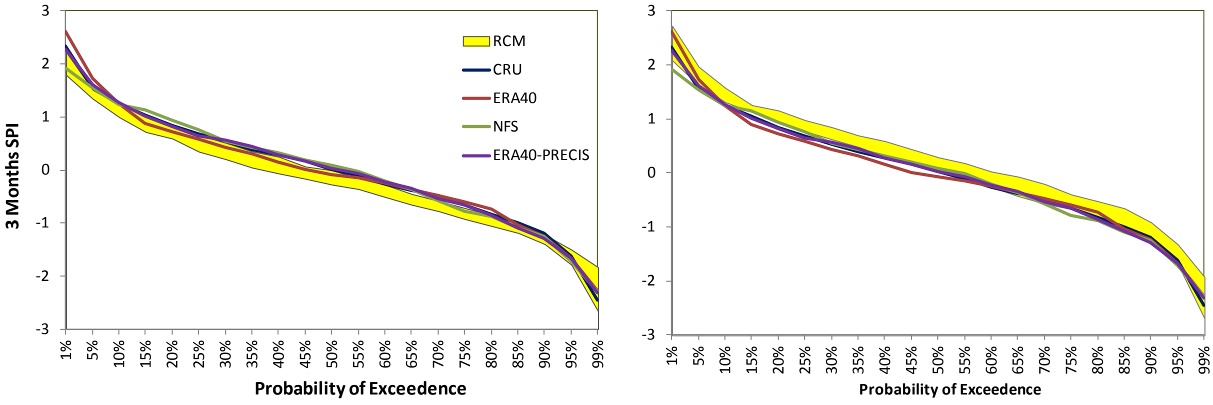

a) Blue Nile - Present (1961-1990)   b) Blue Nile - Future (2021-2050)

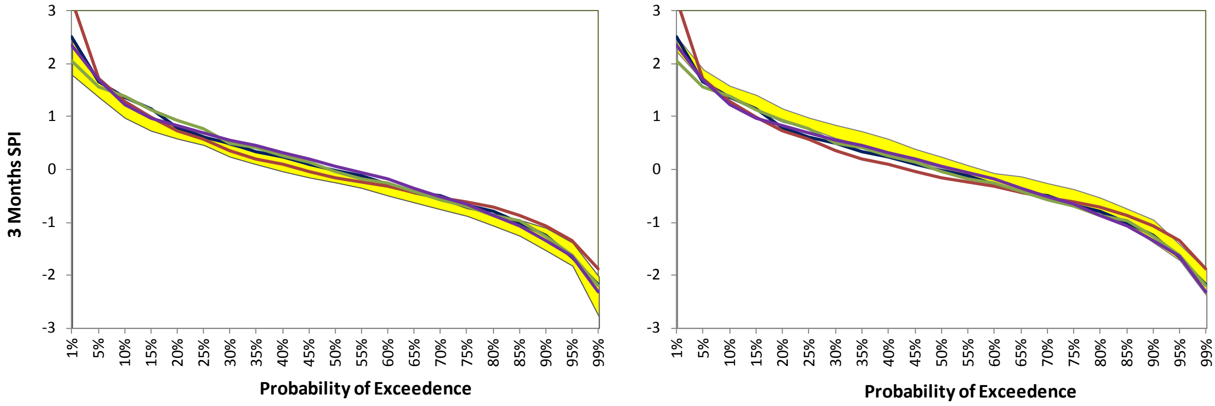

c) Atbara - Present (1961-1990) d) Atbara - Future (2021-2050)

Figure 2-7 Impact of Climate Change from 6 RCM Simulations on 3-Monthly SPI Frequency Distribution of the Blue Nile and Atbara

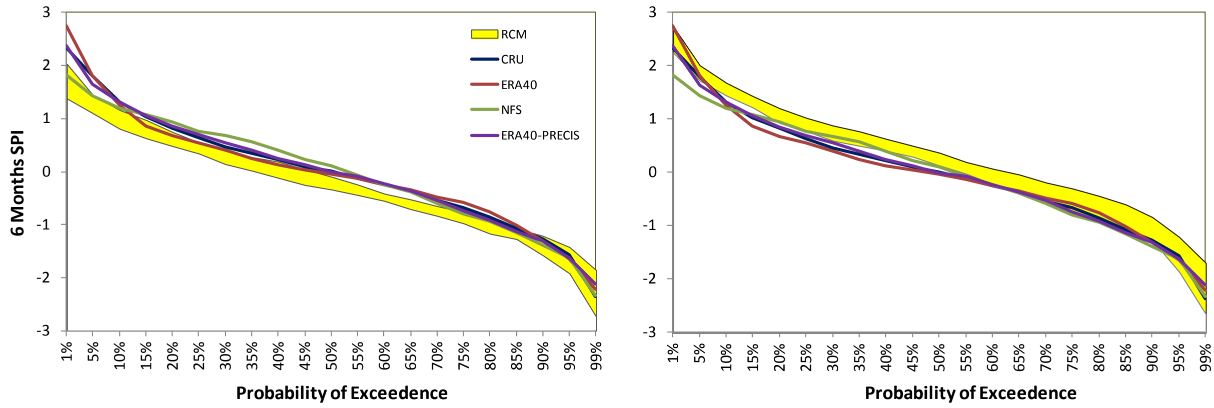

a) Blue Nile - Present (1961-1990) b) Blue Nile - Future (2021-2050)

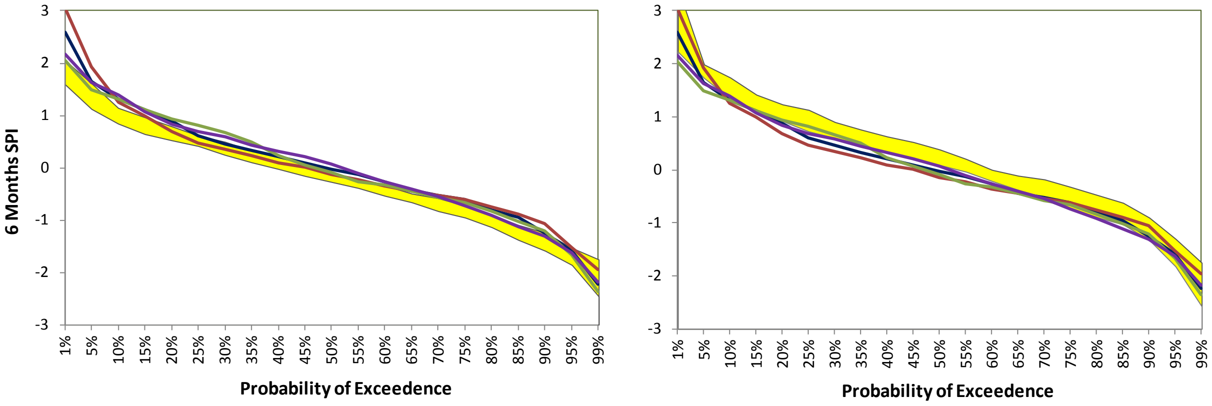

c) Atbara - Present (1961-1990) d) Atbara - Future (2021-2050)

Figure 2-8 Impact of Climate Change from 6 RCM Simulations on 6-Monthly SPI Frequency Distribution of the Blue Nile and Atbara

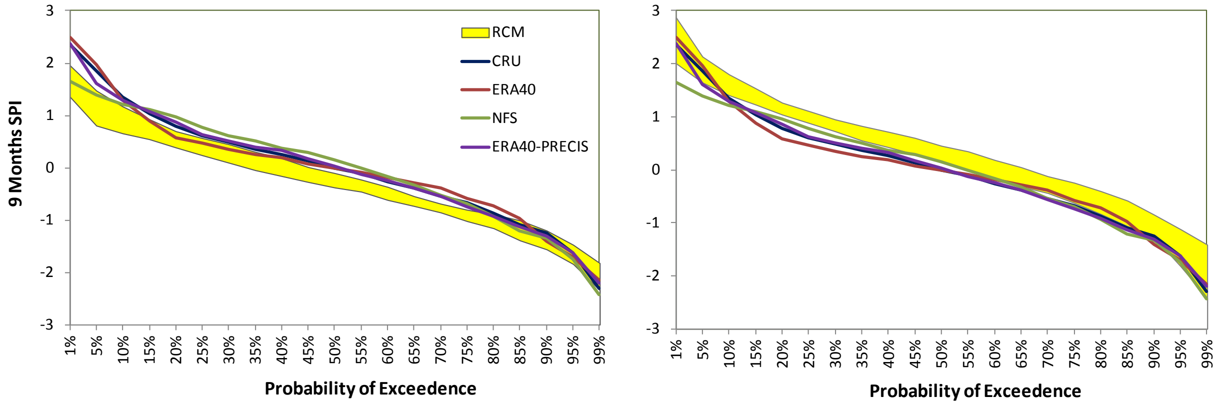

a) Blue Nile - Present (1961-1990) b) Blue Nile - Future (2021-2050)

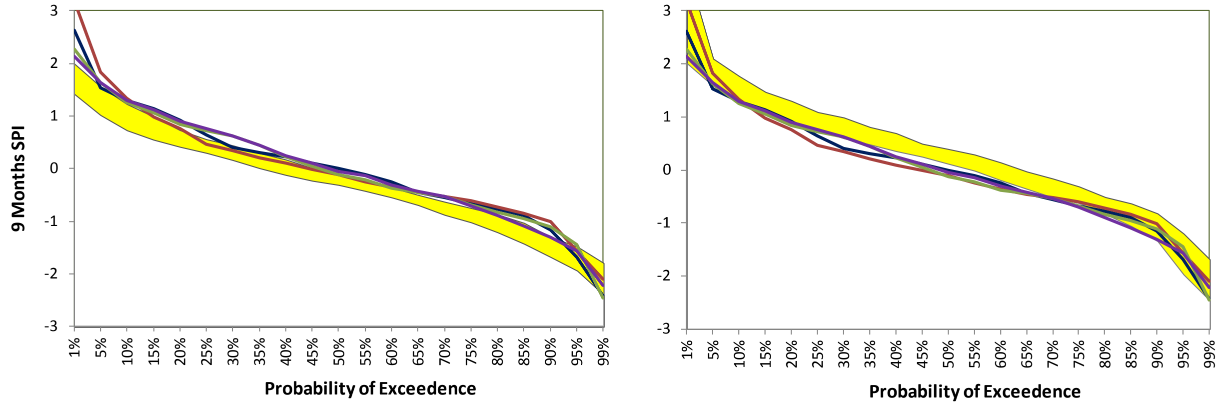

c) Atbara - Present (1961-1990) d) Atbara - Future (2021-2050)

Figure 2-9 Impact of Climate Change from 6 RCM Simulations on 9-Monthly SPI Frequency Distribution of the Blue Nile and Atbara

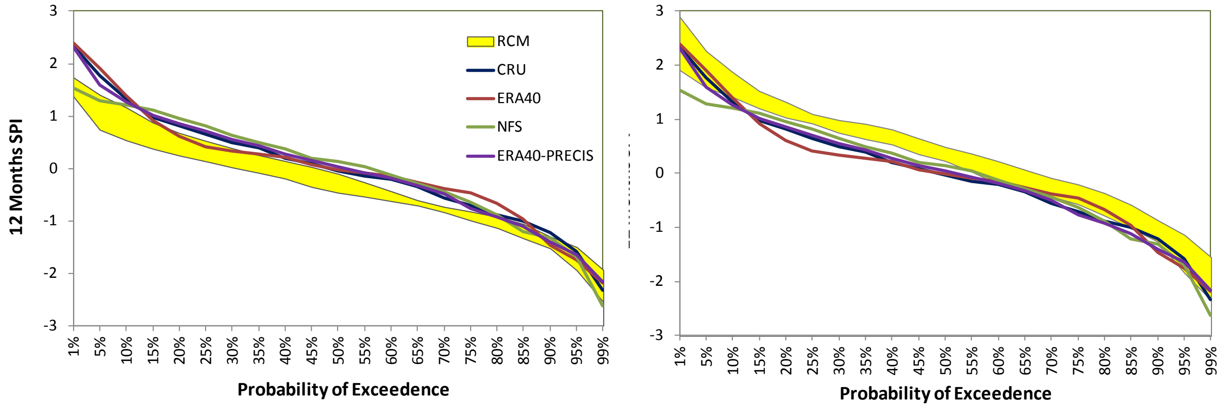

a) Blue Nile - Present (1961-1990) b) Blue Nile - Future (2021-2050)

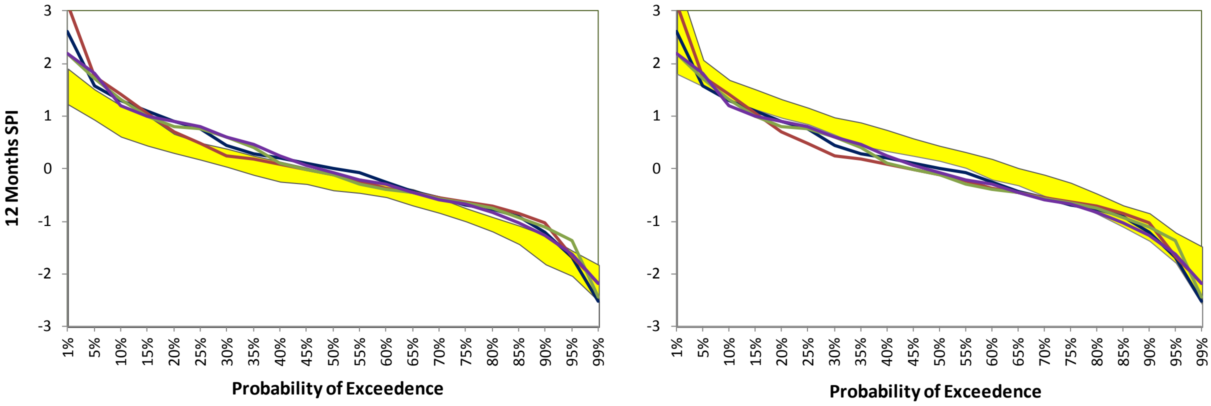

c) Atbara - Present (1961-1990)

d) Atbara - Future (2021-2050)

Figure 2-10 Impact of Climate Change from 6 RCM Simulations on 12-Monthly SPI Frequency Distribution of the Blue Nile and Atbara

2.4 CONCLUSION

The results show that ERA40 rainfall is overestimated for the Eastern Nile region compared to CRU and NFS rainfall datasets for early part of the record, distorting the rainfall distributions, and to a lesser extent the SPI distributions. CRU rainfall is higher than NFS for the region during the peak rainfall, and thus has higher flood probabilities but similar drought probabilities. When run using ERA40 boundary condition (which does not include precipitation), PRECIS overestimates rainfall over the whole year, resulting in different seasonal rainfall distributions compared to ERA40 rainfall. This has its effect on the SPI as some dry years may be seen as wet and vice versa. Such biases need to be corrected, but their effect is somewhat reduced in calculating SPI because it involves normalization of rainfall distributions.

The current set of climate simulations indicate a general increase in rainfall over the region but this does not exclude the increase of drought probability for some lead times especially longer ones and on the scale of the hydrologic year. The uncertainty bandwidth (defined by the range across the different simulations) increases near the ends of the SPI probability distributions but not for all lead times.

The SPI proved to be a useful way to characterize meteorological drought across different catchments and at different time scales. Because it normalizes the rainfall distribution, it is less sensitive to systematic biases in the data (i.e. systematic overestimation or underestimation – shifts in the mean).

3. HYDROLOGICAL DROUGHT ASSESSMENT

3.1 INTRODUCTION

Hydrological droughts occur when the deficit in precipitation extends to large periods and therefore there is a shortfall on surface or subsurface water supply. Therefore, hydrological droughts follow from meteorological droughts but they are affected by the catchment size and the existing management infrastructure. Meteorological drought indices respond to weather conditions that have been abnormally dry or abnormally wet. When conditions change from dry to normal or wet, for example, the drought measured by these indices ends without taking into account streamflow, lake and reservoir levels, and other longer-term hydrologic impacts. Meteorological drought indices do not take into account human impacts on the water balance, such as irrigation. These aspects are considered when computing hydrological drought indices.

Based on time series of hydrological drought characteristics, corresponding indices (single values) can be derived, for example the mean annual minimum flow or mean annual deficit duration. As droughts are regional in nature and critical drought conditions occur when there is an extreme shortage of water for long durations over a large area, a drought study often includes the spatial extent of the drought as a measure of the severity of the drought.

A common feature of all indices is that they are calculated over a particular period of time within the year (e.g., March to October). The period of time to be considered in the calculation depends on the characteristics of the systems to be analysed. For example, dryland agriculture is affected by the atmospheric behaviour of short periods of time (i.e., one or two months) while the rate at which shallow wells, small ponds, and smaller rivers become drier or wetter is affected by the atmospheric behaviour of longer periods (i.e., several months). Some processes have much longer time scales, such as the rate at which major reservoirs, or aquifers, or large natural bodies of water rise and fall, and the time scale of these variations is on the order of several years.

This chapter presents the application of three hydrological drought indices to assess droughts in the Eastern Nile sub-catchments of Atbara and Blue Nile under current and forecasted flow conditions. The methodology, including a description of the selected indices and used models, is presented in the coming section (4.2) followed by the results of applying the indices to the selected basins in Section 4.3 and finally these results are discussed in Section 4.4.

3.2 METHODOLOGY

Under work package 3, Deliverable D3.1, titled “White paper for definition of drought vulnerability across Africa”, gives short descriptions for the most common drought indices used. In this study, we test two of the common drought indices. The first is the *Surface Water Supply Index (SWSI)*, mentioned in D3.1, which is calculated using forecasted flow. The other, not mentioned under D3.1, is the streamflow Drought Index (SDI) which is commonly used in Asia (India, Iran, etc.). SWSI has been used to assess the drought frequency in streamflow forecasts while SDI has been applied to assess the drought frequencies for observed, simulated, and forecasted streamflows for the Eastern Nile sub-basins of Atbara and Blue Nile. Simulated and forecasted streamflows are calculated using the hydrological component of the Nile Forecast System (NFS). A third indicator developed by the Ministry of Water Resources and Irrigation of Egypt is adapted to assess droughts of the selected sub-basins based on the naturalized flows at the outlets of the sub-basins (based on observation).

3.2.1 NFS Hydrological Component and Forecasting

The NFS is a real-time distributed hydro-meteorological modelling system designed for forecasting Nile flows at designated key points within the Nile. Of major interest is the inflow of the Nile into the High Aswan Dam, Egypt. The system is hosted at the Nile Forecast Center (NFC) of the Ministry of Water Resources and Irrigation (MWRI), Giza, Egypt. NFS version 5.1 (Nile Forecast Centre, 2007) was used for this study. The current version of the NFS is 6.08, which is still under testing. Figure 3-1 shows a schematic of the NFS.

The core of the NFS is a conceptual distributed hydrological model of the whole Nile system including soil moisture accounting, hill slope and river routing, lakes, wetlands, and man-made reservoirs within the basin. The model accounts for irrigation abstractions in Sudan, but these are currently defined in a static way (i.e. inter-annual variability is not accounted for). The distributed hydrological model is defined on the quasi-rectangular grid of the METEOSAT satellite from which the system receives imagery to estimate rainfall. Each grid cell (pixel) imitates a small basin with generalized hillslopes and stream channels. Inputs to each grid cell are precipitation and potential evapotranspiration. This input is applied to a two-layer soil moisture accounting (water balance) model of the pixel. The upper layer is thin to represent the short-term detention of storm water. This layer receives precipitation inputs and evapotranspiration occurs at the potential rate. All rainfall is assumed to infiltrate the upper layer. Excess rainfall percolates to the lower layer which has a larger moisture capacity. If the evaporative demand is not met from the upper layer, water is extracted from the lower layer at a rate which varies linearly with the current moisture capacity. Subsurface runoff is calculated as a non-linear function of the relative moisture content of the lower layer (a non-linear reservoir). Surface runoff is calculated as a fraction of the excess rainfall which depends on the amount of the lower layer deficit. Surface and subsurface runoffs are subsequently input to the pixel's hillslope routing model, simulating the transfer of water towards the main channel. Generated runoff is then routed through this channel to the downstream pixel according to a pre-defined connectivity sequence. The system relies on a GIS database to represent the connectivity of the different pixels as well the different streams, rivers, and sub-basins associated with the designated forecast points.

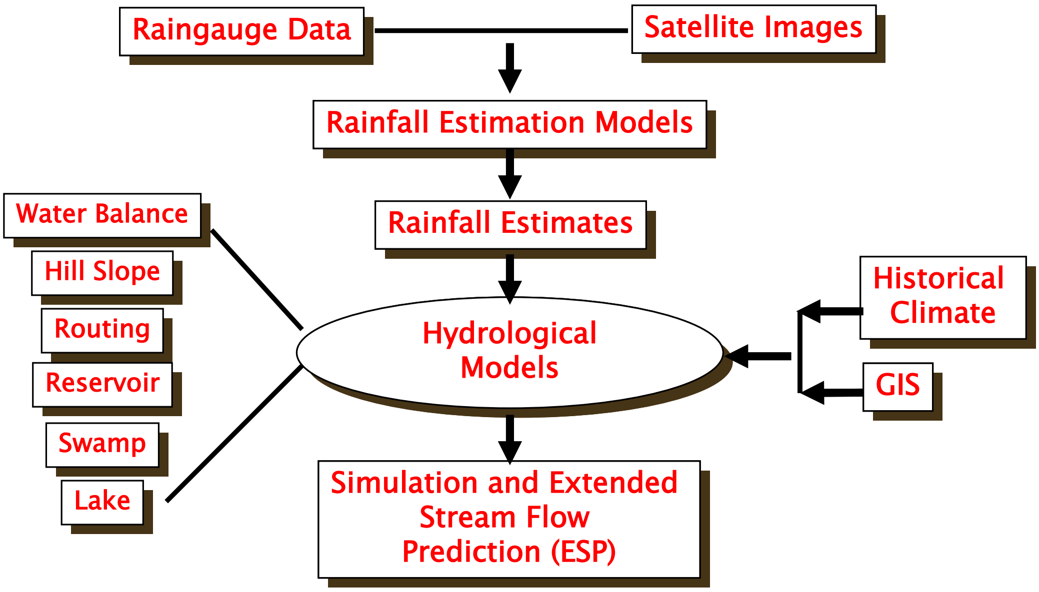

Figure 3-1 Schematic of the Nile Forecast System

Elshamy (2008) evaluated the long-term performance of the NFS at the monthly time scale and found that it is generally satisfactory for the Blue Nile and Atbara tributaries. For more details about the NFS refer to Nile Forecast Center (1999) and Elshamy (2006).

When used for forecasting as intended, a short NFS simulation (a few weeks) is performed using observed rainfall (merged satellite and gauge estimates as described in Section 0) to define the model status (soil moisture storage, reach storage) on the current date. Subsequently, an ensemble of historical rainfall (for as many years as available – currently 60 years are used) for the 3 months following the current date is applied to the model to simulate possible inflow series to Lake Nasser, called Extended (and more recently Ensemble) streamflow Predictions (ESP). The resulting flow traces are analysed statistically to provide forecast traces the 10% and 90% exceedance probability used as the bounds for the forecast and the 50% probability corresponding to the median forecast. These three values are generally the ones that get reported but values corresponding to other probabilities are also available from the analysis. Once a week observed flows at some key points (e.g. Diem at the Blue Nile near the Ethio-Sudanese border) are assimilated to update the model states. It implies that the rainfall estimates are adjusted for the last 4 weeks to minimise the difference between the simulated and the observed flows.

As mentioned above, the NFS requires rainfall and potential evapotranspiration data for the whole Nile basin as inputs. These are required as gridded rainfall and potential evapotranspiration data (i.e. maps) with a daily time step although monthly data can be also used as the system contains routines for disaggregating these to the daily time step. NFS also requires discharge data at key stations for assimilation, calibration, and performance evaluation. Discharge is usually obtained from stage measurements using rating curves that are updated annually based on concurrent stage and discharge measurements.

3.2.2 MWRI Drought Classification

In 2010, the Nile Yield Committee (see Section 0) commissioned a study to classify the Nile flood volume regarding floods and droughts. As Egypt is concerned with the total annual flow of the Nile over the hydrologic year (1st August – 31st July), the categories are based on the annual naturalized flow of the Nile at Aswan (Table 3-1). According to the 1959 Nile Water Treaty with Sudan, the average annual natural flow of the Nile is 84 BCM (1901-1950 average). Therefore, the categories are centred on this figure.

Table 3-1 MWRI Flow Classification According to Naturalized Flow (BCM) at Aswan

Category	Natural Flow at Aswan
Extremely dry	< 56
Very dry	56 - 70
Dry	70 - 77
Lightly dry	77 - 81
Near normal	81 - 87
Lightly wet	87 - 91
Wet	91 - 98
Very wet	98 – 112
Extremely Wet	> 112

For this study, flood/drought categories are needed at other important points along the Nile and were derived from the natural flow values at Aswan. For Dongola, the last river gauge above the inlet of Lake Nasser, the categories bounds are defined subtracting 14.5 BCM from the natural flows at Aswan. This figure is the average Sudan withdrawals over the study period.

For Khartoum, the categories bounds are calculated from those at Dongola based on the average percentage of the Blue Nile at Khartoum flows to the Main Nile flows at Dongola over the period 1992-2011. A similar procedure was done for Atbara and the Blue Nile at Diem (Table 3-2).

For this study, the ESP is run at decadal (10 days) time step over the period 1992-2011 and the flow forecasts for the locations (Dongala, Atbara, Khartoum, and Diem) are summed annually over the hydrological year. The median (50% probability) is used to characterize the flood and the time series of those flows are compared to the mentioned categories to determine the flood/drought condition. These are compared to observed records in Section 3.3.1.

Table 3-2 MWRI-Based Flow Classification and Corresponding Naturalized Flow Ranges (BCM) at Key Locations along the Main Nile, the Blue Nile, and the Atbara

Category	Dongola	Khartoum	Diem	Atbara
Extremely dry	< 41.5	< 24.5	< 27.5	< 6.5
Very dry	41.5 – 55.5	24.5 – 32.7	27.5 – 36.8	6.5 – 8.7
Dry	55.5 – 62.5	32.7 - 36.9	36.8 – 41.5	8.7 – 9.8
Lightly dry	62.5 – 66.5	36.9 – 39.2	41.5 – 44.1	9.8 – 10.4
Near normal	66.5 – 72.5	39.2 – 42.8	44.1 – 48.1	10.4 – 11.4
Lightly wet	72.5 – 76.5	42.8 – 45.1	48.1 – 50.7	11.4 – 12.0
Wet	76.5 – 83.5	45.1 – 49.3	50.7 – 55.4	12.0 -13.1
Very wet	83.5 – 97.5	49.3 – 57.5	55.4 – 64.7	13.1 -15.3
Extremely Wet	> 97.5	> 57.5	> 64.7	> 15.3

3.2.3 SWSI drought index

The Surface Water Supply Index (SWSI) combines hydrological and climatic features in a single index and allows for the consideration of reservoir storage. The SWSI is computed for a hydrographic basin or for a water resources system by obtaining the probability of non-exceedance for the values of precipitation, runoff, stored water, and snowpack in the basin (Garen, 1993, Shafer and Dezman, 1982). Each component is assigned a weight depending on local conditions. These weighted components are summed to determine the global SWSI value for the entire basin. The use of non-exceedance probabilities as a normalizing technique allows comparison of water supply availability among regions of differing variability.

The SWSI was first introduced in Colorado in the early 1980s (Shafer and Dezman 1982) to provide a more appropriate indicator of water availability in western United States than the widely used Palmer drought index (Palmer 1965). Subsequent developments of SWSI in Oregon and Montana have followed the same basic procedure as in Colorado, with minor differences in coefficient estimation and data usage. These indexes have been used by US state governments as a tool for monitoring drought and as a mechanism to trigger specific actions by state drought committees and other related groups.

The original SWSI was formulated as a rescaled weighted sum of non-exceedance probabilities of four hydrologic components: snowpack, precipitation, streamflow, and reservoir storage. The mathematical formulation of the SWSI is:

$$\boldsymbol{SWSI = \frac{aP_{snow} + bP_{prec} + cP_{strm} + dP_{resv} - 50}{12}}$$

where *a,b,c* and *d* are weights for each hydrological component*; a+b+c+d=1*; P_i is the probability of nonexceedance (in percent) for component i; and snow, prec, strm, and resv are the snowpack, precipitation, streamflow, and reservoir storage hydrological components respectively. By subtracting 50 the SWSI values are centred on zero, and dividing by 12 compresses the range of values between -4.17 and +4.17. This centering and compressing was done to make the values have similar magnitudes to the Palmer Index. Weights determined subjectively or from normalizing procedure but not optimized to predict a certain variable.

Although the SWSI is not the most widely used drought index, it was selected because of three main advantages. First, it can be computed with relatively few data, which are generally available in most water resources system (rainfall, streamflow, snowpack and reservoir storage). Second, it is computed for a water resources system, and can describe the global behaviour of the entire basin under analysis. Third, the weights assigned to the different components can be adapted to local requirements, depending on the specific structure of a given system (available resources, degree of development, demand type, relative role of regulation, snowpack or groundwater, etc.).

In 1993, Garen published a revised formulation for the SWSI based on streamflow volume forecasts:

$$\boldsymbol{SWSI = \frac{P_{fcst+resv} - 50}{12}}$$

The revised formula has a single probability of summed expected streamflow (over an appropriate time horizon) and current reservoir storage. The component weightings are done implicitly within the streamflow forecast. Streamflow forecast components vary throughout the year and switches to upcoming year at beginning of water year. This revision is sensible because rainfall and snowmelt both contribute to the streamflow and thus the original formulation was somewhat double-counting their effects. The SWSI values and categories are listed in Table 3-3.

Table 3-3 SWSI Drought Classification

Category	SWSI Range
Extremely dry	-4.2 to -3.0
Moderately dry	-2.9 to -2.0
Slightly Dry	-1.9 to -1.0
Near Average	-0.9 to 1.0
Slightly Wet	1.1 to 2.0
Moderately Wet	2.1 to 3.0
Extremely Wet	3.1 to 4.2

3.2.4 SDI Drought Index

As suggested by Mckee et al. (1993), the SPI procedure can also be applied to other water variables, such as soil moisture, snowpack, streamflow, reservoir and groundwater. The SDI developed by Nalbantis and Tsakiris (2009) and the Standardized Runoff Index (SRI) developed by Shukla and Wood (2008), have computation procedures very similar to that of SPI. The difference between SDI and SRI is that the SDI uses observed streamflow data, while the SRI uses simulated runoff data from hydrological models.

This index $SDI_{i,k}$ requires streamflow volume values $Q_{i,j}$ where i denotes the hydrological year and j denotes a month within the hydrological year. We can obtain $V_{i,k}$ cumulative streamflow volume for the i-th hydrological year and k-th reference period.

$$V_{i,k} = \sum_{j=1}^{ik} Q_{i,j} \qquad i= 1,2,3,\ldots, \; j= 1,2,\ldots 12, \qquad k= 1,2,3,4,\ldots$$

$$SDI_{i,k} = \frac{V_{i,k} - \bar{V}_k}{S_k}$$

Where V_k and S_k are respectively the mean and standard deviation of the cumulative streamflow volumes for the k-th reference period. The definition of states of drought with SDI are given in Table 3-4 below

Table 3-4 SDI Drought Classification

Category	SDI Range
Non drought	≥ 0.0
Mild drought	-1.0 to 0.0
Moderate drought	-1.5 to -1.0
Severe drought	-2.0 to -1.5
Extremely Dry	< -2.0

3.3 RESULTS

3.3.1 MWRI Drought Categories

As mentioned earlier, median ESP forecasts are compared to observations in terms of MWRI-based flood/drought categories at 4 main stations along the Main Nile, the Blue Nile, and the Atbara. For this analysis, total annual flows are calculated for hydrological years spanning the period August 1st to July 31st of the next year. Figure 3-2 shows the comparison at Dongola on the Main Nile. Forecasts seem to be close to observations especially for the first half of the record. For example, year 1998-1999 was a flood year, categorized as very wet for both observation and forecast. Similarly, 2010-2011 was a flood year categorized as very wet according to forecasts while the observed total lies in the wet category. The selected period has more flood years than drought years in general but most of the drought years (e.g. 2002-2003 and 2009-2010) are missed by the forecasts despite being very dry according to observations. In general the ESP seems to overestimate the flows resulting in wrong categorization of drought years.

Figure 3-3 and Figure 3-4 compare the observed and forecasted flow records for the Blue Nile at Khartoum and Diem respectively. Here the ESP seems to be less successful than at Dongola for flood years while it predicts drought years better. The ESP forecast volumes are generally underestimated especially in flood years (e.g. 1998-1999, 2006-2007 are observed to be very wet at Khartoum but only wet according to ESP forecast). The severity of the drought in 2002-2003 is underestimated by the forecast while the correct categories are picked for drought years 1997-1998, 2003-2004, and 2009-2010 at Khartoum. At Diem, the forecast line seems to be shifted down for the whole record. Therefore, flood categories are underestimated, while drought categories are overestimated by the forecasts.

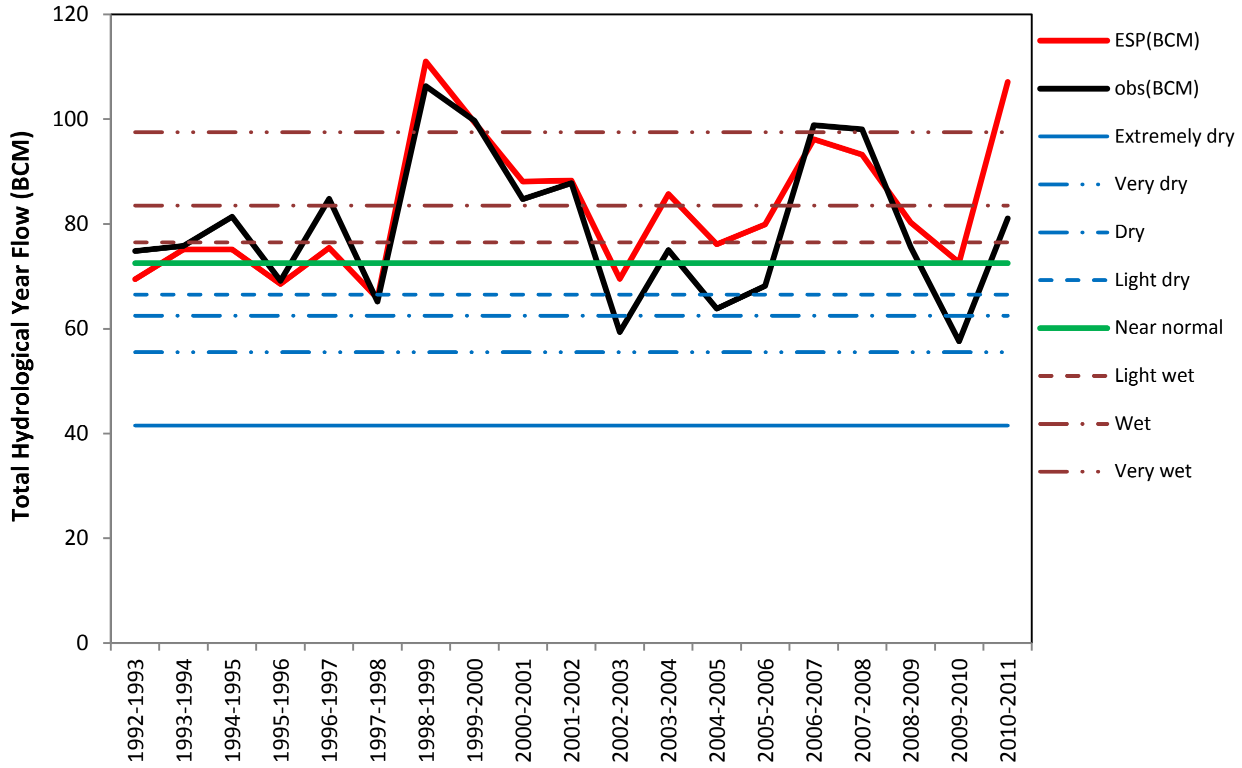

Figure 3-2 Categorized Observed and Forecasted Flows of the Main Nile at Dongola

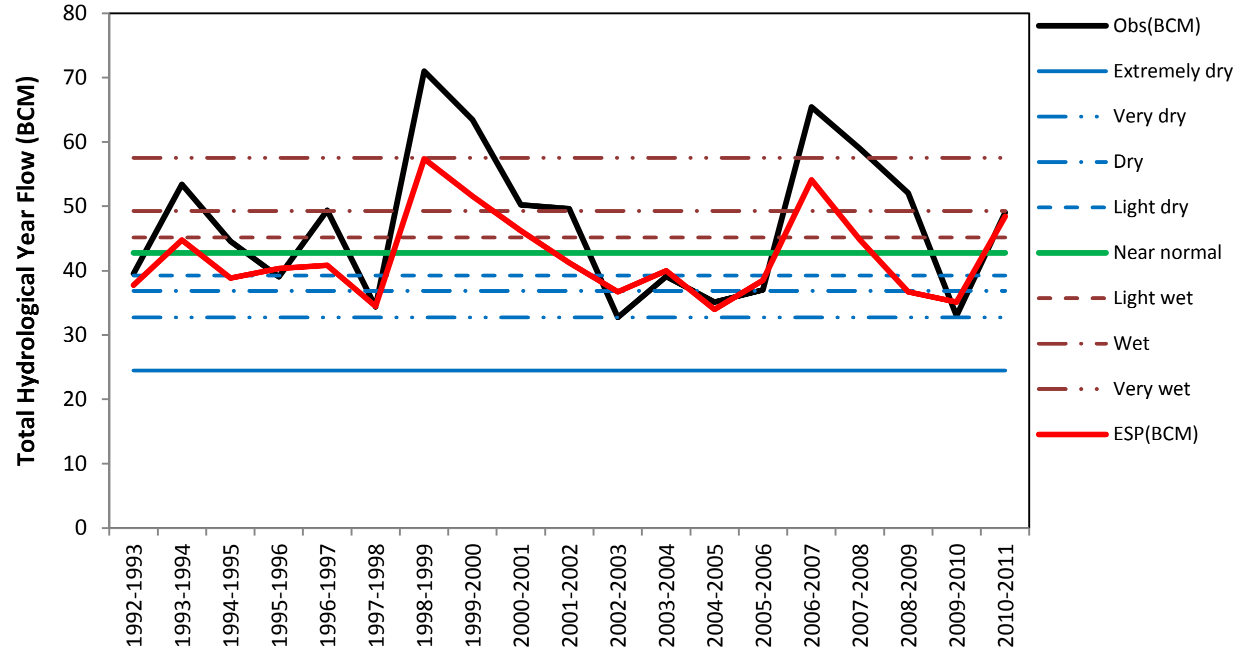

Figure 3-3 Categorized Observed and Forecasted Flows of the Blue Nile at Khartoum

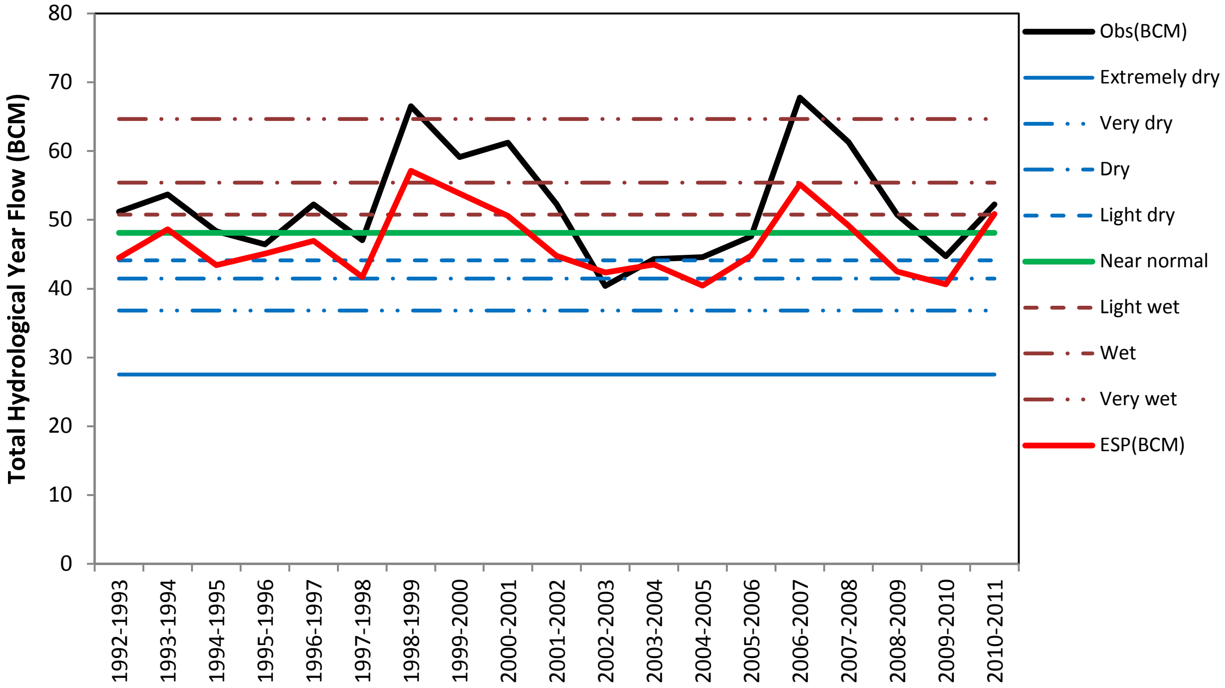

Figure 3-4 Categorized Observed and Forecasted Flows of the Blue Nile at Diem

Figure 3-5 shows the results for the Atbara where more discrepancies are observed. Categorizing a year as a drought year according to forecasts can turn out to be completely wrong, e.g. year 1994-1995 is an extremely wet year according to the derived categories for Atbara while it is forecasted as very dry. 2004-2005 was a dry year while the forecast shows it as a lightly wet year. The small range of the Atbara flows resulted in tight categories but the forecasts of the Atbara need to be revisited.

3.3.2 SWSI Drought Index

Streamflows were forecasted on a decadal (ten days) time step starting in May 1992 till October 2011 by using the median ESP forecast (probability of 50% exceedance). The forecasted flow was accumulated from the first of May till the end of October for each year (to get the flow forecast over the season). The period May-October denotes the rainy season for the Eastern Nile basins. This flow forecast is added to the actual storage in reservoirs at the end of April for both the Atbara and Blue Nile Basins.

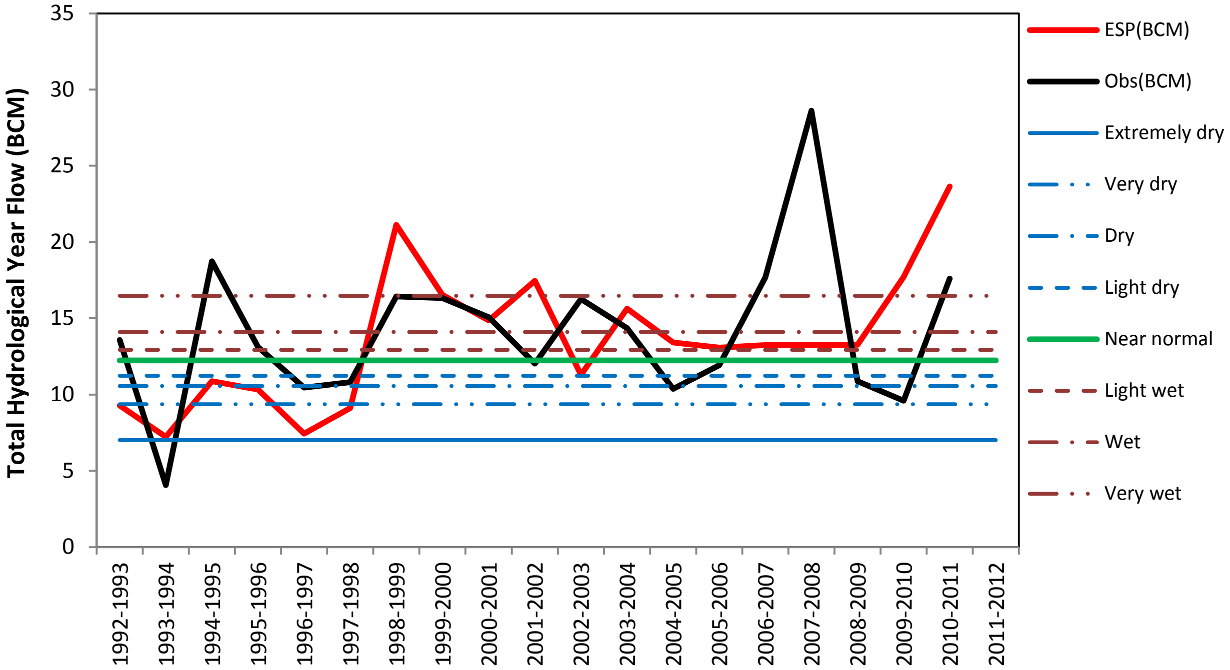

Figure 3-5 Categorized Observed and Forecasted Flows of the Atbara at Atbara Town

To calculate the SWSI, reservoirs need to have a historical record and have been managed consistently over time and data must be available in real time. On Atbara River, there is the Khashm El-Gerba (KEG) reservoir (1964) and the TK5 reservoir (2009), and on Blue Nile, two reservoirs exist, these are the Roseries (1966) and Sennar (1925). All reservoirs started operating (as in the brackets) prior to the start of the selected period except TK5. However, due to the short length of the record (only 20 years), years 2009-2011 were not omitted from the analysis.

The forecast points are selected at basin outlets; therefore, the Atbara town is selected as the outlet of the Atbara River, while Khartoum is the outlet of the Blue Nile. Then the forecasted streamflow for the season is added to the end April reservoir storage, prior to runoff. Finally, the results are sorted in descending order to calculate the non-exceedance probability using the empirical formula (1-(Rank/n+1)), where Rank represent the rank of the summed values in descending order, and n equals the total number of years analyzed. Fitting distributions was avoided because the record length is rather short and the fits are usually affected by the storage term. The previous steps allow the calculation of the SWSI values as explained in Section 3.3.2.

Table 3-5 SWSI values for the flood season during the period (1992-2011) for Atbara Basin

Rank	Year	ESP Flow	Observed	KEG Storage	ESP+Storage	Non-exceedence	SWSI
1	2010	21.15	17.91	1.23	22.38	0.95	3.77
2	1998	17.32	20.48	0.81	18.13	0.90	3.37
3	1999	15.23	13.23	1.01	16.24	0.86	2.98
4	2001	14.99	13.45	1.06	16.05	0.81	2.58
5	2011	14.88	10.25	1.10	15.98	0.76	2.18
6	2007	12.57	19.86	1.11	13.69	0.71	1.79
7	2005	12.63	13.56	1.01	13.64	0.67	1.39
8	2003	12.02	15.40	0.89	12.91	0.62	0.99
9	2000	11.18	13.92	1.12	12.30	0.57	0.60
10	2004	11.18	8.82	1.00	12.18	0.52	0.20
11	2008	10.18	22.66	0.88	11.06	0.48	-0.20
12	2009	9.91	8.37	0.84	10.74	0.43	-0.60
13	1994	8.82	13.11	0.83	9.65	0.38	-0.99
14	2006	8.19	16.08	1.02	9.21	0.33	-1.39
15	1995	7.59	15.42	0.96	8.55	0.29	-1.79
16	2002	6.93	15.01	1.05	7.98	0.24	-2.18
17	1992	6.78	8.13	0.69	7.47	0.19	-2.58
18	1993	6.18	7.70	1.14	7.32	0.14	-2.98
19	1996	6.00	10.30	0.97	6.97	0.10	-3.37
20	1997	5.38	10.23	0.98	6.35	0.05	-3.77

*All Flow Volumes and Storages are in BCM; Storage is taken as observed on 30th of April

Table 3-5 and Table 3-6 show the results of the SWSI values for Atbara and Blue Nile respectively. The results show some conflicts between Atbara Town, and Khartoum. For example, year 2001 is categorized as Moderately Wet for the Atbara River, while it is categorized as Near Average for the Blue Nile. However, this does not mean either is wrong. Despite the proximity of the basins, they need not be in the same flood/drought category each year as can be seen by comparing Figure 3-3 to Figure 3-5 (e.g. 1993-1994). The results do not reflect the actual situation of the flood season for the year 1997-1998 which is categorized as an extremely dry year for both rivers, while, in section 3.3.1 above, this year lies between mild drought and severe drought. The results for the Atbara are worse than those of the Blue Nile (Table 3-6) because of the reduced forecast quality for that basin compared to the Blue Nile. Flow forecast values need to be corrected to enhance the results of the SWSI values (compare the observed and ESP Flow columns).

The results also show that this method requires a large number of years (more than 40 years) to cover most hydrological phenomena. SWSI values are a function of the probability of non-exceedance which is obtained based on the rank of the year. In this study; the total number of the years is 20, and no extreme drought happened in the selected period, the values ranked at the bottom will always be Extremely Dry, even if that year is not really dry. It is the driest only on the used record.

Table 3-6 The SWSI values for the flood season during the period (1992-2011) for Khartoum Basin

Rank	Year	ESP Flow	Observed	Roseires	Sennar	ESP+Storage	Non-Exceedance	SWSI
1	1998	42.51	53.84	1.01	0.52	44.04	0.95	3.77
2	2007	39.83	61.37	1.97	0.51	42.31	0.90	3.37
3	2010	39.46	48.02	0.65	0.32	40.43	0.86	2.98
4	1999	37.68	49.62	1.52	0.53	39.73	0.81	2.58
5	2011	37.72	36.68	0.79	0.40	38.91	0.76	2.18
6	1993	35.37	42.89	1.33	0.49	37.19	0.71	1.79
7	2006	34.58	49.62	1.53	0.48	36.59	0.67	1.39
8	1996	33.86	43.97	0.93	0.49	35.28	0.62	0.99
9	2000	32.90	37.27	1.36	0.52	34.78	0.57	0.60
10	2003	31.71	36.02	0.98	0.49	33.18	0.52	0.20
11	2001	31.21	42.36	1.43	0.50	33.15	0.48	-0.20
12	1994	30.60	42.67	0.85	0.44	31.89	0.43	-0.60
13	2005	29.30	34.97	1.46	0.56	31.32	0.38	-0.99
14	2008	27.13	52.05	1.76	0.40	29.29	0.33	-1.39
15	2002	25.55	23.67	1.29	0.48	27.33	0.29	-1.79
16	1995	25.76	25.10	0.32	0.69	26.77	0.24	-2.18
17	2004	22.63	27.93	1.50	0.47	24.60	0.19	-2.58
18	1992	22.80	29.40	0.50	0.42	23.72	0.14	-2.98
19	2009	21.42	27.37	1.30	0.40	23.11	0.10	-3.37
20	1997	21.35	27.83	1.21	0.51	23.08	0.05	-3.77

All Flow Volumes and Storages are in BCM; Storage is taken as observed on 30th of April

3.3.3 SDI Drought Index

In this section, the Standardized Discharge Index (SDI) is calculated using the observed discharge time series, NFS simulated flow, and the median of ESP forecasted flow generated as explained above. Figure 3-6, Figure 3-7 and Figure 3-8 compare the SDI across the observed, simulated, and forecast for Atbara, Diem, and Khartoum respectively. The simulated and forecasted SDI at Atbara in many years did not have the same direction of the observed SDI, this is clear in years 1994, 1995, 2001, 2002, 2004, 2006, 2008, and 2011. These results indicate that the hydrological model of Atbara should be calibrated and it is clear that the bad simulation of Atbara could be the reason for the poor results of the ESP used to calculate SWSI above.

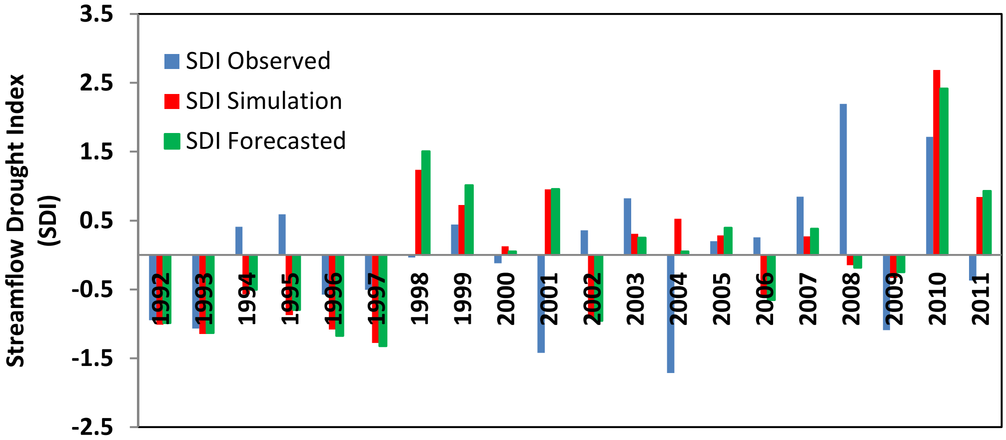

Figure 3-6 Seasonal values of SDI over the Atbara river during the period (1992-2011)

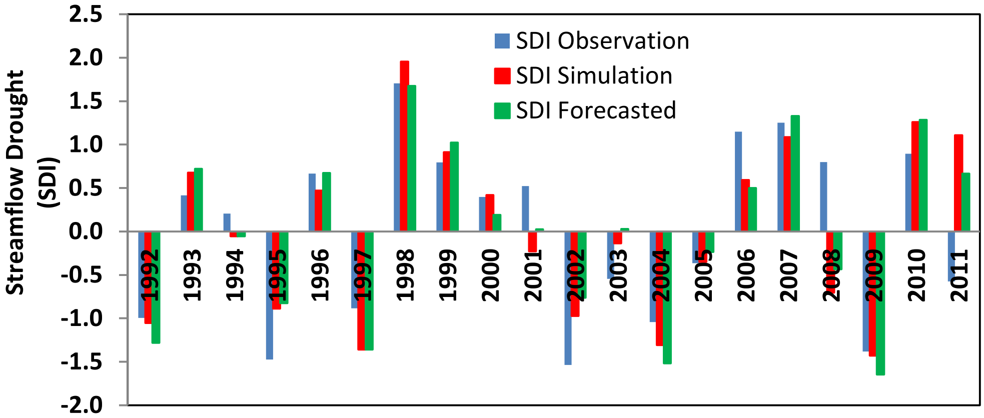

Figure 3-7 Seasonal values of SDI over the Upper Blue Nile at Diem during the period (1992-2011)

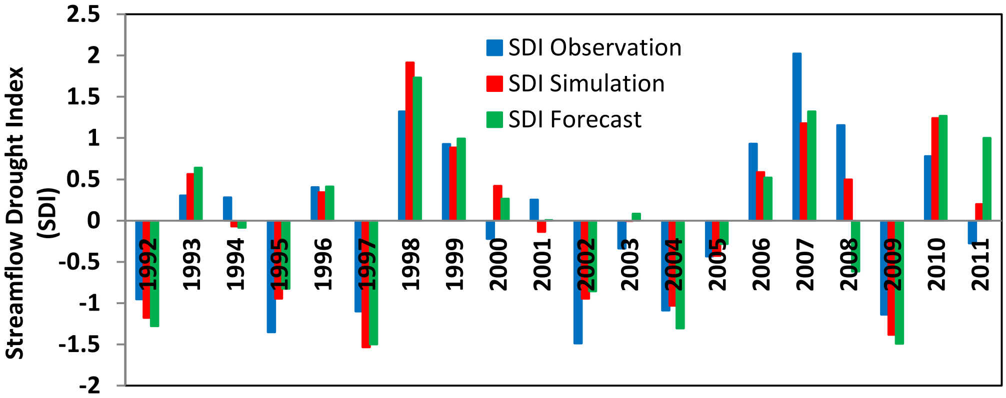

Figure 3-8 Seasonal values of SDI over the Blue Nile at Khartoum during the period (1992-2011)

The results of the Blue Nile at Diem and Khartoum show that the observed SDI, Simulated and forecasted SDI have the same sign for most years. During the whole period (1992-

2011), not a single year recorded DSI close to -2.0, which means that no extremely dry years occurred during the study period. Most years were near average or not dry, and in all drought years the SDI was > -1.5, i.e. drought years were only in the moderate drought range.

3.4 CONCLUSION

From the above results we can summarize the conclusion in these points:

- The MWRI classification method has been successfully adjusted for the application to the selected sub-basins. However, the small flow range of the Atbara results in small bounds for the categories which makes it difficult to get the right drought characterization.
- The hydrological model or forecasting parameters of the Atbara basin need to be revisited. A proper calibration is needed so as to study the drought situation for that basin.
- The quality of SWSI Results depends on the accuracy of the forecasted flow and the length of record.
- The SDI is an easy method to categorize the drought even for the observed or simulated stream flow time series.
- The selected drought indices seem to be useful and applicable but the data and modelling need to be improved to obtain the right information about any coming drought.
- Other drought indices need to be studied and compared before selecting the best index to characterize drought in the Eastern Nile region.

4. THE CONNECTIONS OF ENSO AND DROUGHT AND FLOOD OVER THE UPPER CATCHMENT OF THE BLUE NILE BY USING OBSERVATIONAL DATASET

4.1 INTRODUCTION

The Nile is the longest river in the world with a length of 6,650 km and it flows through ten countries Jury, (2004). The major two tributaries, the White Nile and Blue Nile form the main Nile in Khartoum, and the seasonal Atbara River joins the Nile approximately 500 km downstream. The Blue Nile originates from Lake Tana in Ethiopian Highland and contributes around 67% to the main Nile discharge. The Upper Blue Nile River Basin is 176 000 km^2 in area (Conway, 2000). The rainfall regime follows the seasonal solar heating of the air above the Ethiopian Plateau, and the rainy season extends approximately from June to September. The Blue Nile (known as Abay River in Ethiopia) and its tributaries originate from the Ethiopian plateau, at elevations of 2000-3000 m. The two main tributaries of the Blue Nile in Sudan are Rahad and Dinder. The rainy season in Ethiopia from June to September known locally as Kiremt, Seleshi and Zanke (2004), and rainfall is highly variable both temporally and spatially, Gissila et al., (2004).

The Blue Nile sustains the life of millions of people in Ethiopia, Sudan and Egypt. Rainfall has a great impact on the social and economic life in the region. Scarcity in rainfall leads to drought while excessive, intense rainfall may lead to floods. For example, during the 1984 drought in Sudan, Khartoum received only 4.7 mm of rain between May and October, Eltayeb (2003). This led to crop failure and consequently a famine hit Sudan which in turn led to migration of people in search of food and water. Floods reflect the other extreme in rainfall fluctuations. There are many factors which affect the severity of the flood, such as terrain slopes, soil types and amount of water in the soil. On the 4th of August 1988, Khartoum received 216 mm of rainfall during a 24 hour-period. This situation became disastrous when the Nile level also rose around 7 m above normal, which led to wide-spread property damage. These two natural extreme disasters were associated with significant anomalies in the Pacific sea surface temperature (SST): El Niño (1983) and La Niña (1988) events.

During the last few decades, there has been a wide recognition that natural oscillations in the state of the Pacific Ocean leave a significant impact on the patterns of weather and climate around the world, Amarasekera et al., (1997); Eltahir, (1999). The dominant among these oscillations is known as the El Niño – Southern Oscillation (ENSO) which has a return period of about 4 years. Though distant from Africa, ENSO is significantly correlated with rainfall variations over the eastern side of the African continent, but the signs of the correlations and their phase relative to the seasonal cycle vary from region to region, Camberlin et al. (2001). Eltahir, (1996) found that 25% of the natural variability in the annual flow of the Nile is associated with El-Niño oscillations and proposed to use this observed correlation to improve the predictability of the Nile floods. Wang and Eltahir, (1999) recommended an empirical methodology for medium and long-range (~6 months) forecasting of the Nile floods using ENSO information. Amarasekera et al., (1997) showed that ENSO episodes are negatively correlated with the floods of the Blue Nile and Atbara rivers which originate in Ethiopia. Eltahir, (1996) showed that the probability of having a low (high) flood flow given a cold SST condition is 2% (49%). On the other hand, the probability of having a high (low) flood flow given a warm SST condition is 8% (58%). De Putter et al., (1998) made a study of decadal periodicities of the Nile River historical discharge of Roda Nilometer (Cairo, Egypt). He suggested that high frequency peaks could be linked to the ENSO. Abtew et al., (2009) analyzed monthly rainfall observations from a 32-rain gauge monitoring network in the Upper Blue Nile Basin. He found that high rainfall is likely to occur during La Nina years and low rainfall conditions are likely to occur during El Nino years. He also found that extreme dry years are highly likely to occur during El Nino years and extreme wet years are highly likely to occur during La Nina years.

The Southern Oscillation Index (SOI) is a measure of air pressure difference between Tahiti in the east and Darwin, Australia to the west as compared to historical average of the same difference. Negative differences indicate El Niño conditions as lower pressure in the eastern Pacific is associated to warmer water and weakened easterly trade winds, and positive SOI corresponds to negative SST index and La Niña. Seleshi and Zanke (2004) reported that June to September rainfall of the Ethiopian highlands is positively correlated to the Southern Oscillation Index (SOI) and negatively correlated to the equatorial eastern pacific SST.

Many studies tried to use oceanic and atmospheric variables as predictors in seasonal hydrologic forecasting over East Africa, but none of the studies had a focus on the June to September rainfall in Ethiopia (Mutai et al.1998; Hastenrath et al. 2004; Philippon et al. 2002; Yeshanew and Jury 2007; Mwale and Gan 2005; Williams and Funk, 2011; Williams and Funk, 2010). In this study, we analyze river flow, and rainfall observations, and we evaluate the impact of El Niño on the drought and flood in the upper catchment of the Blue Nile. We identify for the suitable seasonal SST conditions over the Pacific Ocean to be recommended as input to seasonal forecasting by water resources managers in the region. A successful seasonal forecasting system would have great economic and social value.

4.2 DATA AND METHODS

4.2.1 Observed data

Discharge measurements between 1965 and 2011 from Eldiem station (Figure 4-1) was used in this study. This station is located at the border between Sudan and Ethiopia around 120 km upstream from El Rosieres dam (Figure 4-1). The gauge station measures water level and discharge at the outlet of the upper catchment of the Blue Nile. The data at Eldiem station from 1997 to 2001 was missing. These missing data points were filled by using the nearest station to Eldiem station, (Rosieres), with no contributing tributaries in between. The discharge data represents the catchment hydrology better than the rainfall data from scattered set of stations. Duethmann et al., (2012) concluded that the rainfall data has relatively large uncertainty due to errors in measurement, wind, and high spatial variability of precipitation in the mountainous region. The density of the rain gauges network is often low, and the gauges are often unequally distributed.

For El Niño, Niño 3.4 index between 1965 and 2011 was downloaded from NOAA website (http://www.cpc.ncep.noaa.gov/products/analysis_monitoring/ensostuff/ensoyears.shtml). An El Nino event is identified if 5-month running mean of sea surface temperature (SST) anomalies in the Niño 3.4 region (5°N–5°S, 120°–170°W) exceeds 0.4°C for 6 months or more, Trenberth, (1997). Data from Niño 3.4 region was analyzed in relation to several observational datasets (GPCP rainfall and discharge flow).

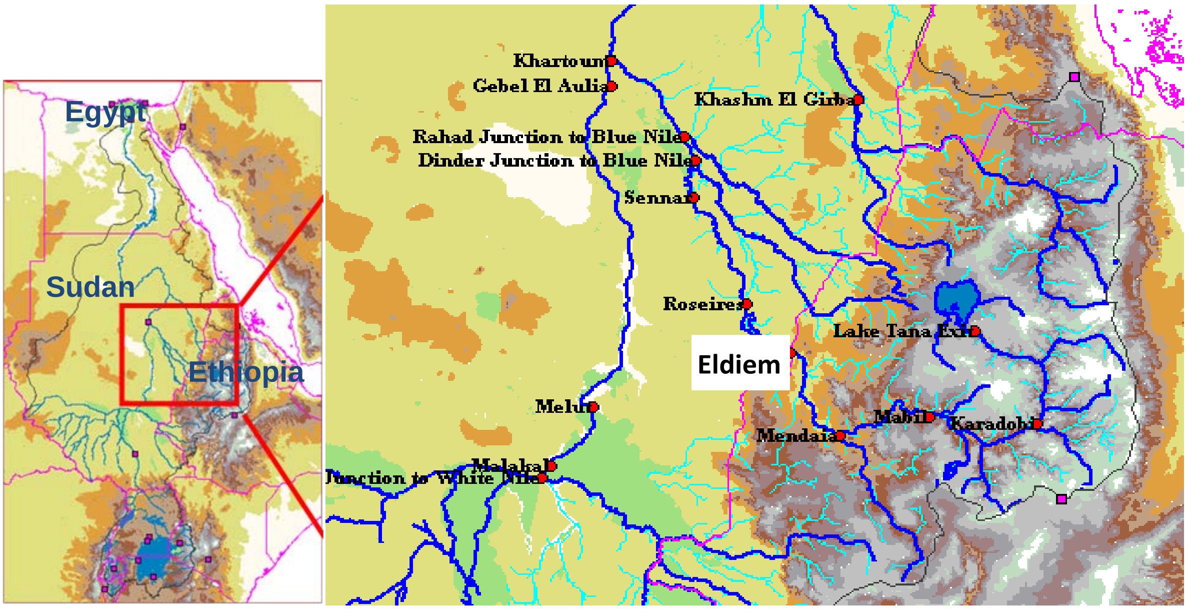

Figure 4-1: The topography and geography of cities in the region.

A global dataset of monthly precipitation was selected. The Global Precipitation Climatology Project (GPCP) version 2.2 (Huffman et al. 2011) is available from January 1979 to December 2010 with a resolution of 2.5°.

4.3 RESULTS AND DISCUSSION

The discharge at Eldiem station and its association with El Niño and La Niña years is shown in Figure 4-2. El Niño years like 1972 and 1987 as shown in the upper panel are associated with low discharge, and La Niña years, for example 1988 as shown in the upper panel are associated with high discharge. The lower panel shows the whole time series of Eldiem station. In the lower panel the red colour in the time series represents El Niño months, the Blue colour represents La Niña months, and the green colour represents normal months.

This confirms the results of previous studies that El Niño is associated with below average rainfall, and La Niña is associated with above average rainfall, (Eltahir, 1996); (Wang and Eltahir, 1999); (Amarasekera et al., 1997); De Putter et al., (1998); Camberlin et al. (2001); Abtew et al., (2009).

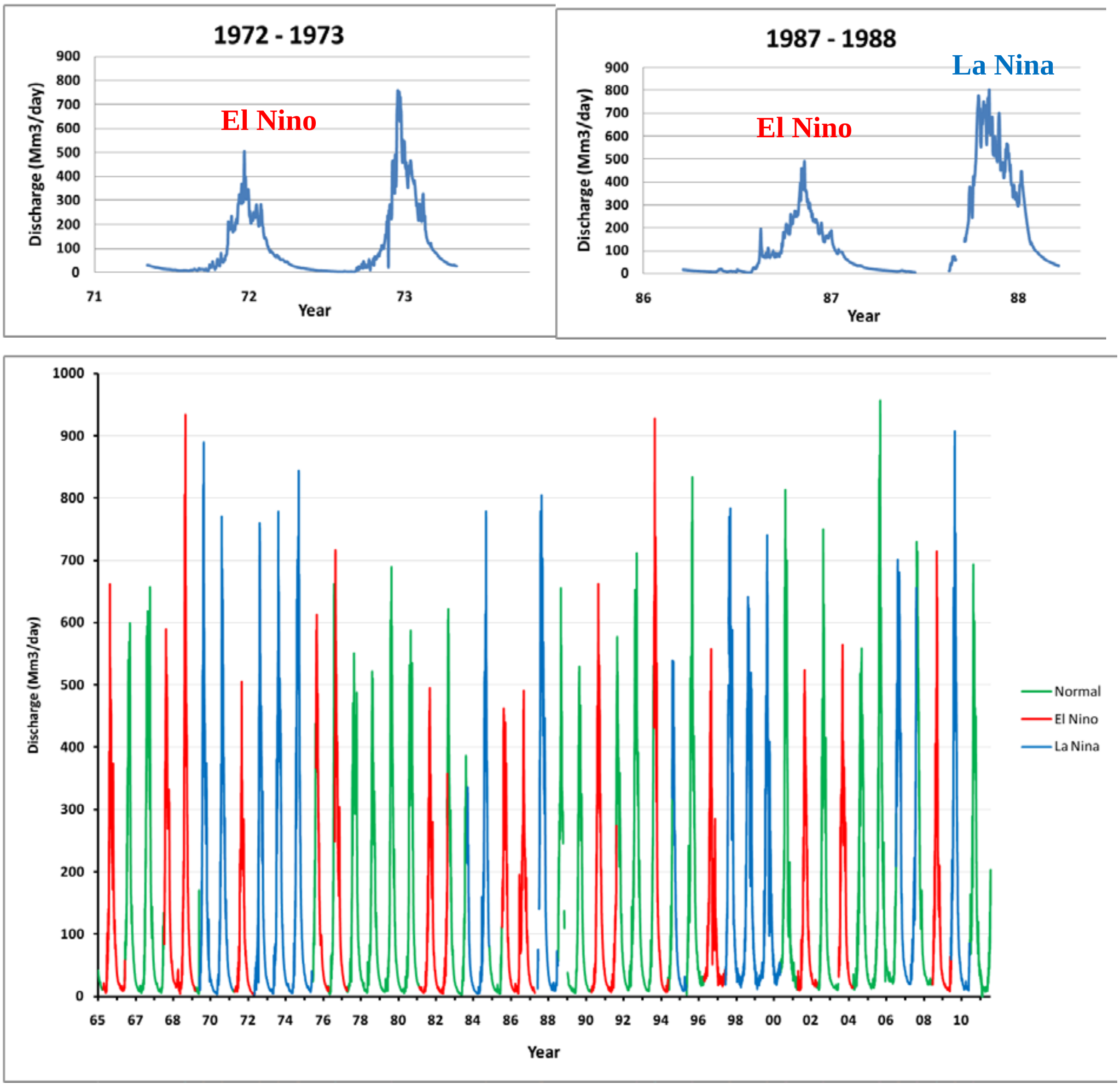

Figure 4-2: The discharge of the Blue Nile at Eldiem station (1965-2009) and its association with El Niño and La Niña years.

4.3.1 Teleconnections of Pacific SST and the discharge observation at Ediem station.

The seasonal discharge anomalies for (June, July, August, and September) JJAS are shown in Figure 4-3. Some thresholds were assumed in this study: any discharge anomaly above 6.813 km^3 was considered as extreme flood which is 1 * standard deviation, and any discharge anomaly below – 6.813 km^3 considered as a extreme drought, and any discharge anomaly between 3.407 km^3 (0.5* standard deviation) and 6.813 m^3 considered as flood, and any discharge anomaly between – 3.407 km^3 and – 6.813 km^3 considered as a drought. Finally, any discharge anomaly between – 3.407 km3 and 3.407 km3 was considered normal. The normal event covers around 38 % of the normal distribution curve. Drought and flood cover from 38 % to 68 % of the normal distribution curve. The extreme drought and extreme flood cover the range of 32%. This classification is in line with observed floods and droughts in this region, and in line with the classification of the Ministry of Water Resources and Electricity of Sudan. For example, in Figure 4-3, nine extreme floods can be identified, and among them there are three at or close to record floods in 1988, 2006 and 2007. There are six extreme droughts, four floods, and ten droughts.

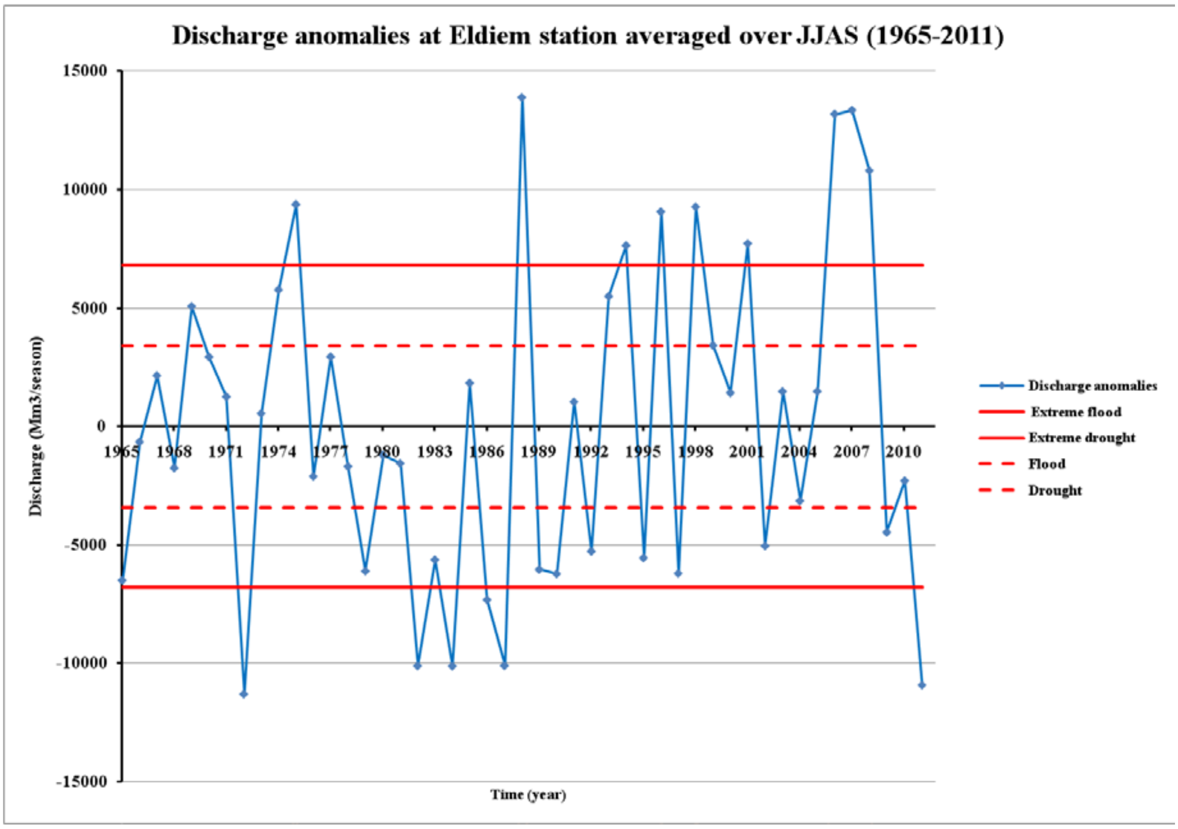

Figure 4-3: The discharge anomalies at Eldiem station averaged over JJAS (1965-2011), the red line represent the threshold for the extreme flood/ drought, and the dashed red line represents the threshold for drought/ flood.

The negative correlation between the SST anomalies in Pacific Ocean in Nino 3.4 region and the discharge anomalies in Eldiem station during JJAS is evident in Figure 4-4. The right axis represents the SST anomalies during AMJ in the middle panel, and the left axis represents the discharge anomalies during JJAS. The upper panel represents SST anomalies during JFM, and the lower panel represent JAS. The same plot was made with different SST anomalies for other seasons; FMA, MAM, MJJ and JJA (not shown here), and they showed less negative correlations compare to AMJ season. Figure 4-4 illustrates that the rainfall in the upper catchment is highly sensitive to the SST during AMJ. For example the big El Nino of 1987 associated with below average discharge and La Nina of 1988 associated with above average discharge.

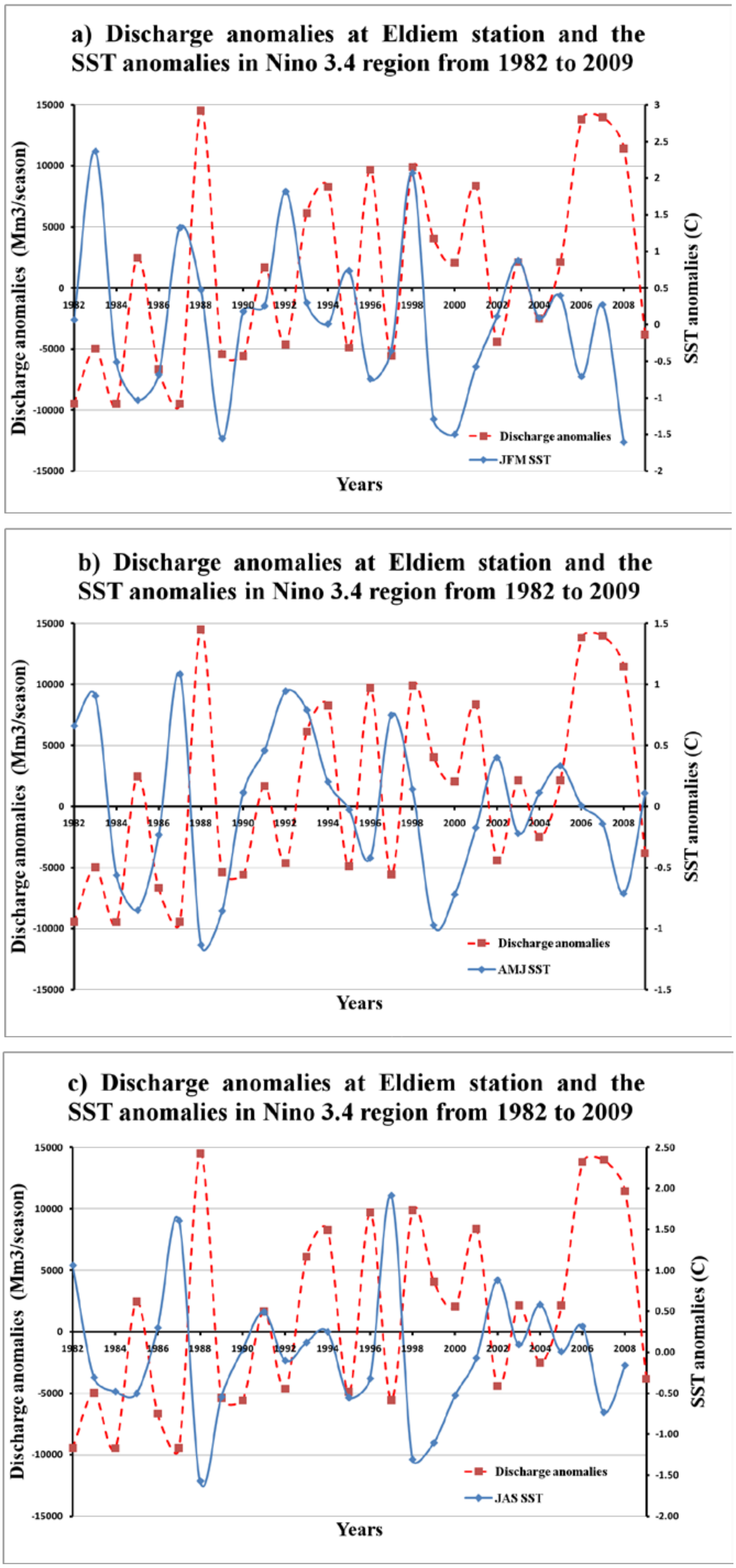

Figure 4-4: The SST anomalies during (a) JFM, (b) AMJ, and (c) JAS in Nino 3.4 region and the discharge anomalies in Eldiem station.

The impact of start date of El Niño

The impact of start date of El Niño on the drought of the upper catchment of the Blue Nile was investigated by evaluating the relationship between Niño 3.4 for different seasons, and the rainfall anomaly in the upper catchment of the Blue Nile during June to September (JJAS) for each year respectively. The first column in Table 4-1 shows the starting season of El Niño, the second column indicates whether there was an extreme drought, the third column if there was a drought, and the fourth column if there is no drought in the upper catchment of the Blue Nile. The flow year column refers the start year of each El Niño event. The length column refers to the number of months during that El Niño.

Table 4-1: The effect of the start date of El Niño on the drought of the upper catchment of the Blue Nile during JJAS of the same year.

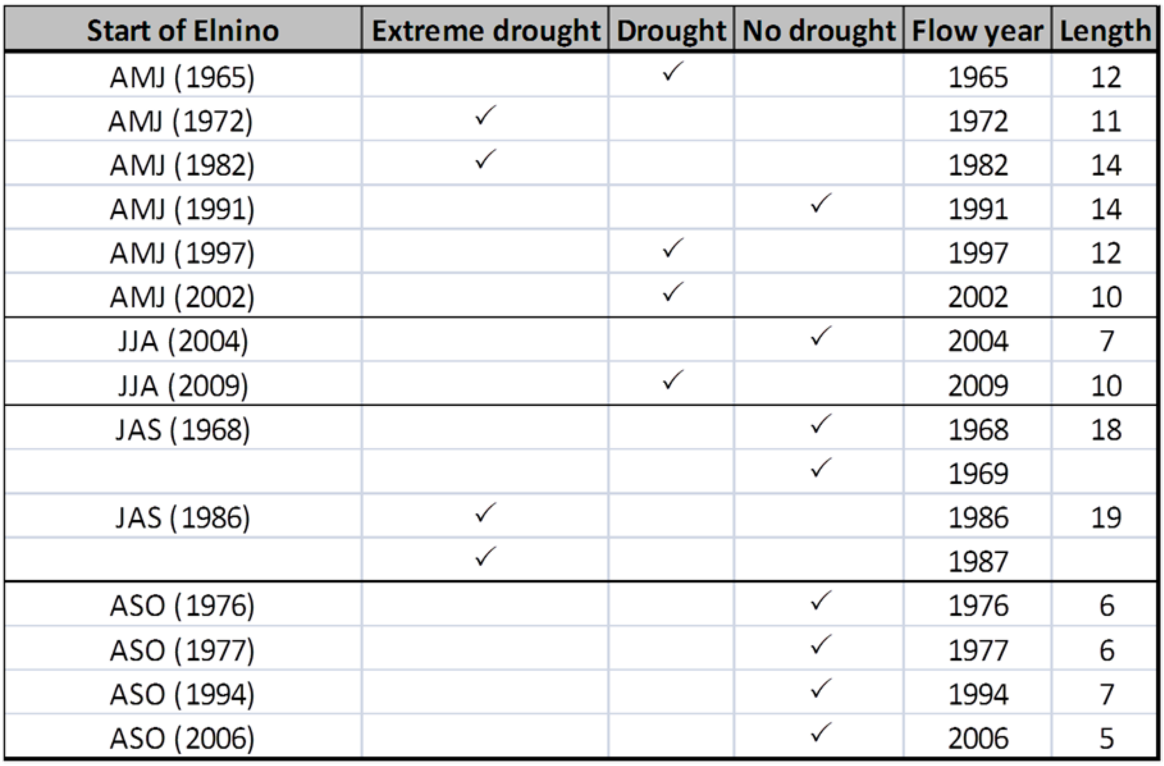

Start of Elnino	Extreme drought	Drought	No drought	Flow year	Length
AMJ (1965)		✓		1965	12
AMJ (1972)	✓			1972	11
AMJ (1982)	✓			1982	14
AMJ (1991)			✓	1991	14
AMJ (1997)		✓		1997	12
AMJ (2002)		✓		2002	10
JJA (2004)			✓	2004	7
JJA (2009)		✓		2009	10
JAS (1968)			✓	1968	18
			✓	1969	
JAS (1986)	✓			1986	19
	✓			1987	
ASO (1976)			✓	1976	6
ASO (1977)			✓	1977	6
ASO (1994)			✓	1994	7
ASO (2006)			✓	2006	5

From Table 4-1 there are six events when El Niño started in AMJ. When El Niño started in AMJ, there was an extreme drought twice, 3 droughts and only one year with normal condition. When El Niño started in JJA, there was only 1 drought out of two events. The longest two El Niño events occurred when El Niño started in JAS. When El Niño started in JAS there was no drought on the same year, but the discharge was below average, and there was one drought event. When El Niño extends to the whole next year, there was one extreme drought (in 1987), and one normal year (in 1969). When El Niño started late in ASO, it tends to be relatively short, and there was no drought event (in the same year) for four times, among them one normal flood and one extreme flood.

From the above results and Table 4-1, we found that the upper catchment of the Blue Nile is very sensitive to El Niño events starting in AMJ. When El Niño started in AMJ, 5 out of 6 cases there was a drought. When El Niño started in JJA or JAS, 50% of the cases there was a drought. If we look at these three seasons in total (AMJ, JJA and JAS), in 70% of the cases, there was a drought in the upper catchment of the Blue Nile, in 20% of the cases the discharge was below average, and only in 10 % of the cases no drought was observed. When El Niño starts late (ASO), there are no drought effects in the Blue Nile.

This analysis is consistent with the hypothesis that El Nino impacts the global monsoon, Diaz and Markgraf, (2000). In addition, when El Nino starts in early (AMJ, JJA JAS) it has a big impact in East African monsoon and suppressed the rainfall in the upper catchment of the Blue Nile. However, when El Nino started late it has no impact in East African monsoon.

The impact of start date of La Niña.

La Niña is normally associated with floods in the upper catchment of the Blue Nile (Eltahir, 1996); (Wang and Eltahir, 1999); (Amarasekera et al., 1997). In this section the start date of La Niña season will be explored, along with its effect on the flooding of the upper catchment of the Blue Nile in the same year. The first column in Table 4-2 shows the season of the start of La Niña. From Table 4-2, it is clear that La Niña events can last for up to three years, as in 1973-1975 and 1998-2000.

When La Niña started in AMJ of 1988, there was one extreme flood (in the same year), when it started in AMJ of 1973 and extended for 3 years ,there was no flood (in the same year), and one flood and one extreme flood in the following years. When La Niña started in JJA, there was no flood in 1970 and no flood in 2010, and there was an extreme flood in 1998. When La Niña started in JAS of 2007, there was an extreme flood. When La Niña started late in ASO, there were no floods recorded, and in one event there was even a strong drought in 2011. So, in general when La Niña started in AMJ, JJA and JAS, 50 % of the times there would be a flood or extreme flood. This result is in line with the result of impact of start of El Niño, the rainfall and the monsoon in this catchment is sensitive to AMJ, JJA and JAS SST in the Pacific Ocean.

When La Niña extended for the next year, years or at least 9 months of the next year, there were no floods two times (all of them above average), two times there was a flood, and one time an extreme flood in 1975. That means if La Niña extends to the next year, there was no drought or even below average discharge. So, there is a low possibility to have a drought.

Table 4-2: The effect of the start of La Niña in the flood of the upper catchment of the Blue Nile.

Start of La Nina	Extreme flood	Flood	No flood	Flow year	Length
AMJ (1973)			✓	1973	36
		✓		1974	
	✓			1975	
AMJ (1988)	✓			1988	13
JJA (1970)			✓	1970	18
			✓	1971	
JJA (1998)	✓			1998	33
		✓		1999	
			✓	2000	
JJA (2010)			✓	2010	10
JAS (2007)	✓			2007	11
	✓			2008	
ASO (1983)			✓	1983	5
ASO (1995)			✓	1995	7
ASO (2011)			✓	2011	7

El Niño followed by La Niña events

In the last 40 years when El Niño was followed by La Niña there were extreme floods records in the upper catchment of the Blue Nile in 1988, 1998 and 2007. When El Niño was followed by La Niña, in 50 % of the cases there were extreme floods as shown in Table 4-3. The red box represents the end of El Niño period, and the blue box represents the start of La Niña. If we look at the period from the 1980s to present, it can be concluded that when El Niño is followed by La Niña, there is a 75% chance of extreme flood in the Blue Nile.

In these 47 years there were 9 extreme floods, so the probability of having an extreme flood in any year is 19 %. If however we have additional knowledge about having a La Niña year, this probability of an extreme flood increases. Here we have 13 La Niña years, among them 5 extreme floods were observed; hence the corresponding probability increases to 38 %. As shown above, when El Niño is followed by La Niña year the probability increased further to 50 %.

Table 4-3: El Niño followed by La Niña and extreme flood.

Year	DJF	JFM	FMA	MAM	AMJ	MJJ	JJA	JAS	ASO	SON	OND	NDJ	Remark
1970	-						+						Low flood
1973			-		+								Above average
1988		-			+								**Extreme flood**
1998				-			+						**Extreme flood**
2007	-							+					**Extreme flood**
2010				-			+						Below average

The severity of El Nino and its impact on the upper catchment of the Blue Nile

There were three strong El Niño in the last 50 years. We consider in this study any El Niño index from 2 and above as a strong El Nino. The strong ones were in 1972, 1982 and 1997. During the strong El Niño of 1972 and 1982 there were extreme droughts. During the strong El Niño of 1997 there was a normal drought. On the other hand, in the longest normal El Niño of 1987, there was extreme drought. In 1984 and 2011, there was no El Niño observed, but there was extreme drought. Hence, it is also possible that there may be a strong drought without any El Niño, and this could be attributed to some local and regional process.

4.3.2 The correlation between Nino 3.4 and the GPCP precipitation observations

In the previous sections we evaluated the relations between Nino 3.4 and discharge at the upper catchment of the Blue Nile. Figure 4-5 shows the rainfall anomalies over the upper catchment of the Blue Nile during JJAS from 1982 to 2008, and the discharge anomalies at Eldiem station during JJAS. GPCP captures well the general trend of almost all the droughts and floods. However, GPCP overestimated the rainfall in 1989 and 1990, and did not capture the extreme floods in 2006, 2007 and 2008.

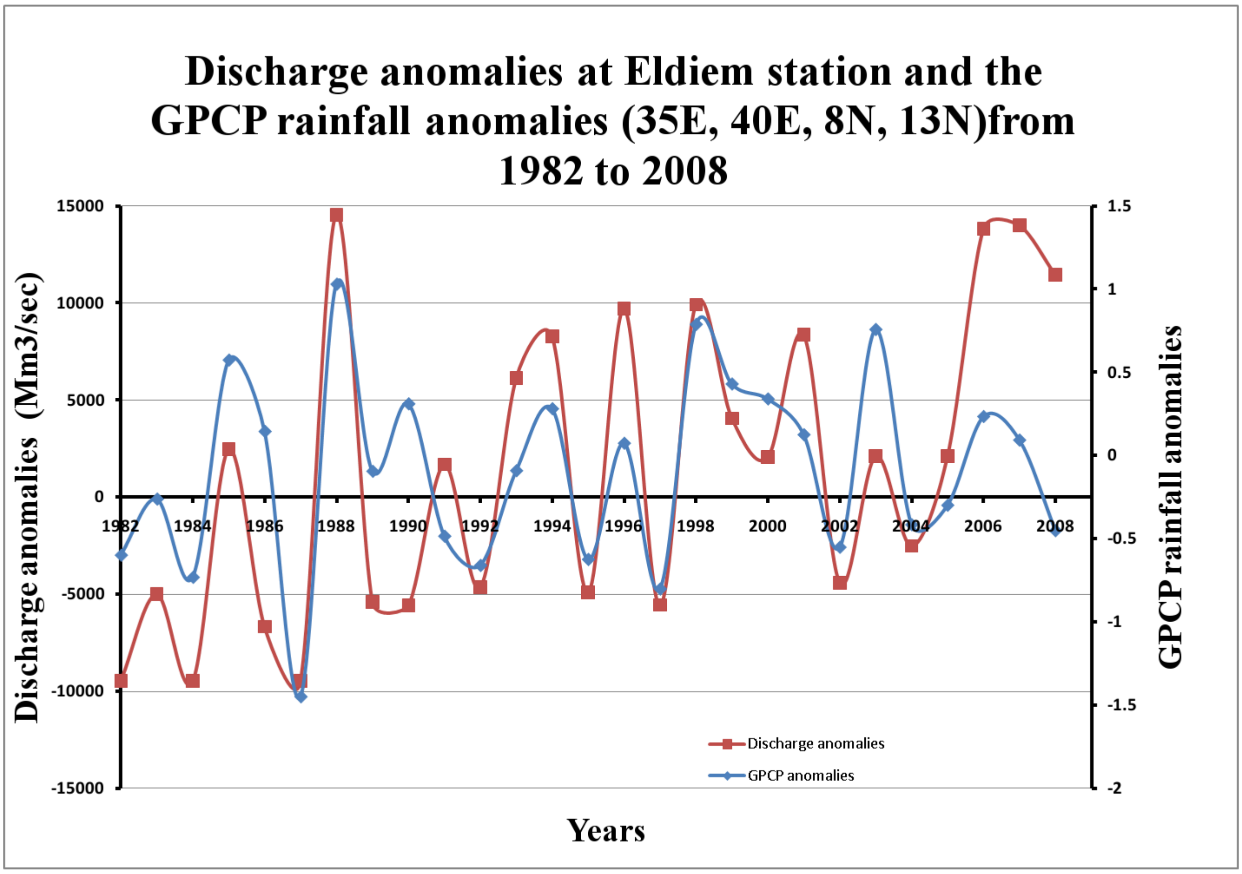

Figure 4-5: Rainfall anomalies over Ethiopian Highlands during JJAS.

The correlation between the SST anomalies in Niño 3.4 during different seasons was calculated for all the years regardless of El Niño or La Nina years against the rainfall over Ethiopian Highland from the GPCP as shown in Figure 4-6. The correlation of SST with Eldiem discharge data is also presented in the same figure. The negative and lowest correlations by the GPCP were found during JFM season (-0.14), the negative correlation increased gradually until JJA (-0.72), and the correlation decreased gradually again until OND (-0.48). The GPCP shows almost similar trend like the discharge correlation. However, GPCP shows a higher correlation compared to the discharge data.

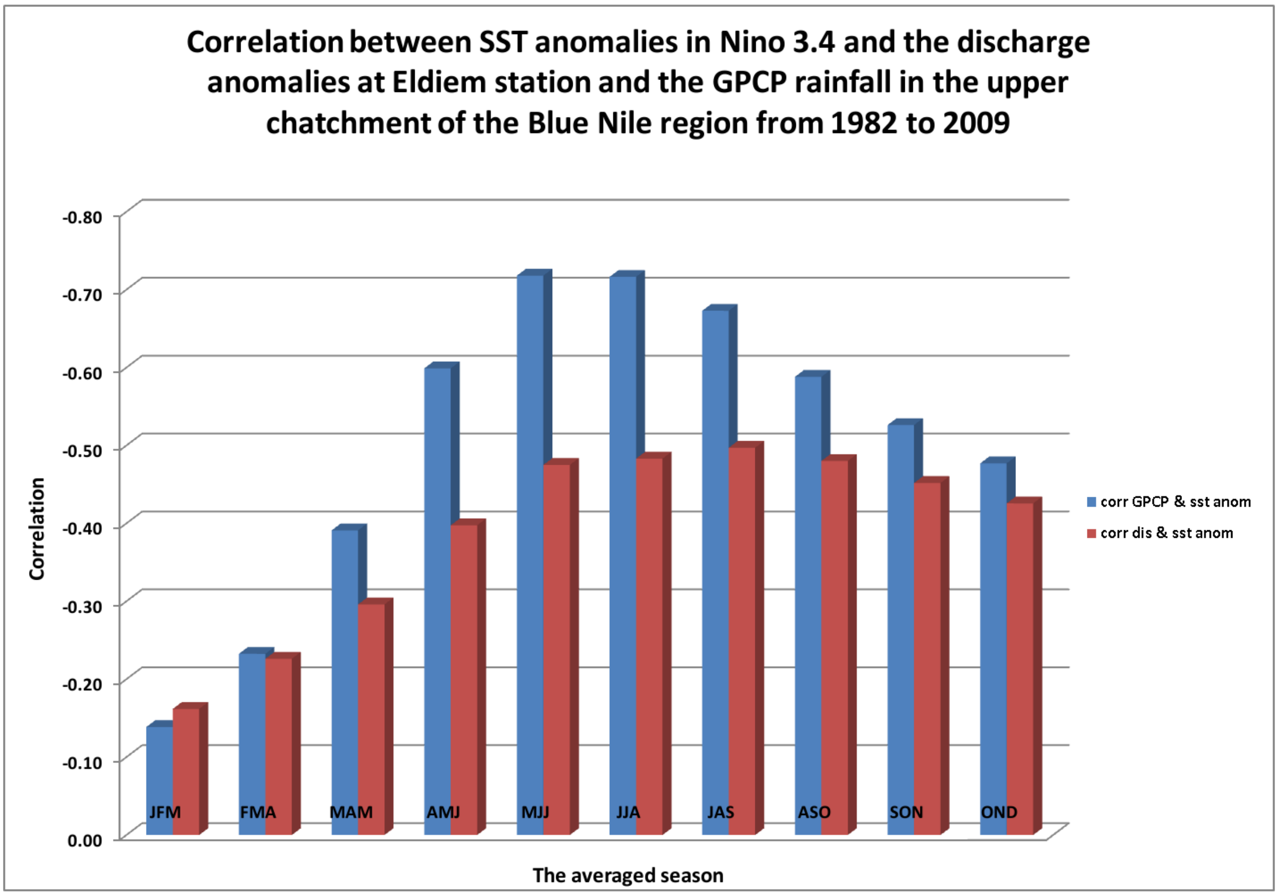

Figure 4-6: Correlation between SST anomalies in Nino 3.4 region and the upper catchment of the Blue Nile in Ethiopian Highlands from 1982 to 2008.

The 95% significant 2 tailed test was made for the correlation between the SST anomalies in Nino 3.4 and the GPCP rainfall in the upper Blue Nile and discharge at Eldiem as shown in Figure 4-7. The points below the red line represents the null hypothesis of no relationship (cannot be rejected). The values above the red line means the null hypothesis is rejected and the relationship exist between SST anomalies and discharge or GPCP rainfall. From Figure 4-7, the correlation in JFM and FMA is not significant for GPCP and discharge, and the correlation in MAM is not significant only the discharge.

The correlation is significant for MAM for GPCP and significant for AMJ, MJJ, JJA, JAS, ASO, SON and OND for the GPCP and discharge.

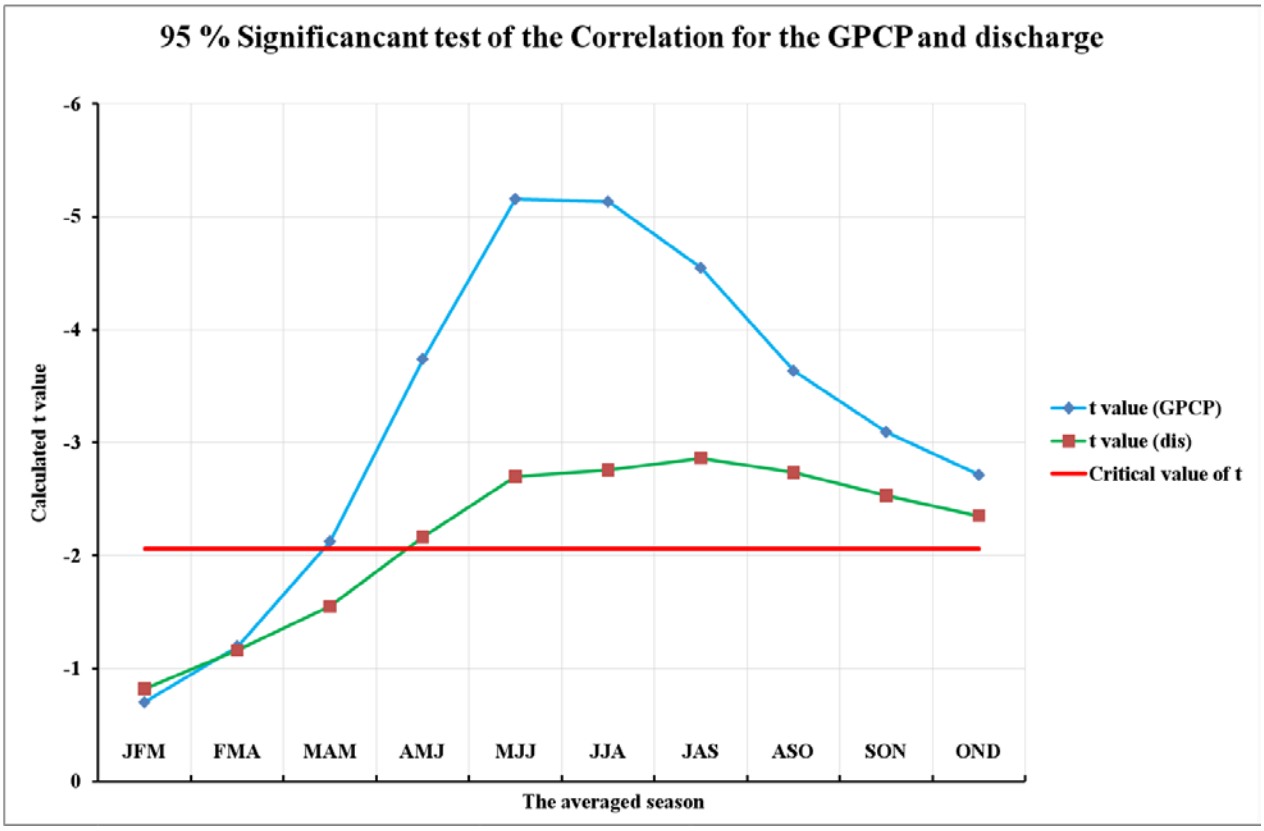

Figure 4-7: 95% significant test of the correlation for the GPCP and discharge.

4.4 CONCLUSION

Rainfall has a great impact on the social and economic life in the region. Scarcity in rainfall leads to drought while excessive, intense rainfall may lead to floods. Ethiopian rainfall is highly variable, both temporally and spatially, the rainfall seasonality varies greatly from one region to another, Gissila et al., (2004). The Blue Nile contributes around 67% of the main Nile discharge. The natural oscillations in the state of the Pacific Ocean leave a significant impact on the patterns of weather and climate around the world. The role of global sea surface temperatures in shaping the potential predictability of rainfall over tropical East Africa has been thoroughly assessed in both observational discharge at the mouth of the upper catchment of the Blue Nile and GPCP dataset, and inferring that ENSO exerts a significant influence to the upper catchment of the Blue Nile.

The negative correlation between the SST anomalies in Pacific Ocean in Nino 3.4 region and the discharge anomalies in Eldiem station at the outlet of the upper catchment of the Blue Nile during JJAS is evident. Droughts in the Blue Nile are sensitive to El Niño, with 70% of drought cases when El Niño starts in AMJ, JJA and JAS. When El Niño starts in AMJ, 83 % of the cases resulted in drought. When El Niño ends early (DJF, JFM, FMA and MAM), there is almost no effect on the drought in the Blue Nile. When El Niño terminates late in MJJ (or after that) there is a high possibility of drought occurrence in the Blue Nile. This analysis is consistent with the hypothesis that El Nino impacts global monsoon, Diaz and Markgraf, (2000).

When La Nina started in AMJ, JJA and JAS, in 50 % of the cases there was a flood or extreme flood. There has to be an active event El Nino / La Nina during the season for development of the monsoon over Ethiopia (May to September), for this teleconnection to have an impact.

In 50 % of the cases that El Niño was followed by La Niña there were extreme floods in the Blue Nile.

The important conclusion is that JJAS rainfall in the upper catchment of the Blue Nile is highly sensitive to the SST in the early season of AMJ in Nino 3.4. This season is recommended by this study be used in the seasonal forecasting of the Blue Nile.

5. THE CONNECTIONS OF ENSO AND DROUGHT AND FLOOD OVER THE UPPER CATCHMENT OF THE BLUE NILE BY USING 9 AVERAGE MEMBERS

5.1 INTRODUCTION

During the last few decades, there has been a wide recognition that natural oscillations in the state of the Pacific Ocean leave a significant impact on the patterns of weather and climate around the world. The dominant among these oscillations is known as the El Niño – Southern Oscillation (ENSO) which has a period of about 4 years. (Eltahir, 1996) found that 25% of the natural variability in the annual flow of the Nile is associated with El-Niño oscillations and proposed to use this observed correlation to improve the predictability of the Nile floods. (Wang and Eltahir, 1999) recommended an empirical methodology for medium and long-range (~6 months) forecasting of the Nile floods using ENSO information. (Amarasekera et al., 1997) showed that ENSO episodes are negatively correlated with the floods of the Blue Nile and Atbara rivers which originate in Ethiopia. (Eltahir, 1996) showed that the probability of having a low (high) flood given a cold SST condition is 2% (49%). On the other hand, the probability of having a high (low) flood flow given a warm SST condition is 8% (58%). The previous studies were conducted by using observational dataset. In this study, we analyze observational data sets also, and we evaluate the hypothesis whether a similar connection can be formed between droughts/ floods and Sea Surface Temperature in the Pacific Ocean by using a physically based model of the climate system (the Regional Climate Model (RegCM4.1.1)) (Giorgi et al., 2012). We simulate an ensemble of 9 members describing the regional climate to study the impact of El Niño on the drought and flood in the upper catchment of the Blue Nile.

5.2 REGCM4 MODEL DESCRIPTION

RegCM4.1 Elguindi et al., (2011) reflects an evolution of the previous version, RegCM3, described by Fischlin et al., (2007). RegCM4.1 is a hydrostatic, sigma-p vertical coordinate model with multiple physics options. For this experiment we used the options described in Giorgi et al., (2012): modified CCM3 radiative transfer scheme Kiehl et al., (1996), modified Holtslag et al., (1990) planetary boundary layer scheme, SUBEX resolvable precipitation scheme Pal et al., (2000), mixed cumulus convection configuration utilizing the scheme of Grell, (1993) over land and that of Emanuel, (1991) over oceans and the biosphere−atmosphere transfer scheme Dickinson et al., (1993) land surface package. Therefore, the model uses forcing lateral BC only in the northern and southern boundaries of the domain, with no external forcing in an east−west direction. The horizontal resolution of the model is 125 km. In a north−south direction the domain extends from about 50° S to 50°

N, and a standard exponential relaxation procedure Giorgi et al., (1993a) are used in the southern and northern boundaries over a buffer zone with 12 grid points width. The model simulate processes over a latitudinal belt that extends for 360° around the earth. The model has 18 vertical sigma levels and a top at 50 hPa, as in its standard configuration.

The initial and lateral boundary conditions for the RegCM4.1 simulations were obtained from the ERA-Interim 1.5° × 1.5° gridded reanalysis (ERAI, Dee et al. 2011) which is the third generation ECMWF reanalysis products. RegCM4.1 was forced with sea surface temperatures (SSTs) 1° resolution, and a weekly temporal resolution, obtained from the National Oceanic and Atmospheric Administration (NOAA) Optimum Interpolation (OI) SST dataset (Reynolds et al., 2007). The simulation period was from 1 January 1982 to 31 March 2010.

The data used for model validation was the Global Precipitation Climatology Project daily precipitation dataset (GPCP; Huffman et al. 2011) and the CRU dataset for precipitation, the CRU dataset for temperature, the NOAA Outgoing Long-wave Radiation (OLR) for outgoing long-wave radiation, and the ERAI dataset for wind.

5.3 MODEL VALIDATION

5.3.1 Rainfall climatology

The spatial patterns of seasonal precipitation have been validated in this part. Figure 5-1 compares averaged JJAS CRU and GPCP precipitation (Figure 5-1a, b) with the corresponding RegCM4.1 field (Figure 5-1c). Also shown are the differences between the RegCM4.1 field and the two observational datasets (Figure 5-2a, b). In JJAS, the ITCZ approaches its northernmost location. Therefore, observed precipitation (CRU and GPCP) (Figure 5-1a, b) over the continent is mostly confined between 7°S and 18°N, while regions above and below these latitudes are predominantly dry. This pattern of precipitation is mainly associated to the occurrence of propagating the mesoscale convective system related to the dynamics of African Easterly Jet (AEJ), African Easterly Waves (AEW), and Tropical Easterly Jet (TEJ) (d’Amato and Lebel 1998; Jenkins et al. 2005). The CRU data exhibit two precipitation maxima around Cameroon Mountains, and Ethiopian Highlands which are associated with local orographic features, while GPCP shows less rainfall over the Ethiopian Highlands and Cameroon Mountains, probably because of its coarse resolution. The model captures the general patterns of the observed rainfall distribution, in particular the ITCZ position and intensity. However, precipitation over southern Sudan, Central Africa and the Ethiopian Highlands is overestimated due to the orographic effect and the high convergence over this region. Also, the monsoon rain belt appears narrower in the model than in the two observation datasets. Our RegCM4.1 simulation appears reasonable. We also note that the performance of our model version appears in line with previous works performed using either the RegCM system in various configurations (Sun et al. 1999; Pal et al. 2007; Anyah and Semazzi 2007; Sylla et al. 2010b; Steiner et al. 2009; Zaroug et al. 2012) or other regional modeling systems (e.g., Vizy and Cook 2002; Nikulin et al. 2012; Paeth et al. 2005; Gallée et al. 2004; Flaounas et al. 2010; Druyan et al. 2008).

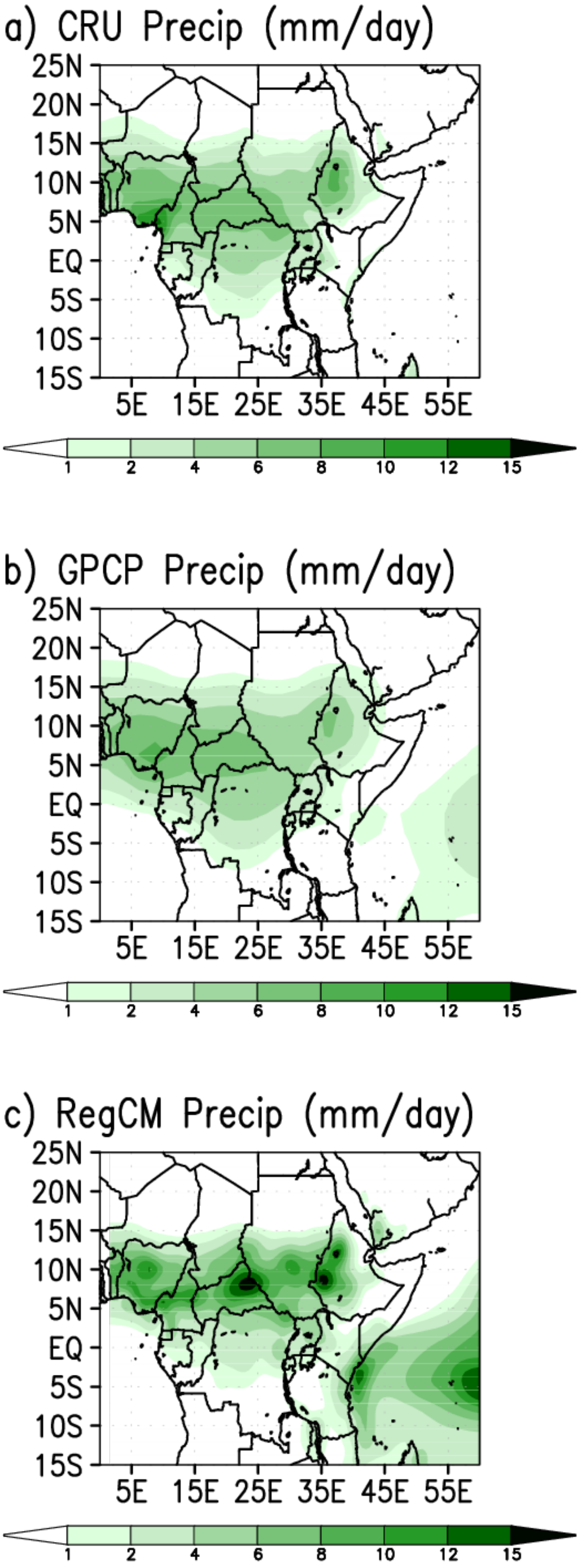

Figure 5-1: Averaged precipitation (in mm/day) for JJAS 1982-2009: a) CRU, b) GPCP, c) RegCM.

a) RegCM–CRU Precip (mm/day)

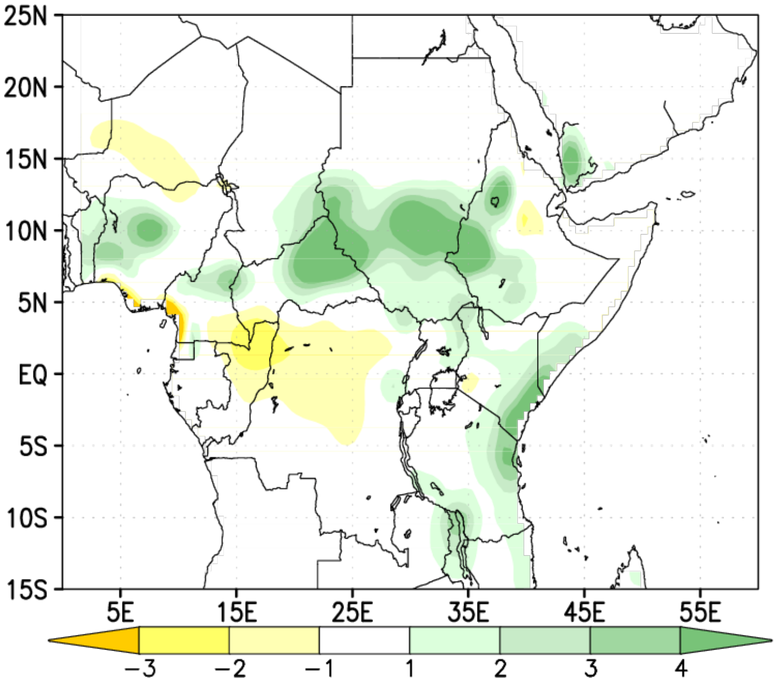

b) RegCM–GPCP Precip (mm/day)

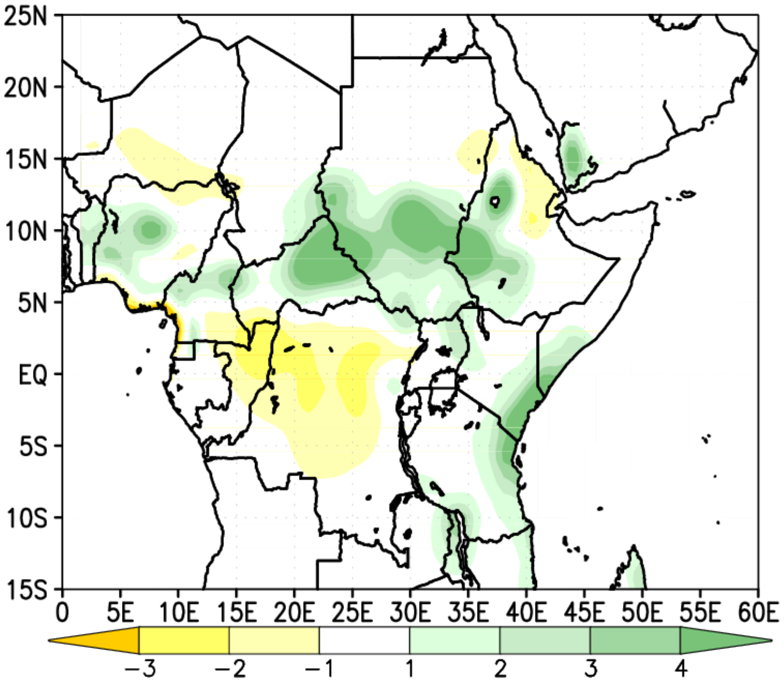

Figure 5-2: Averaged precipitation bias (in mm/day) for JJAS 1982-2009: a) RegCM – CRU, b) RegCM – GPCP.

5.3.2 Temperature climatology

The seasonal average of JJA 2-m temperature for 1982 to 2009 is illustrated in Figure 5-3. The figure presents CRU observations (Figure 5-3a), RegCM4.1-simulated values (Figure

5-3b), and the difference between CRU and RegCM4.1 (Figure 5-3c) temperatures. In JJA (Figure 5-3a), the CRU observations place the lowest temperatures mostly over the mountainous areas of Cameron and Ethiopian Highlands, Tanzania and south Kenya. The warmest areas are confined between 15 °N and 27 °N with larger values located over the Sahara desert. RegCM4.1 (Figure 5-3b) reproduces well this spatial pattern but it shows a systematic cold bias of a few degrees in the convective regions in East Africa (Figure 5-3c), Nigeria, Algeria and Libya. This cold bias over tropical and equatorial Africa has been a persistent feature in RegCM3, as also found for example in the experiments of Sylla et al. (2010b), although the magnitude of the bias is somewhat reduced in our simulation. It should be stressed that the CRU observations are possibly affected by large uncertainties in this region due to the relative sparseness of observing stations, particularly in remote areas (Mitchell et al. 2004). In addition, surface temperature depends on many parameters, such as albedo evapotranspiration rates, location and height of the observing gauges, etc., which are also highly uncertain, and on the presence of dust and aerosols. Given all these uncertainties, we assess that a model bias of a few degrees is acceptable in this study.

5.3.3 Outgoing long-wave radiation (OLR)

In this section, the spatial pattern of seasonal (JJA) OLR is validated. The OLR is validated against observations from the above mentioned NOAA dataset. Figure 5-4 shows the averaged JJA NOAA OLR (Figure 5-4a) and the corresponding RegCM4.1 field (Figure 5-4b) along with their difference (Figure 5-4c). Both the model and the observations (Figure 5-4a, b) exhibit larger (lower) OLR values in North Africa and south of 5 °S (along the ITCZ) because of smaller (larger) amount of cloud cover. Consistent with the Total Cloud Cover (TCC) results, simulated OLR is underestimated over the Congo basin due to an overestimation of TCC (Zaroug et al. 2012). Nevertheless, the model manages to capture generally well the general features of the OLR pattern in both magnitude and spatial extent.

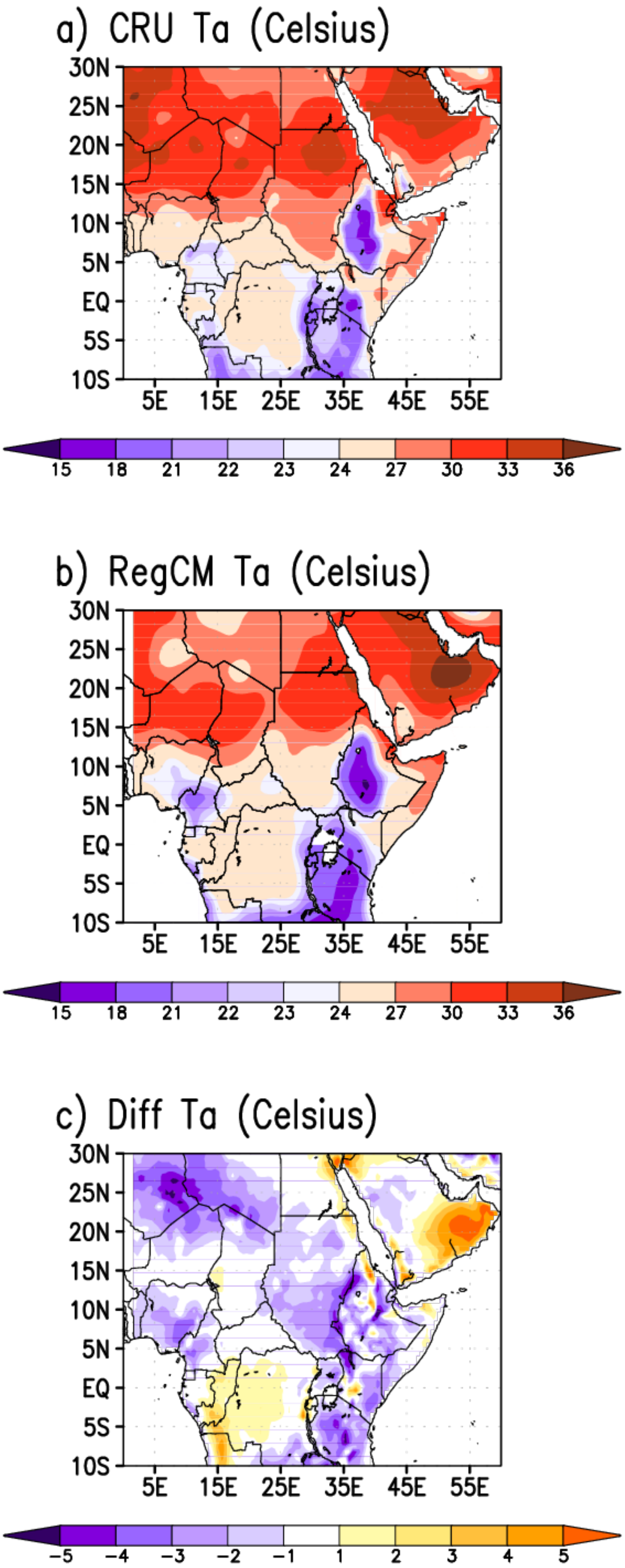

Figure 5-3: Averaged 2 m air temperature (in C) for JJAS 1982 – 2009: CRU, b RegCM, c RegCM minus CRU difference.

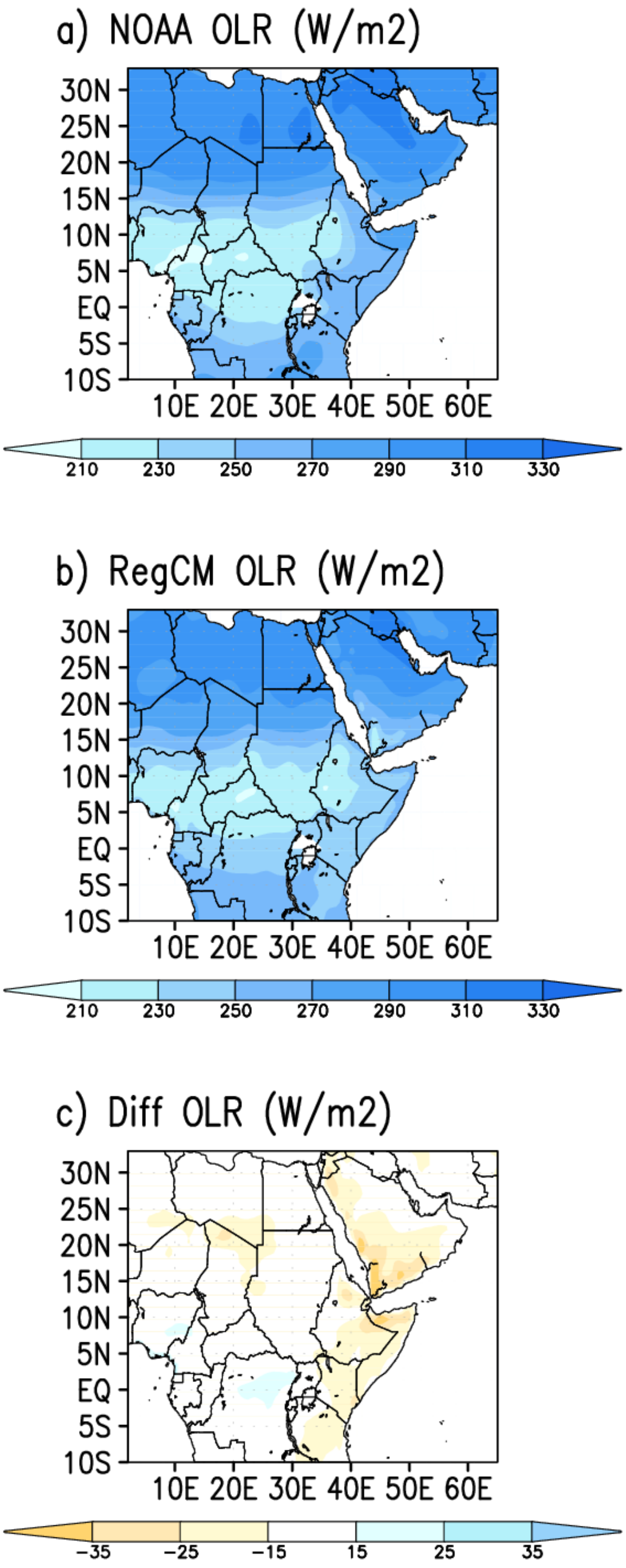

Figure 5-4: Averaged outgoing longwave radiation (in W/m^2) for JJAS 1982-2009: a NOAA, b RegCM, c NoAA minus RegCM.

5.3.4 Climatology of dynamical features

Low level circulation

The spatial patterns of average JJA low level (925 mb) circulation is shown in Figure 5-5a for the ERA Interim reanalysis and Figure 5-5b for the RegCM4.1 simulation. Direct observations of the low level wind over the region is not available, and thus, we use here the driving reanalysis (which is the closest information to reality that we have available) for model validation. Overall, the model reproduces well the main features of the low level circulation, such as the low level monsoon flow over North Africa, the northerly flow over East Africa and the south-easterly flow over the Horn of Africa. Overall, Figure 5-5 indicates that RegCM4.1 exhibits a good performance in the simulation of the low level circulation over the selected domain.

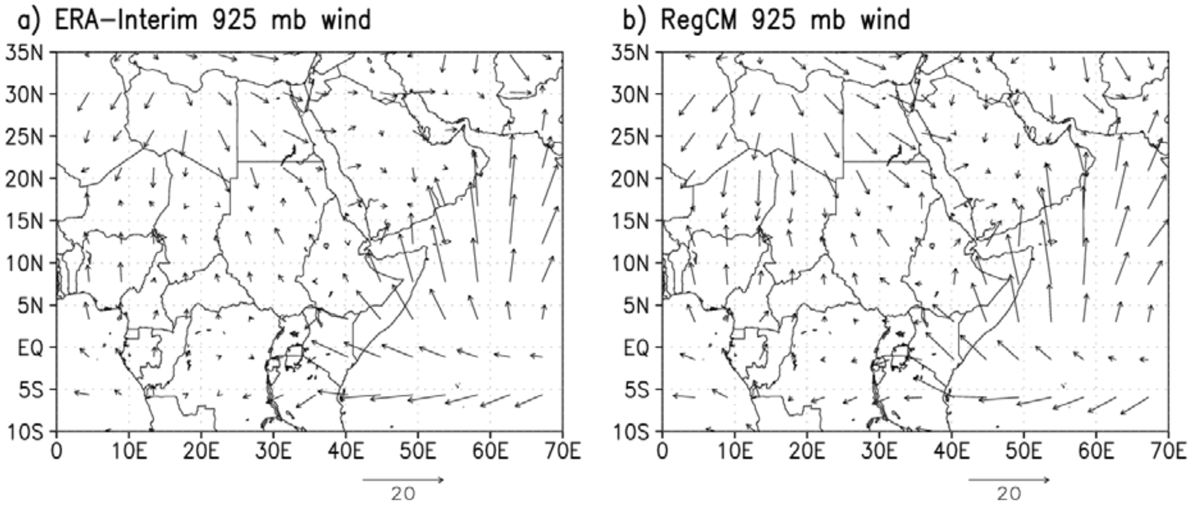

Figure 5-5: The black arrows show the averaged 925 mb wind vector for JJA 1982 – 2009: a ERA-Interim, b RegCM.

Tropical easterly jet (TEJ)

The TEJ develops between 200 and 150 mb in the upper troposphere over India in response to a large meridional thermal gradient and settles during the northern summer Asian monsoon season between the Tibetan Highlands and the Indian Ocean (Fontaine and Janicot 1992; Koteswaram 1958; Chen and van Loon 1987). It stretches from the Indochina peninsula, across the African continent, to the tropical Atlantic (Wu et al. 2009), and it is linked to anomalous SSTs on a planetary scale (Chen and van Loon 1987). The TEJ is one of the planetary features that contribute to the northern African summer climate variability (Chen and van Loon 1987). Figure 5-6a shows the TEJ in the ERA Interim reanalysis confined between 3 °N and 17 °N with a core speed exceeding 15 m/s. The band of the jet decreases gradually from East Africa to West Africa. In fact, the highest wind speed of about 18 m/s occurs over the Horn of Africa and the western Indian Ocean, while the lowest values of about 6 m/s are found over Niger. RegCM4.1 in Figure 5-6b reproduces well the structure of the TEJ shown in the ERA Interim reanalysis. It captures both the location and intensity of the jet. However, it extends the core of the jet with winds further to Sudan. In addition, it extends also the 12 m/s and 9 m/s zone further west.

African easterly jet (AEJ)

The AEJ results mainly from the vertical inversion (around 600–700 mb) of the meridional thermal gradient between the Sahara and equatorial Africa due to the existence of strong surface baroclinicity (Cook 1999; Steiner et al. 2009) associated with atmospheric deep convection (Thorncroft and Blackburn 1999; Sylla et al. 2010b). Figure 5-6c shows the ERA Interim zonal wind in JJA at 600 mb. It is confined approximately between 7° N and 20 °N extending from Chad to the Atlantic Ocean with a core speed ranging from 11 to 13 m/s located over West Africa (Zaroug et al. 2012). As for the TEJ, RegCM4.1 simulates reasonably well both the strength and location of the jet (Figure 5-6d).

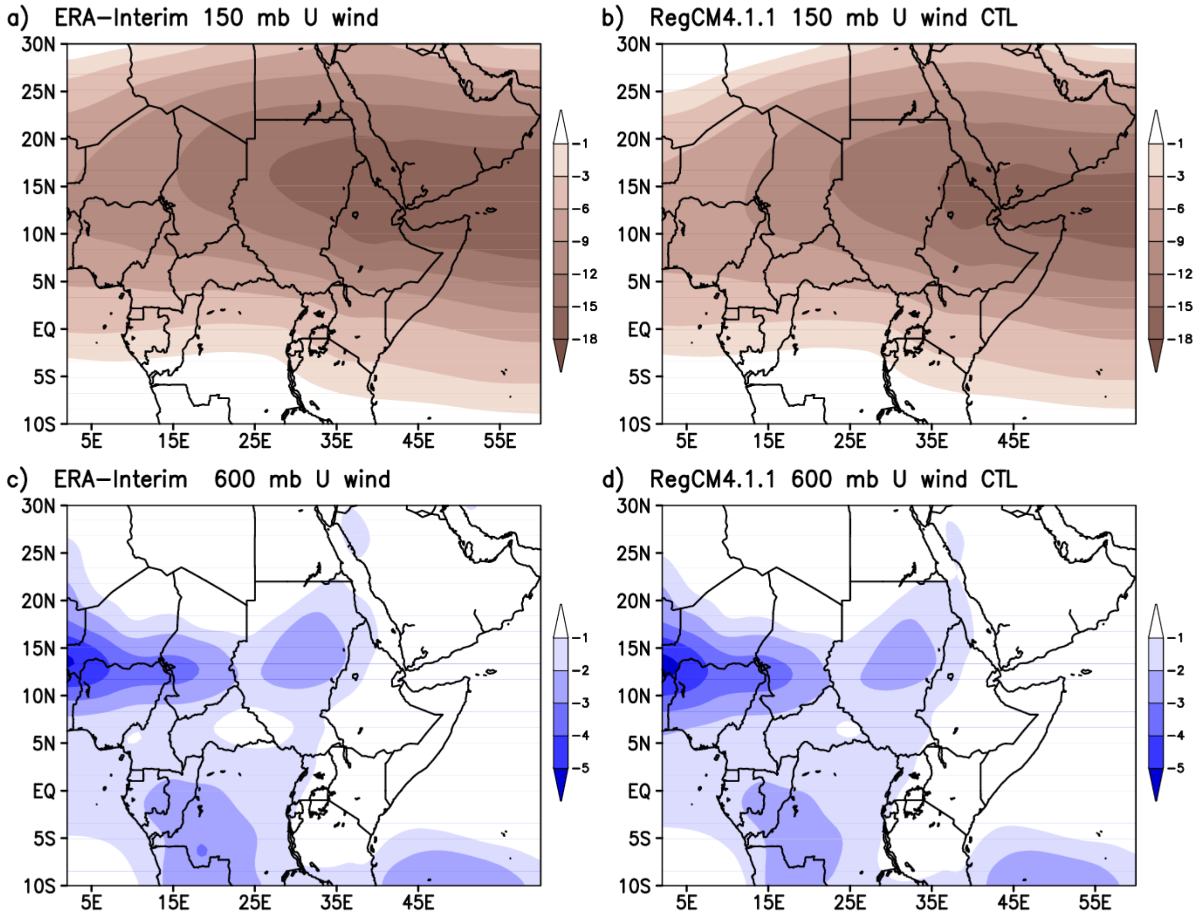

Figure 5-6: Averaged zonal wind (in m/s) for JJAS 1982 – 2009: a ERA Interim at 150 mb, b RegCM at 150 mb, c ERA Interim at 600 mb, d RegCM at 600 mb.

5.4 RESULTS AND DISCUSSION

5.4.1 The difference between La Niña and El Niño years in the model and in the GPCP observational data set

Figure 5-7 shows the model domain and topography along with some sub-regions selected for more detailed regional analysis.

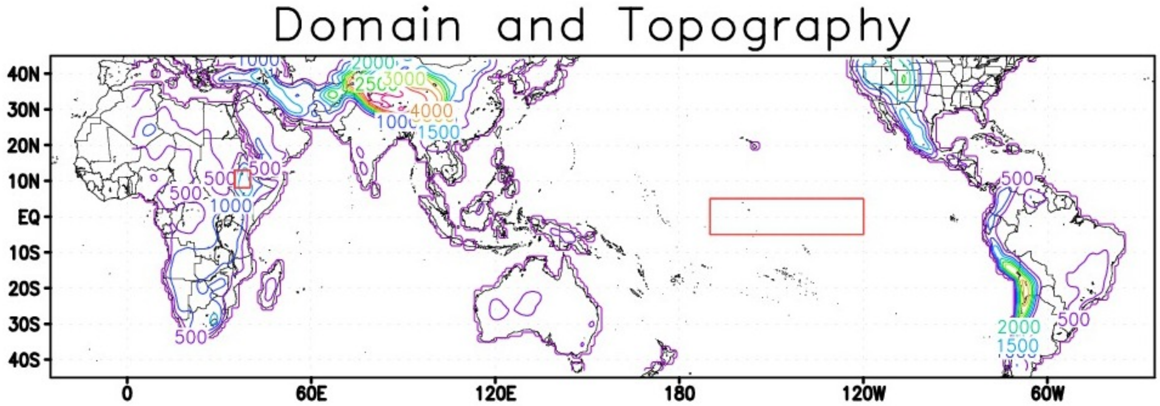

Figure 5-7: The domain and the topography of the model. The red box in the Pacific Ocean illustrated Nino 3.4 region, and the red box in Ethiopian Highland illustrated the upper catchment of the Blue Nile.

In this analysis we assess if the model (RegCM4.1) was able to capture the difference between La Niña and El Niño years. The 9 members were averaged for 28 years (1982-2009), and then 5 La Niña years and 5 El Niño years were selected. In the upper panel of Figure 5-8, the average of 5 La Niña years (1988, 1998, 1999, 2007 and 2008) are shown, and in the middle panel the average of 5 El Niño years (1982, 1983, 1987, 1992 and 2002). The lower panel shows the difference between La Niña years and El Niño years, with rainfall differences in the Sahel region and in the upper catchment of the Blue Nile. The results of each ensemble member were calculated for each member (Figure 5-9 to Figure 5-17), there was a remarkable variability between different members. These model results agree with the previous analysis, confirming that La Niña years are associated with the above normal rainfall and El Niño years with below normal rainfall in the upper catchment of the Blue Nile. So, the model can capture the impact of El Niño/ La Niña.

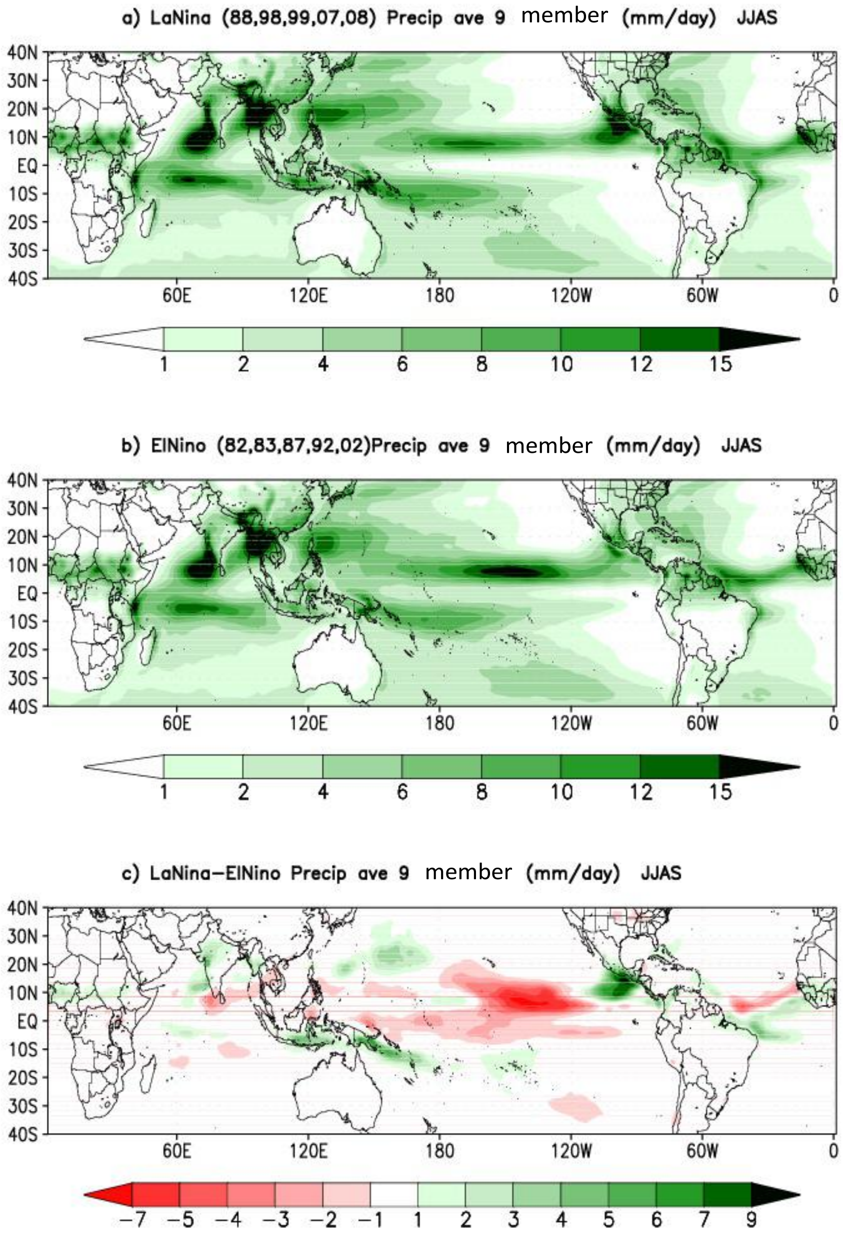

a) LaNina (88,98,99,07,08) Precip ave 9 member (mm/day) JJAS

b) ElNino (82,83,87,92,02)Precip ave 9 member (mm/day) JJAS

c) LaNina–ElNino Precip ave 9 member (mm/day) JJAS

Figure 5-8: The rainfall from 9 members during JJAS for a) 5 La Niña years b) 5 El Niño years c) The difference between La Niña years and El Niño years.

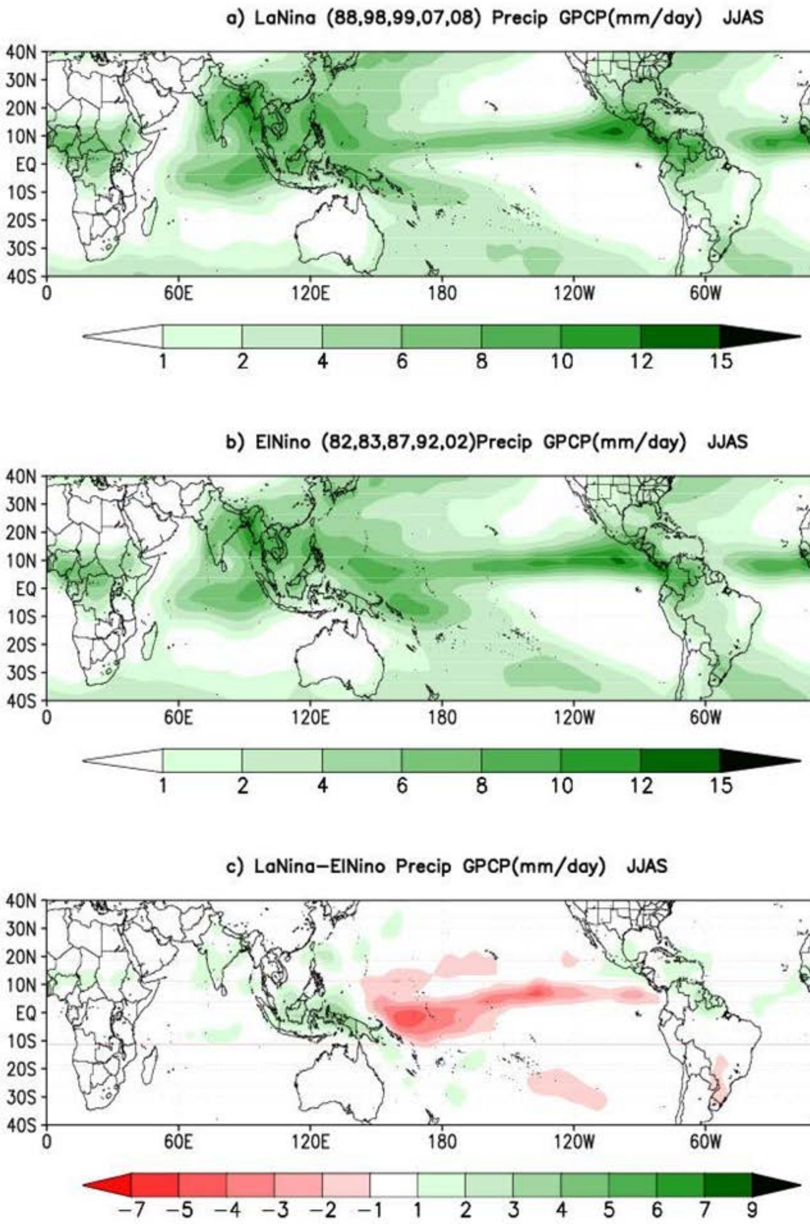

Figure 5-9: The rainfall for member 1 during JJAS for a) 5 La Nina years b) 5 El Nino years c) The difference between La Nina years and El Nino years.

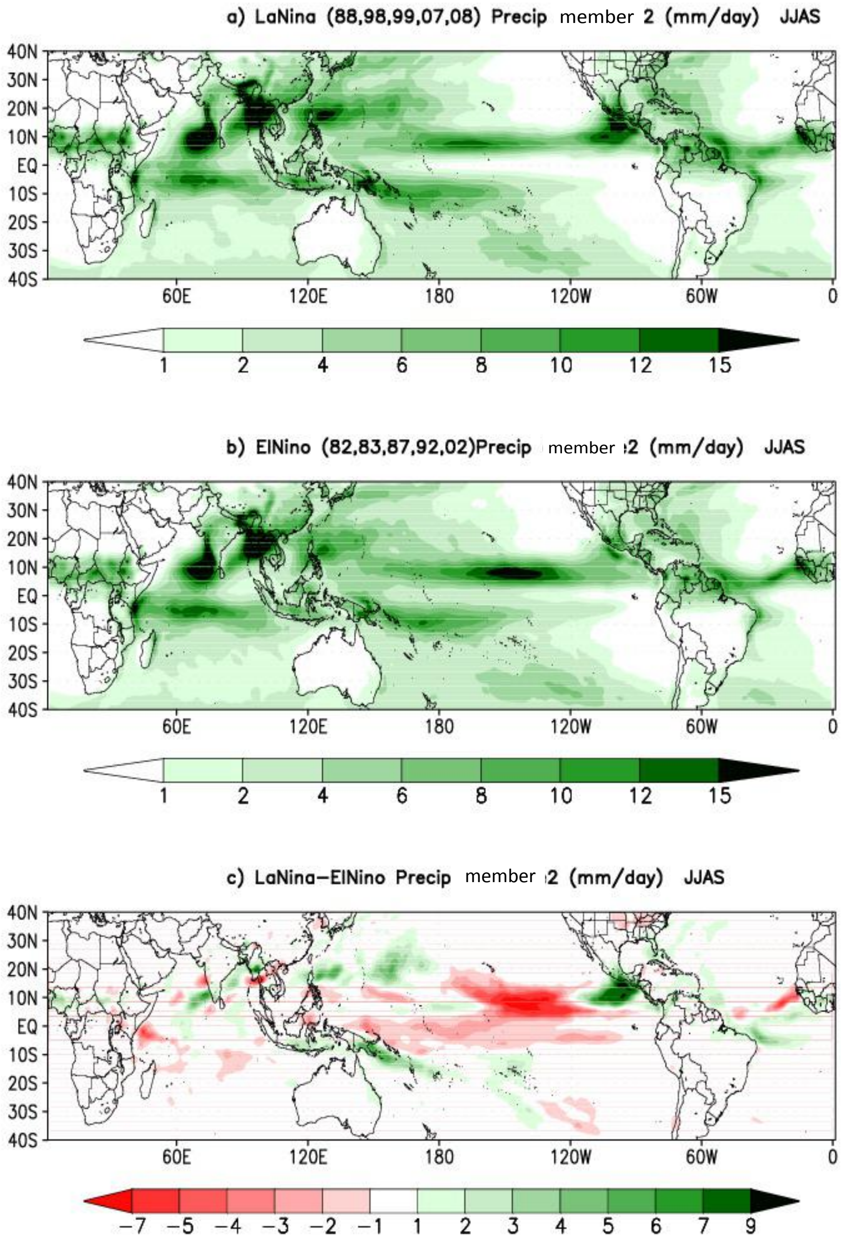

Figure 5-10: The rainfall for member 2 during JJAS for a) 5 La Nina years b) 5 El Nino years c) The difference between La Nina years and El Nino years.

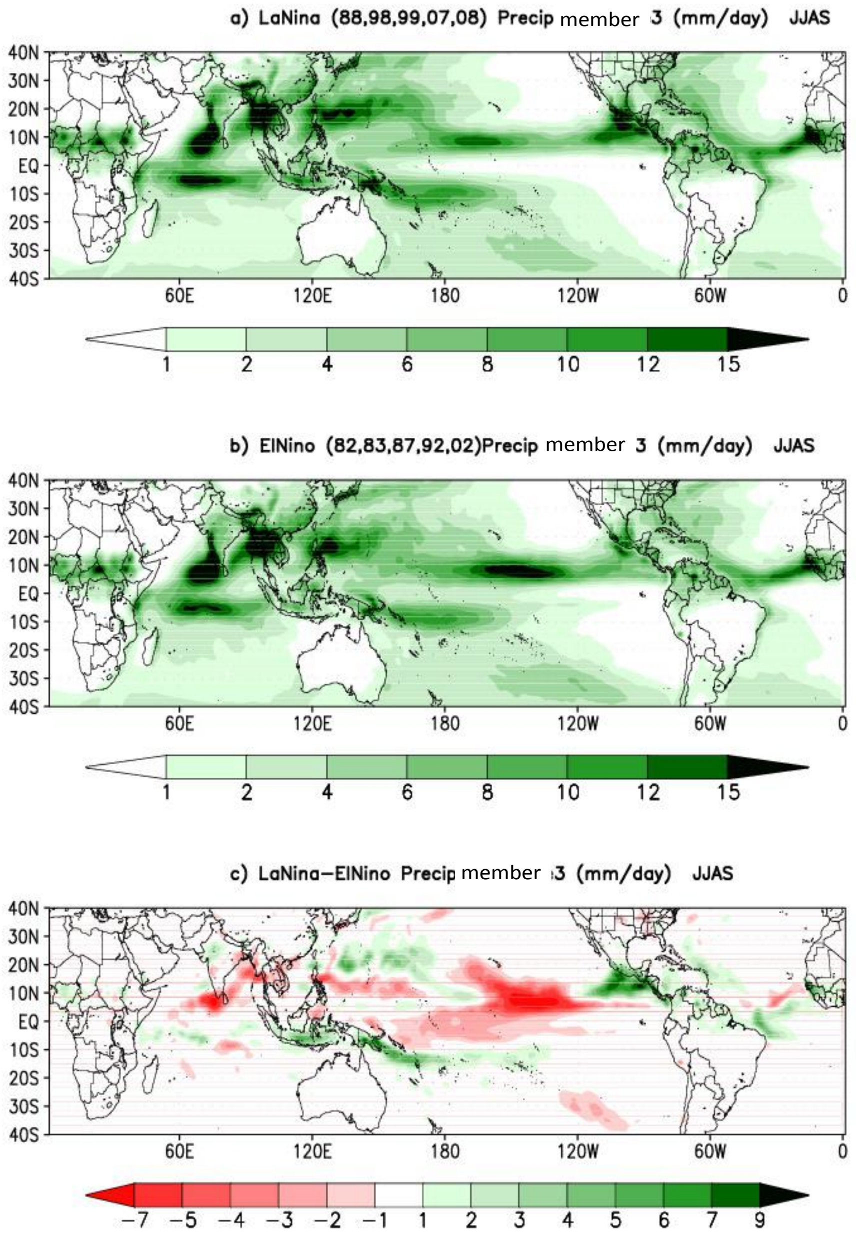

Figure 5-11: The rainfall for member 3 during JJAS for a) 5 La Nina years b) 5 El Nino years c) The difference between La Nina years and El Nino years.

a) LaNina (88,9 member) Precip ensemble4 (mm/day) JJAS

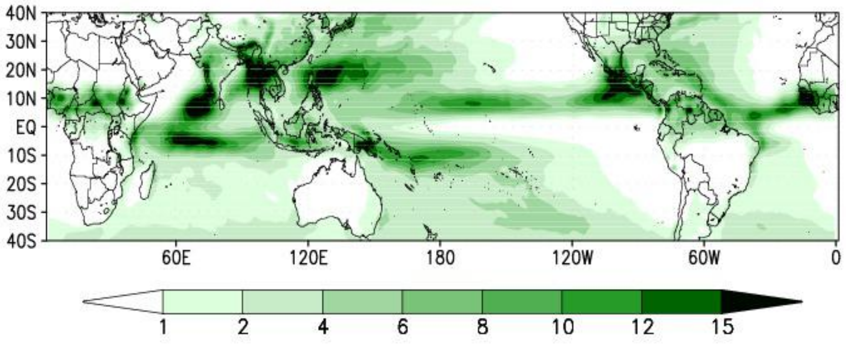

b) ElNino (82, member 2)Precip ensemble4 (mm/day) JJAS

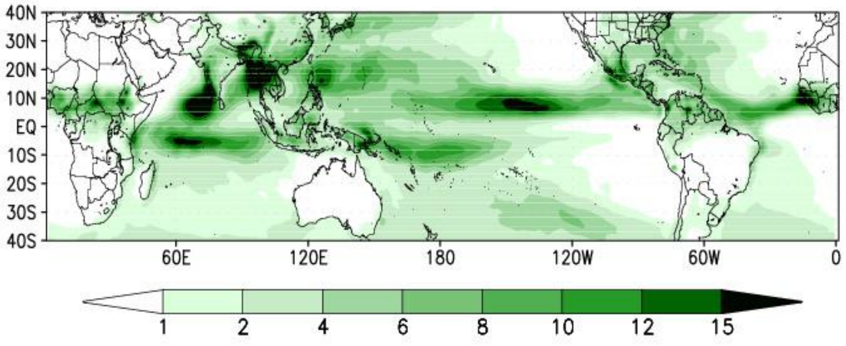

c) La member Precip ensemble4 (mm/day) JJAS

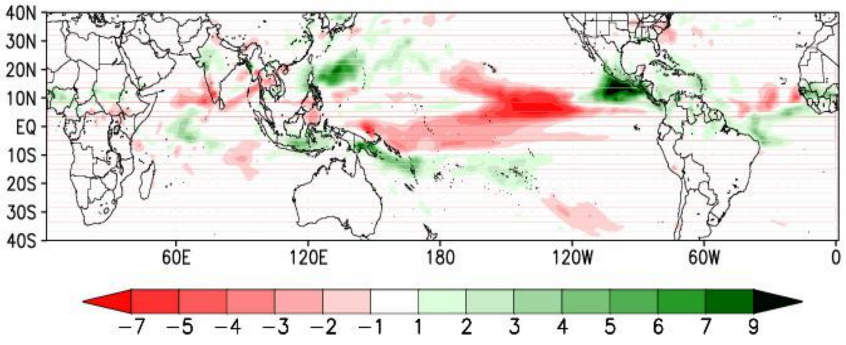

Figure 5-12: The rainfall for member 4 during JJAS for a) 5 La Nina years b) 5 El Nino years c) The difference between La Nina years and El Nino years.

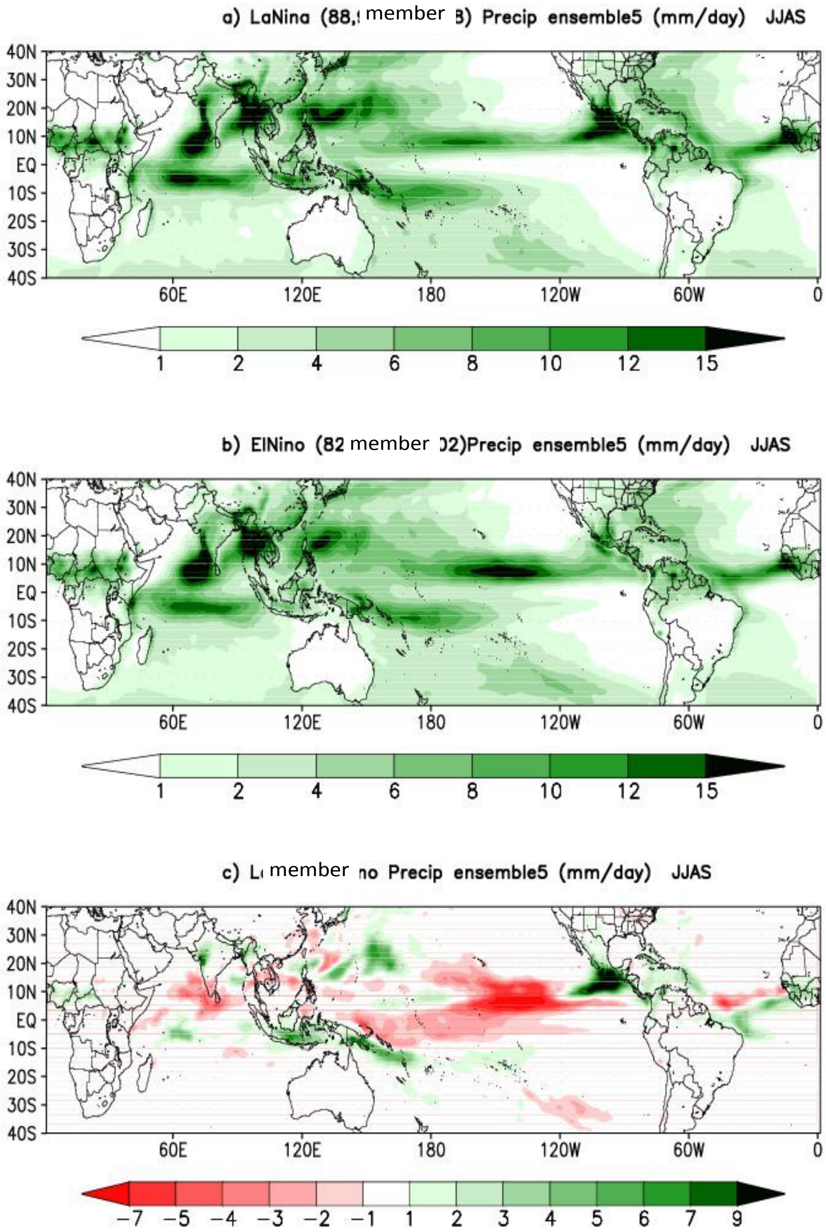

Figure 5-13: The rainfall for member 5 during JJAS for a) 5 La Nina years b) 5 El Nino years c) The difference between La Nina years and El Nino years.

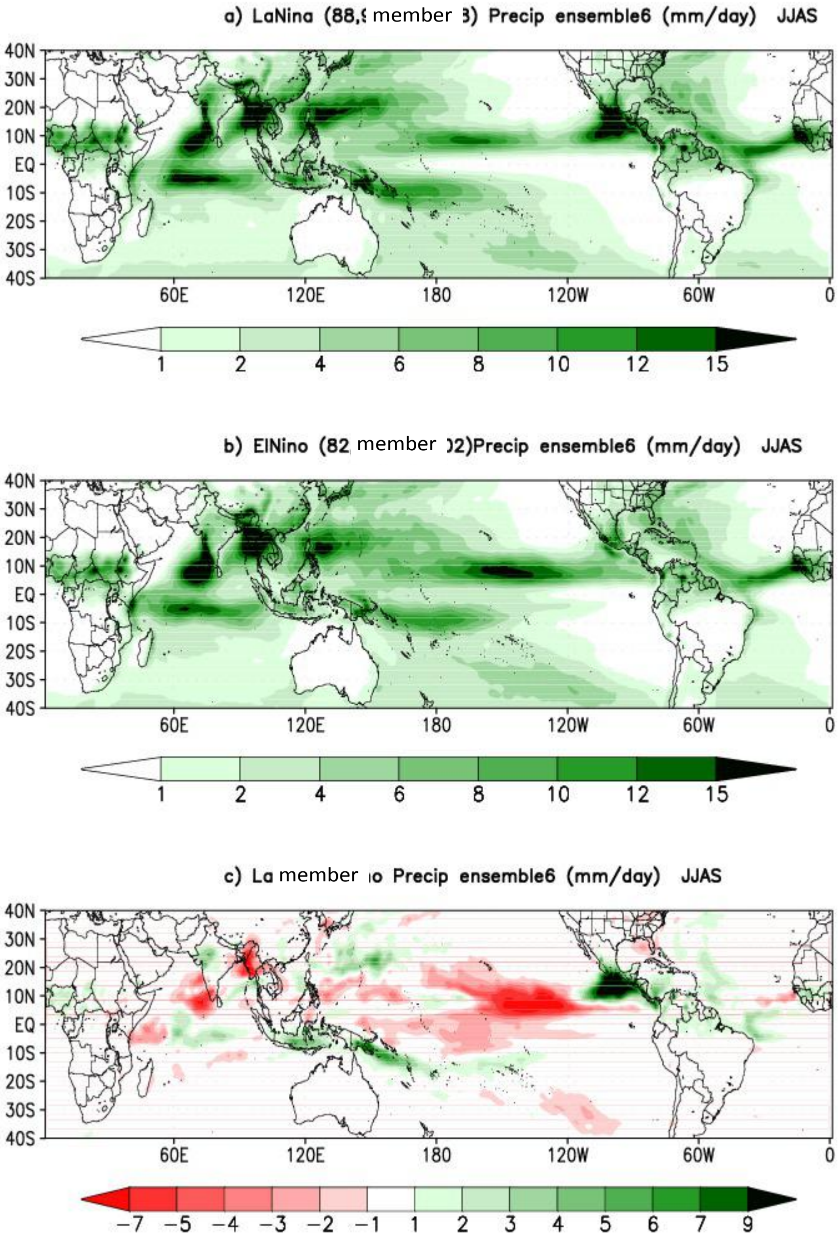

Figure 5-14: The rainfall for member 6 during JJAS for a) 5 La Nina years b) 5 El Nino years c) The difference between La Nina years and El Nino years.

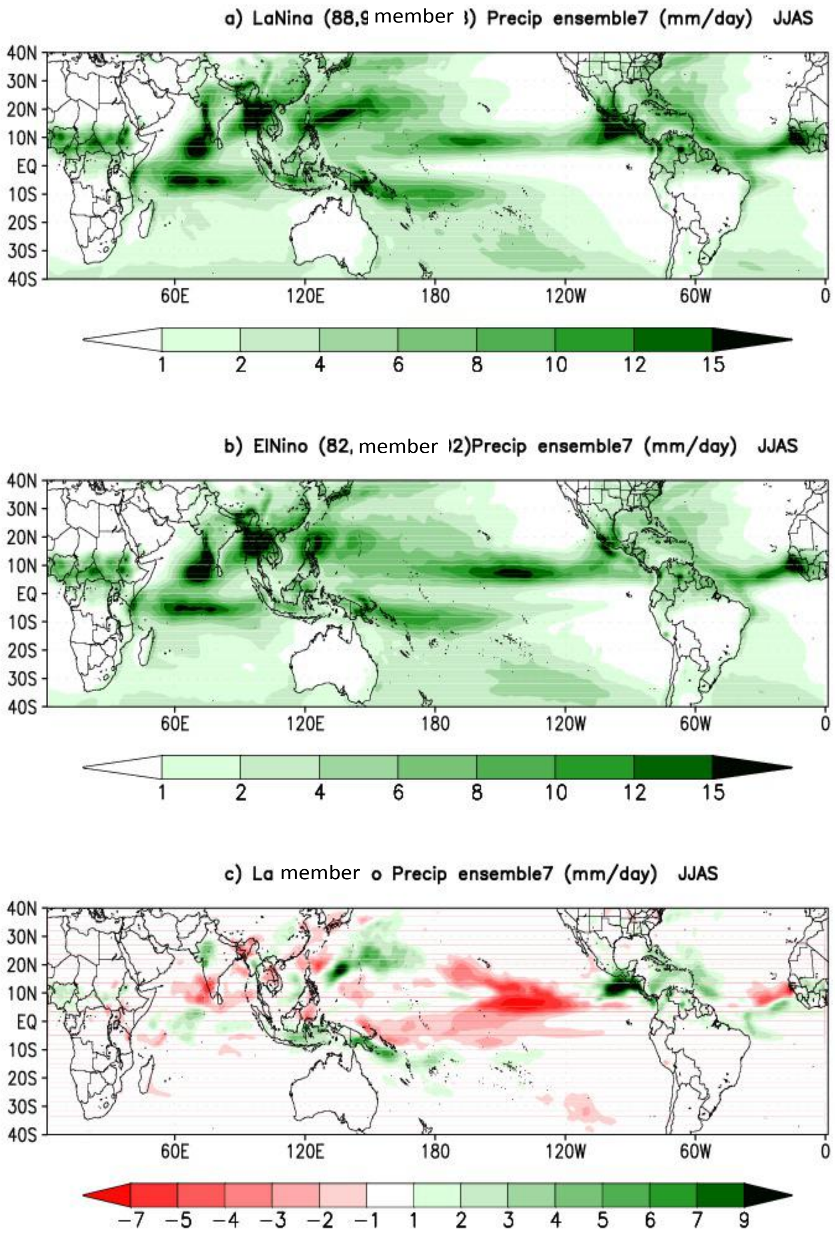

Figure 5-15: The rainfall for member 7 during JJAS for a) 5 La Nina years b) 5 El Nino years c) The difference between La Nina years and El Nino years.

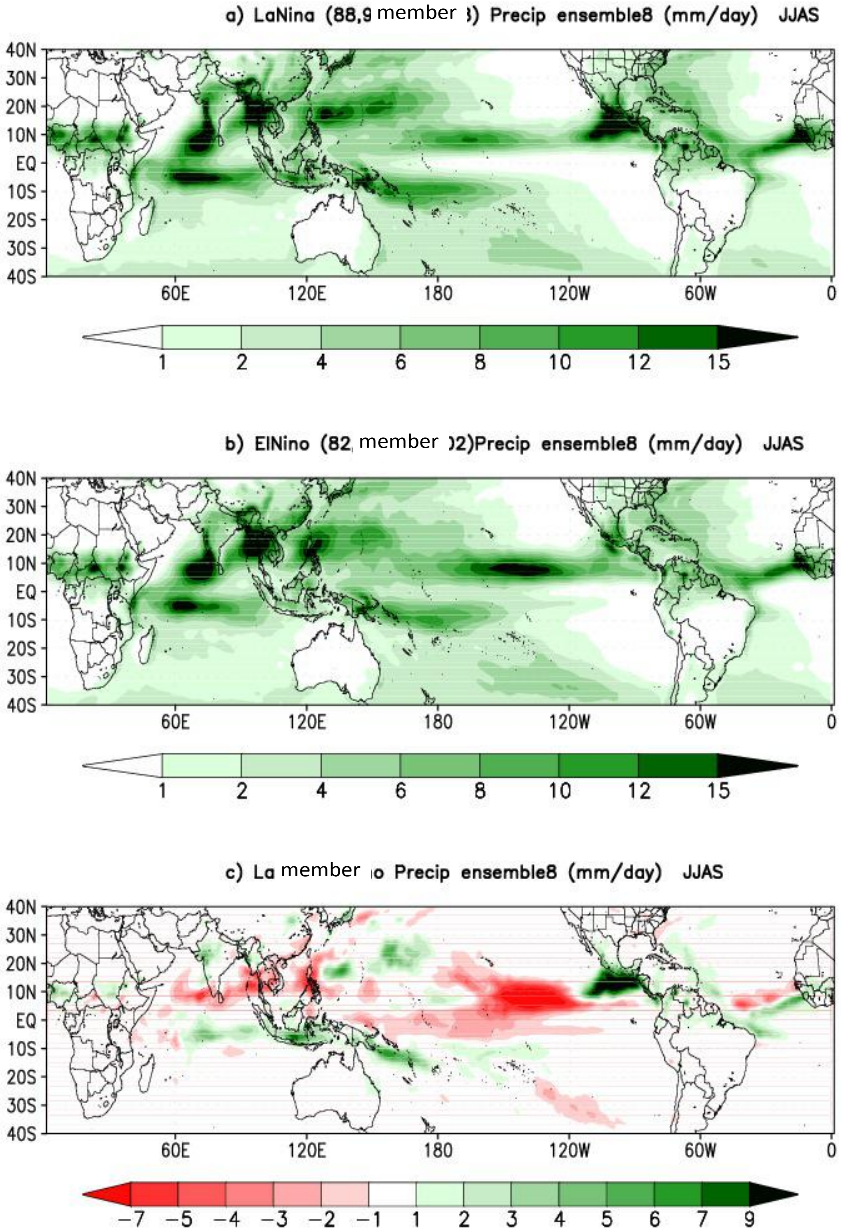
a) LaNina (88,9 member 3) Precip ensemble8 (mm/day) JJAS

b) ElNino (82 member)2)Precip ensemble8 (mm/day) JJAS

c) La member o Precip ensemble8 (mm/day) JJAS

Figure 5-16: The rainfall for member 8 during JJAS for a) 5 La Nina years b) 5 El Nino years c) The difference between La Nina years and El Nino years.

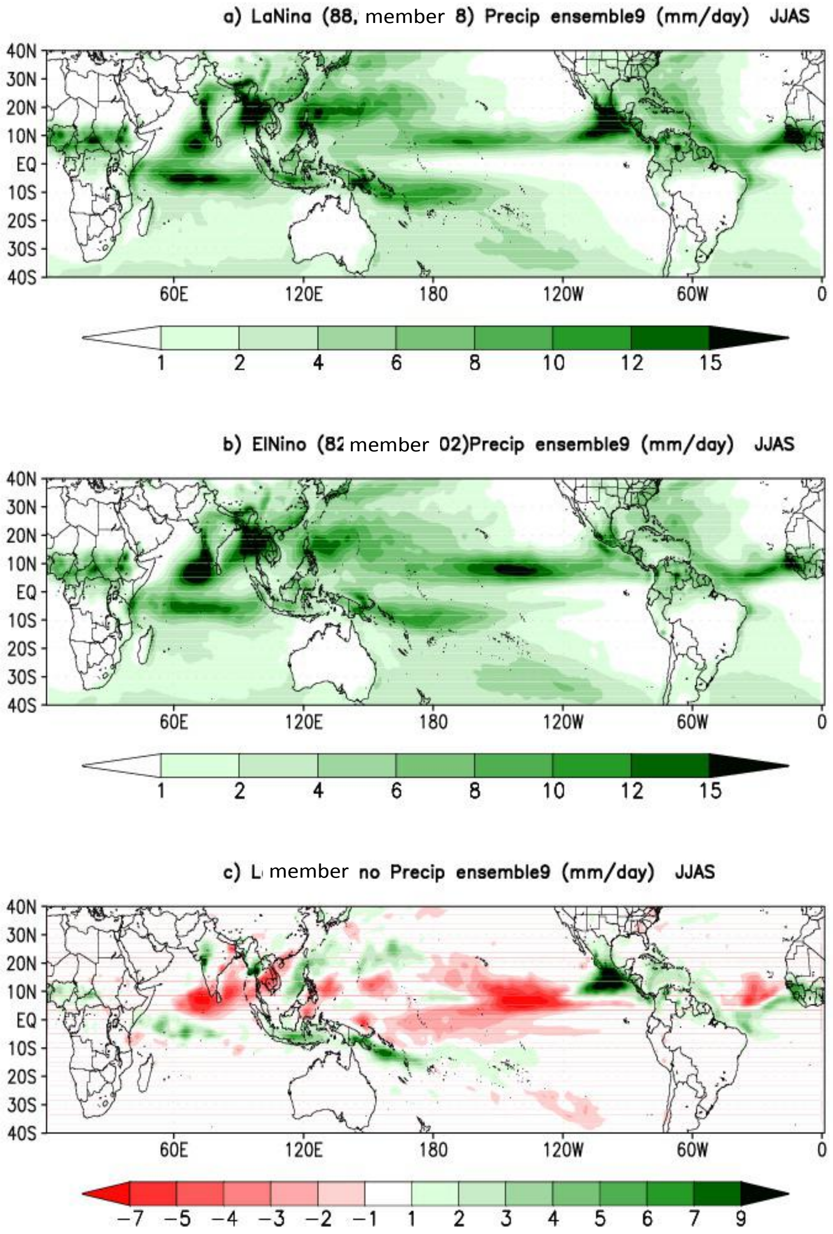

Figure 5-17: The rainfall for member 9 during JJAS for a) 5 La Nina years b) 5 El Nino years c) The difference between La Nina years and El Nino years.

Figure 5-18 shows the same analysis in Figure 5-8. It shows a magnified picture for North Africa for 5 La Niña years minus 5 El Niño years. The model managed to capture very well the difference in rainfall along the ITCZ. The Sahel region is the most affected region by El Niño and La Niña.

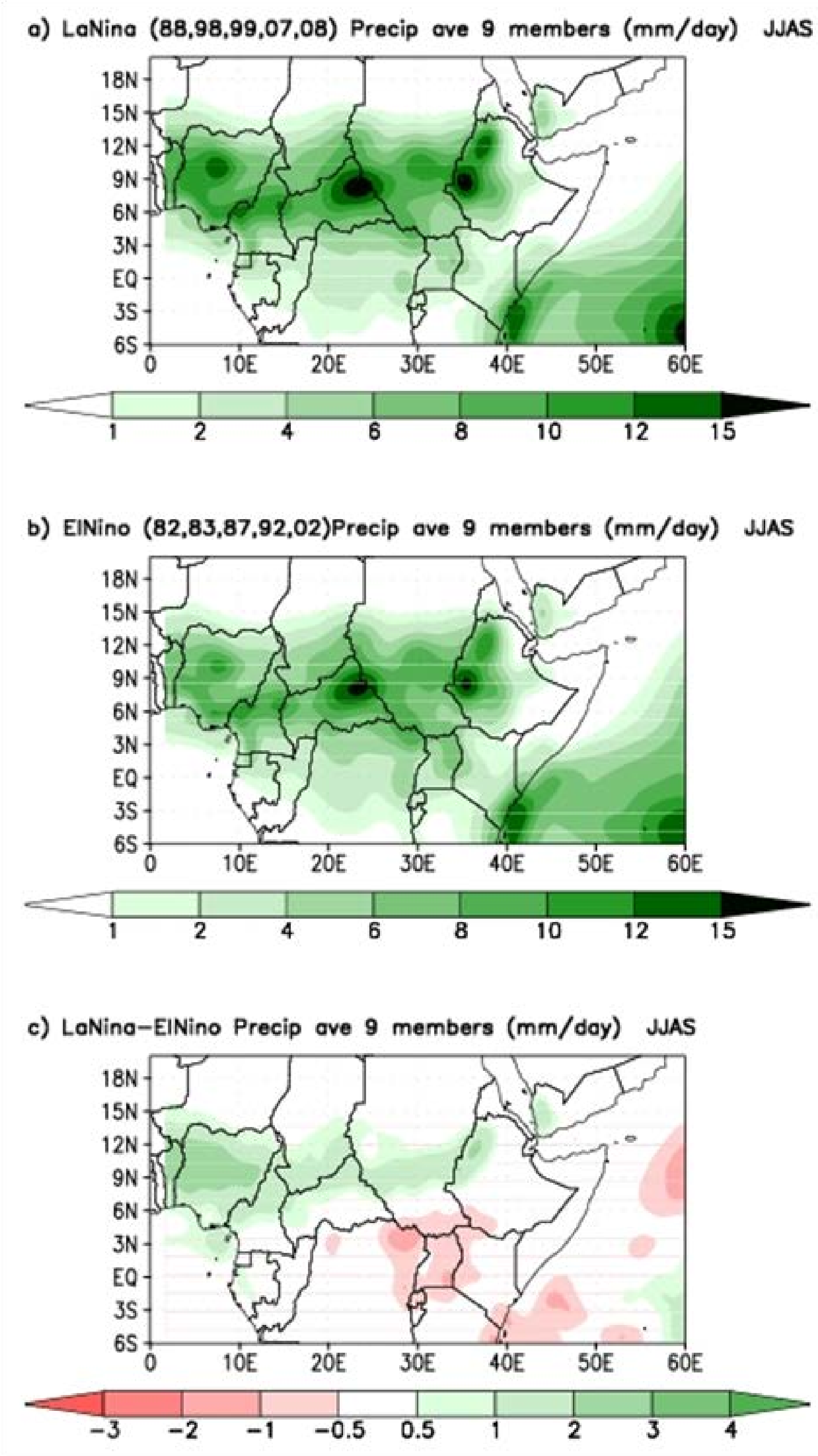

Figure 5-18: The rainfall in North Africa from 9 members during JJAS for a) 5 La Niña years b) 5 El Niño years c) The difference between La Niña years and El Niño years.

In Figure 5-19 an assessment was made also for the observational dataset from GPCP to see if it also captures the difference between La Niña and El Niño years. The GPCP data was averaged also for 28 years (1982-2009), and then 5 La Niña years and 5 El Niño years were selected. In the upper panel of Figure 5-19, the average of 5 La Niña years (1988, 1998, 1999, 2007 and 2008) are shown, and in the middle panel the average of 5 El Niño years (1982, 1983, 1987, 1992 and 2002). The lower panel shows the difference between La Niña years and El Niño years, with rainfall differences exhibited in the Sahel region and in the upper catchment of the Blue Nile.

a) LaNina (88,98,99,07,08) Precip GPCP(mm/day) JJAS

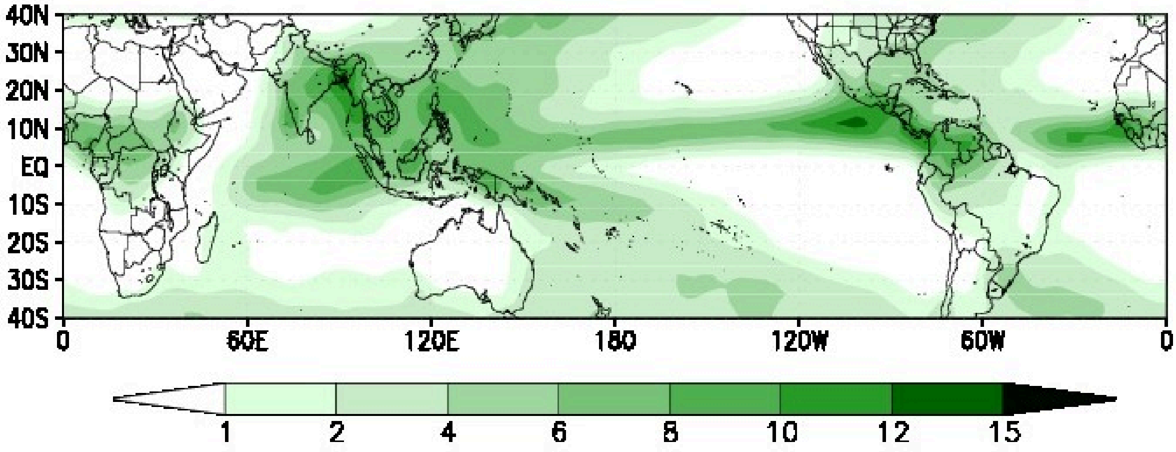

b) ElNino (82,83,87,92,02)Precip GPCP(mm/day) JJAS

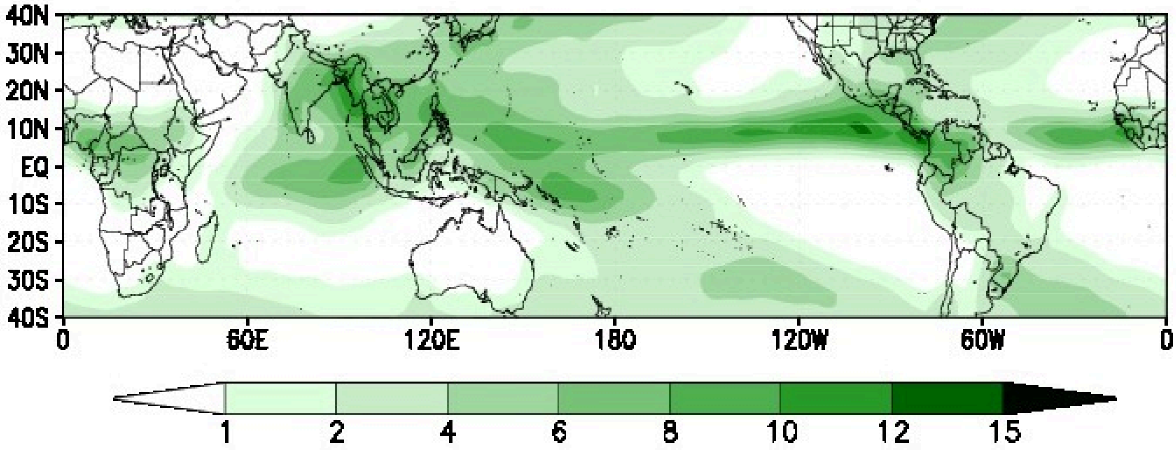

c) LaNina−ElNino Precip GPCP(mm/day) JJAS

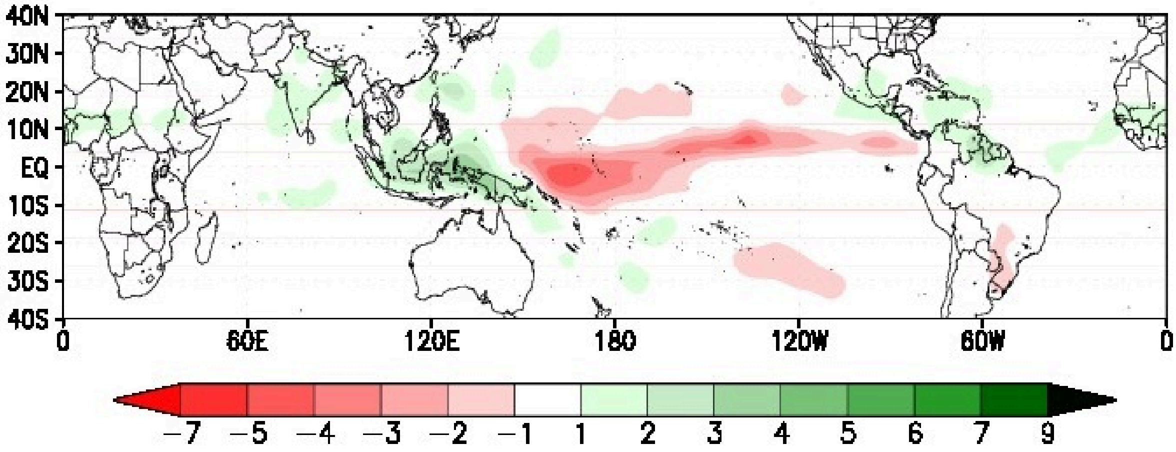

Figure 5-19: The rainfall from GPCP during JJAS for a) 5 La Niña years b) 5 El Niño years c) The difference between La Niña years and El Niño years.

The North African region is shown also in Figure 5-20. La Nina years were shown in the upper panel while El Nino years were shown in the middle panel. The lower panel showed the differences between La Nina years and El Nino years. The observational difference from GPCP extends further north up 18° N, unlike the model difference (Figure 5-18) which extends up to 15° N.

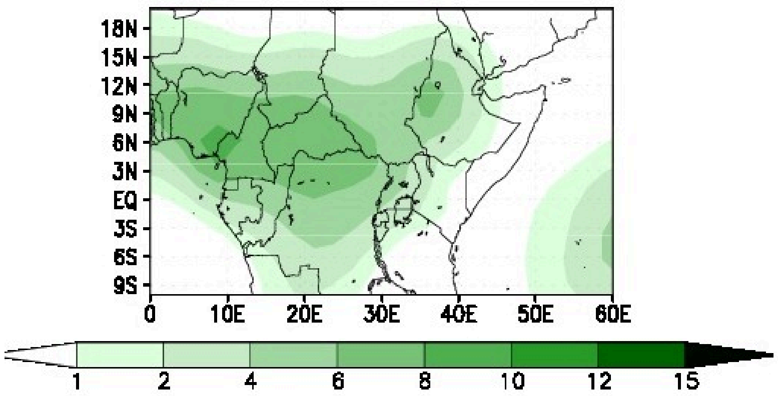
a) LaNina (88,98,99,07,08) Precip GPCP(mm/day) JJAS

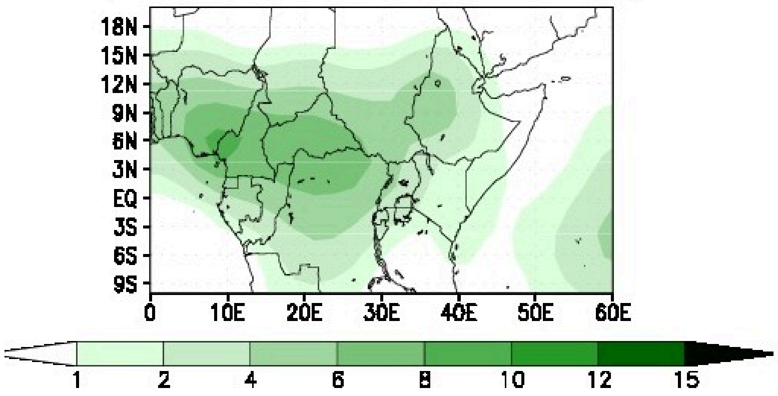
b) ElNino (82,83,87,92,02)Precip GPCP(mm/day) JJAS

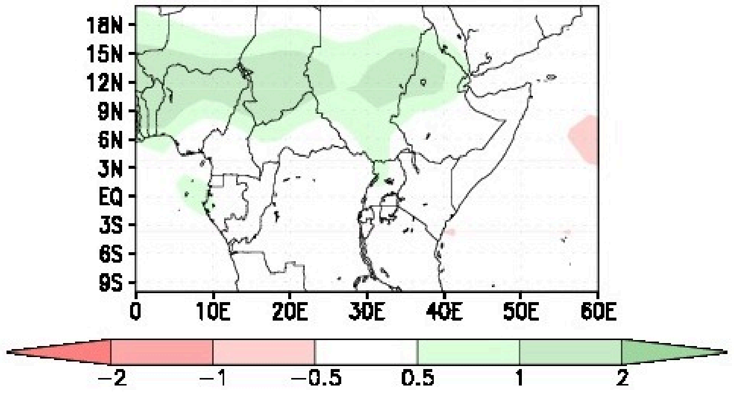
c) LaNina–ElNino Precip GPCP(mm/day) JJAS

Figure 5-20: The rainfall in North Africa from GPCP during JJAS for a) 5 La Niña years b) 5 El Niño years c) The difference between La Niña years and El Niño years.

5.4.2 Correlation between rainfall anomalies over Ethiopian Highlands and SST anomalies over the Pacific Ocean in Nino 3.4 region for 9 members

Figure 5-21 shows the correlation between the rainfall anomalies during JJAS and the SST anomalies during (JFM, FMA, MAM, AMJ, MJJ and JJA). The correlations are negative during all seasons. The lowest correlation was around 42 % in JFM and it increased gradually up to AMJ. The highest correlation was around 62% during AMJ. After that, the correlations decreased to 49% in JJA. In section 3.2 the river discharge showed the highest probability for drought events during AMJ (83 %). The model results also show the highest correlation during AMJ. These results support the use Nino3.4 in AMJ for a seasonal forecasting of drought in the upper catchment of the Blue Nile.

The previous correlations were calculated for each member (Figure 5-22 to Figure 5-30). The best correlation was found when taking the ensemble mean.

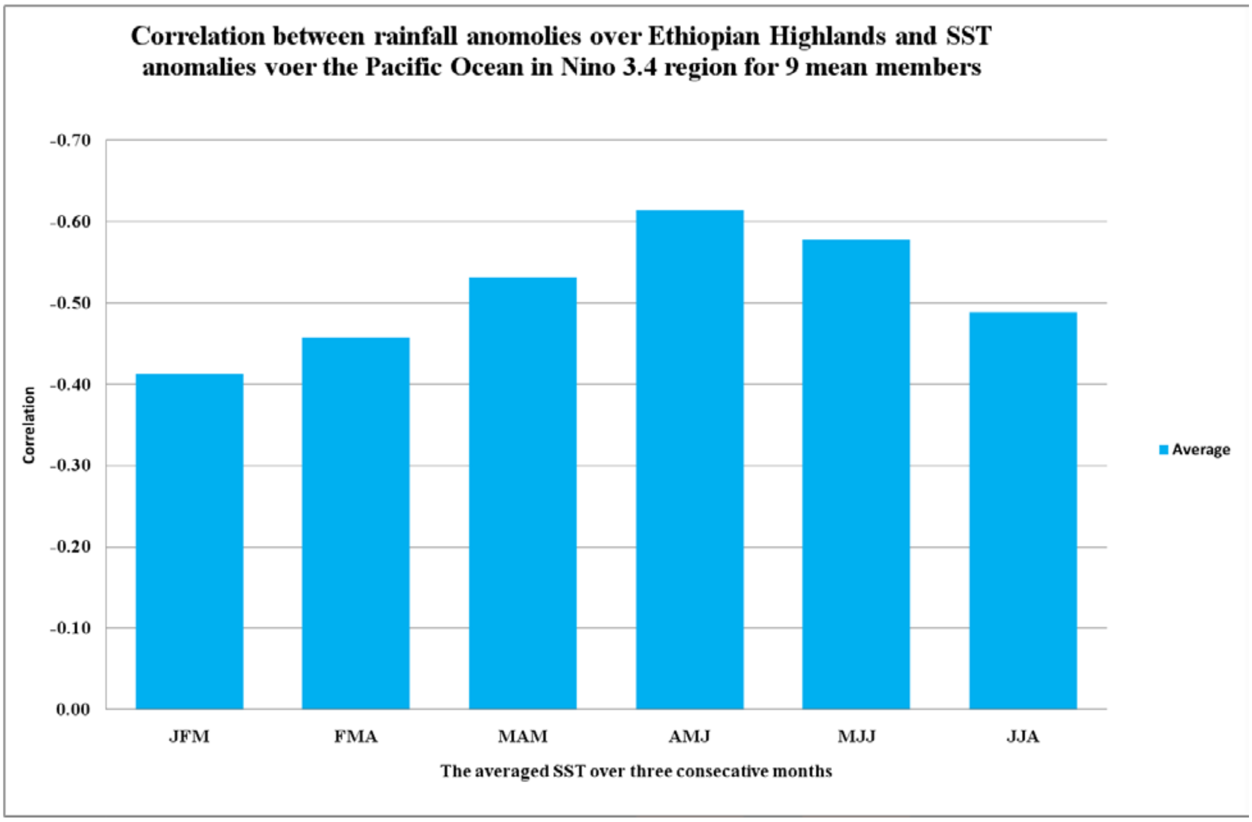

Figure 5-21: The correlation between rainfall anomalies over Ethiopian Highlands for 9 averaged members and SST anomalies over the Pacific Ocean in Nino 3.4 region.

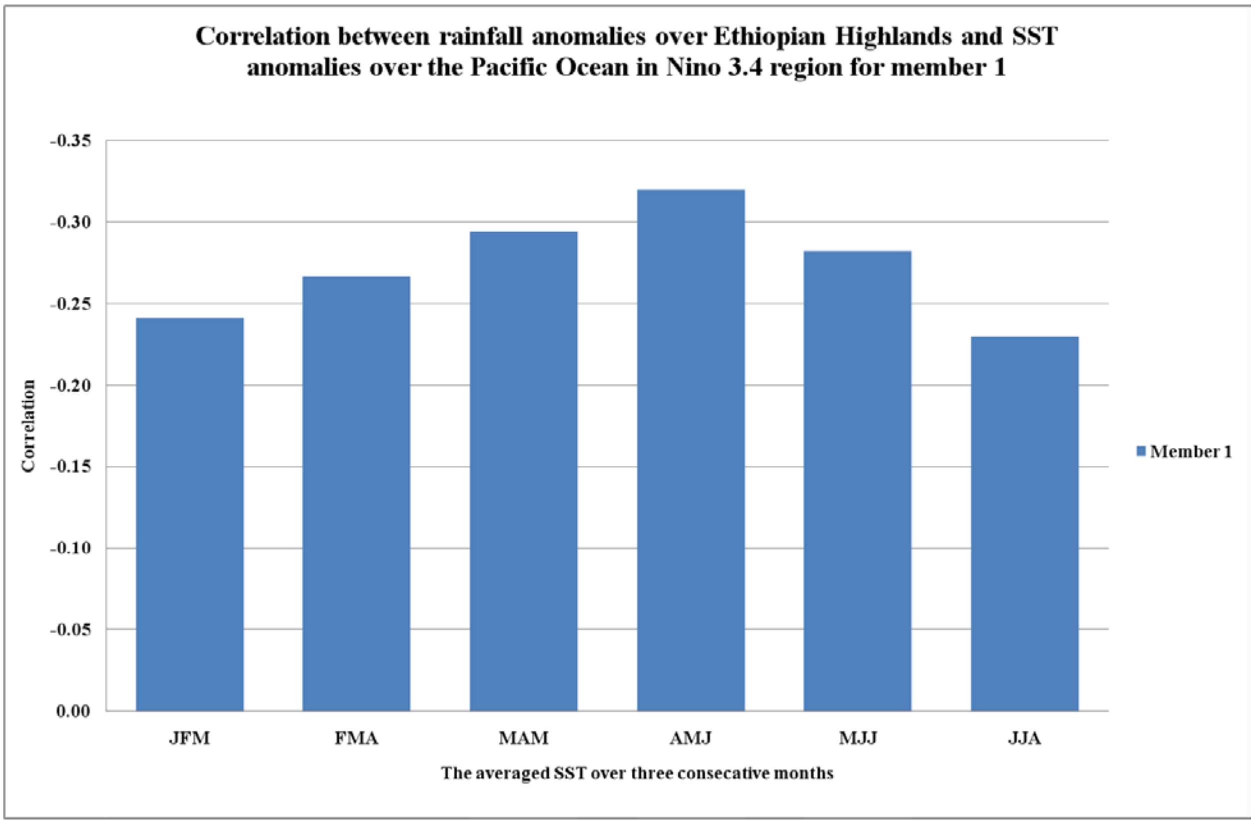

Figure 5-22: The correlation for member 1 between rainfall anomalies over Ethiopian Highlands for 9 averaged members and SST anomalies over the Pacific Ocean in Nino 3.4 region.

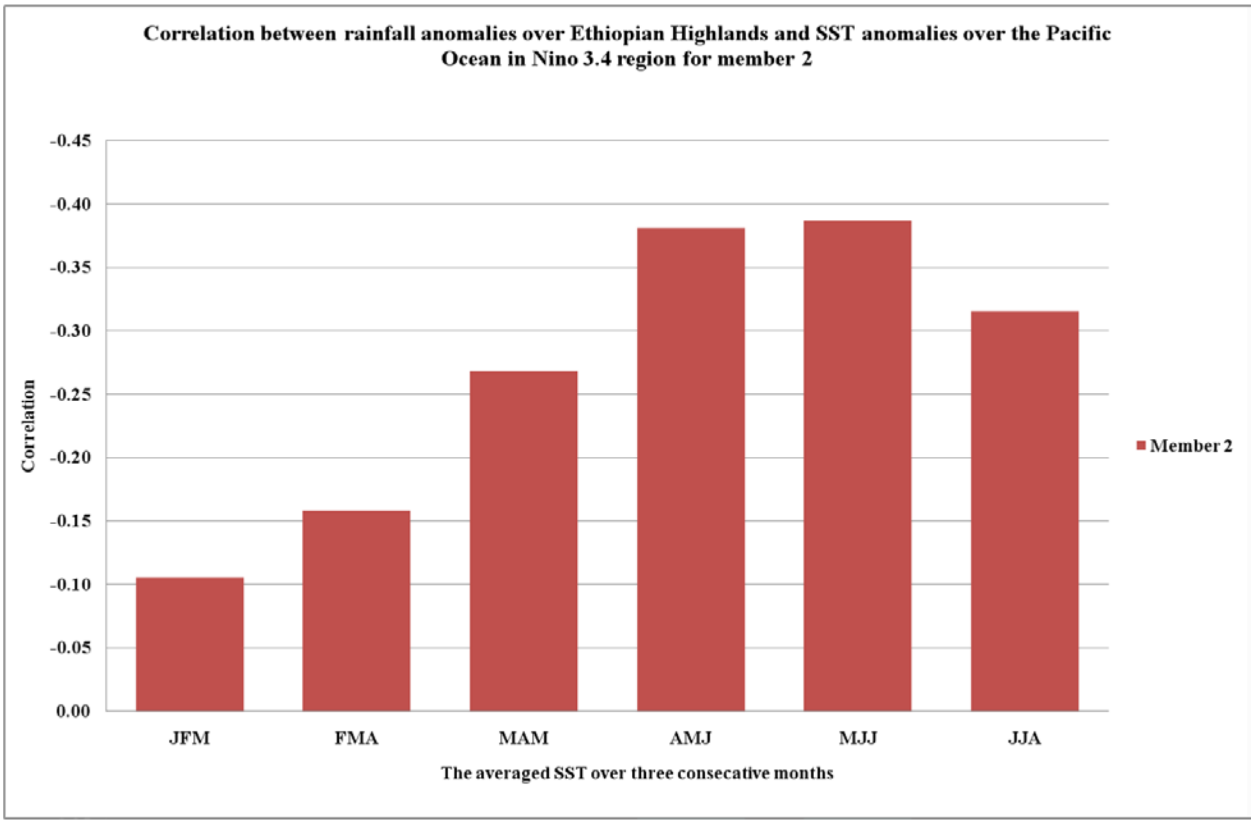

Figure 5-23: The correlation for member 2 between rainfall anomalies over Ethiopian Highlands for 9 averaged members and SST anomalies over the Pacific Ocean in Nino 3.4 region.

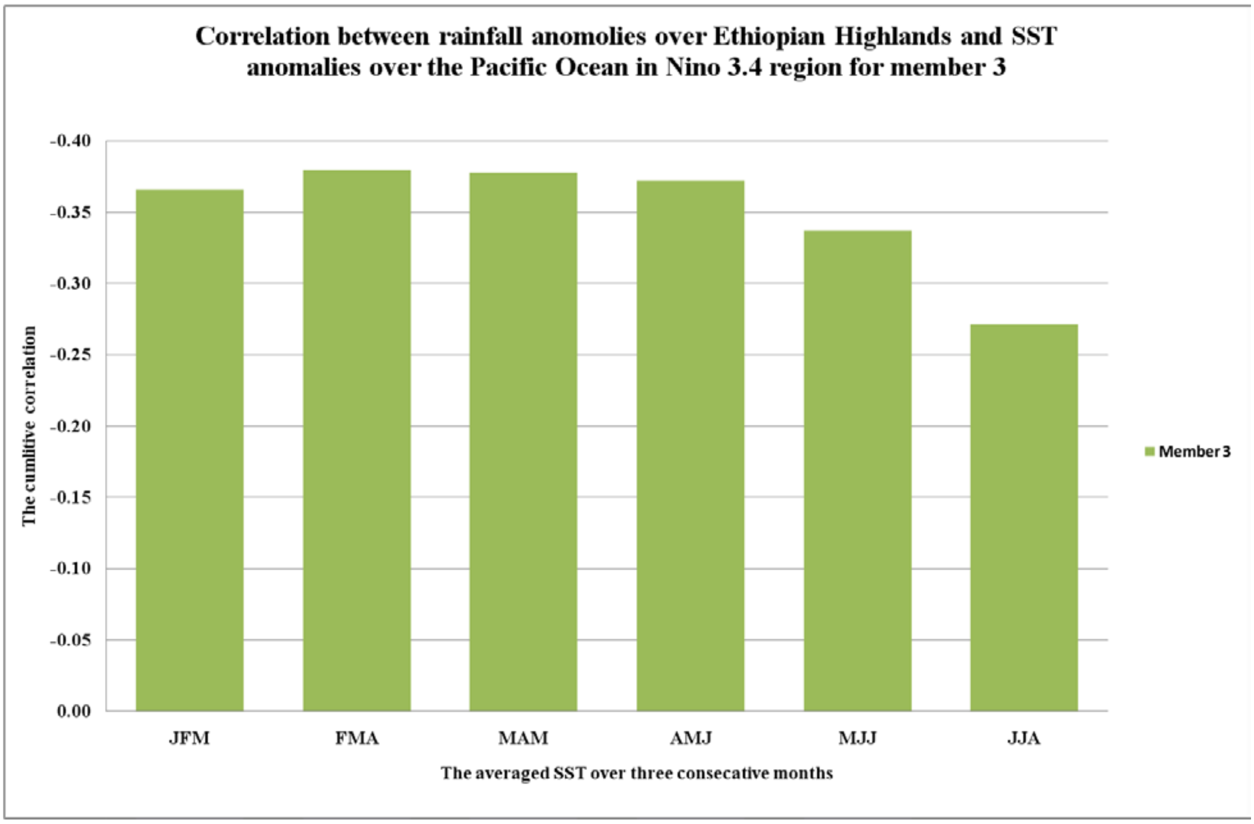

Figure 5-24: The correlation for member 3 between rainfall anomalies over Ethiopian Highlands for 9 averaged members and SST anomalies over the Pacific Ocean in Nino 3.4 region.

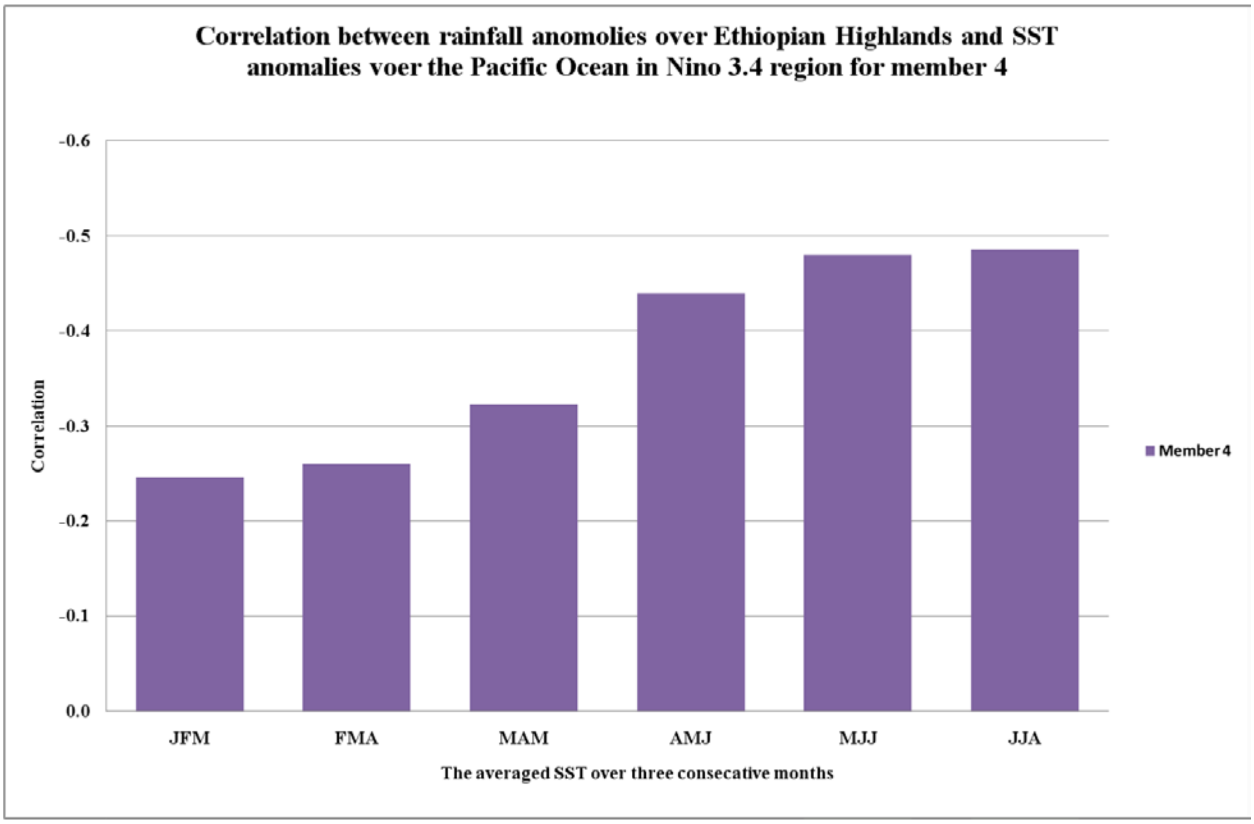

Figure 5-25: The correlation for member 4 between rainfall anomalies over Ethiopian Highlands for 9 averaged members and SST anomalies over the Pacific Ocean in Nino 3.4 region.

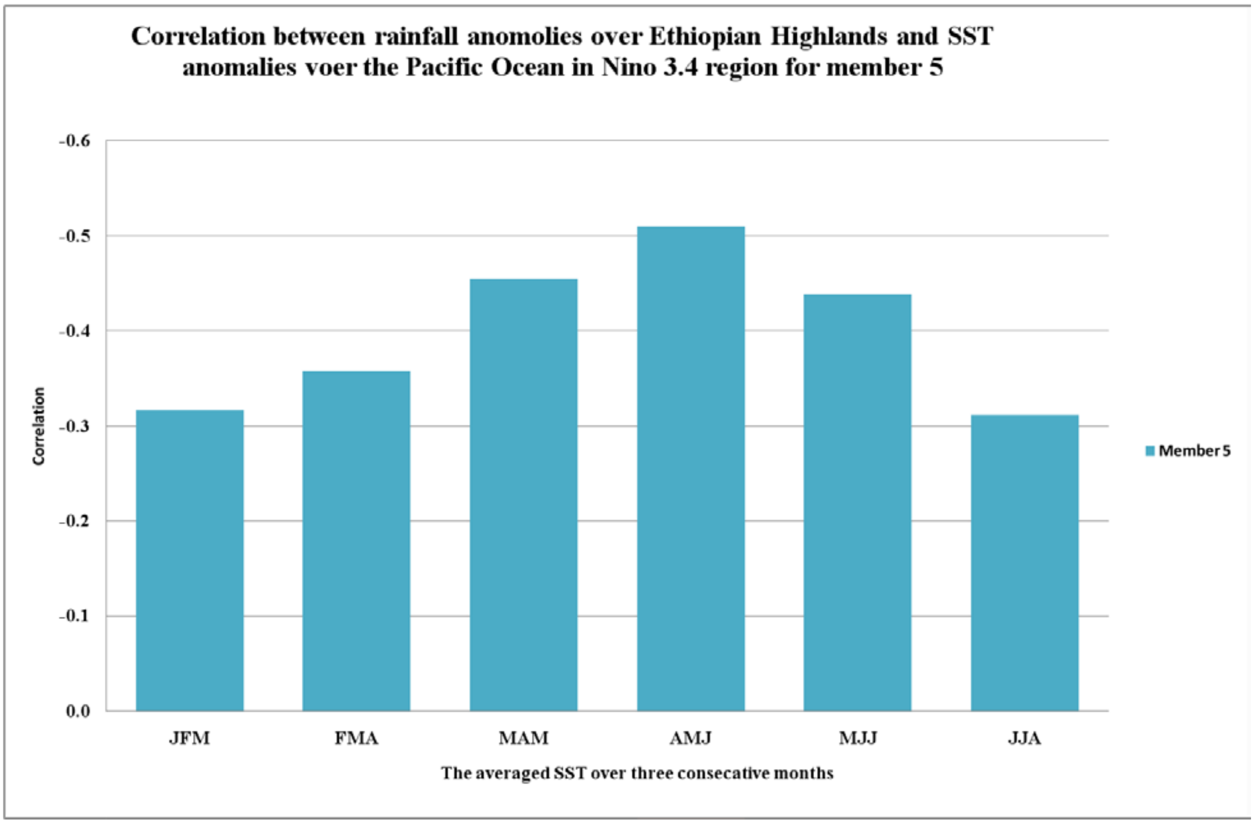

Figure 5-26: The correlation for member 5 between rainfall anomalies over Ethiopian Highlands for 9 averaged members and SST anomalies over the Pacific Ocean in Nino 3.4 region.

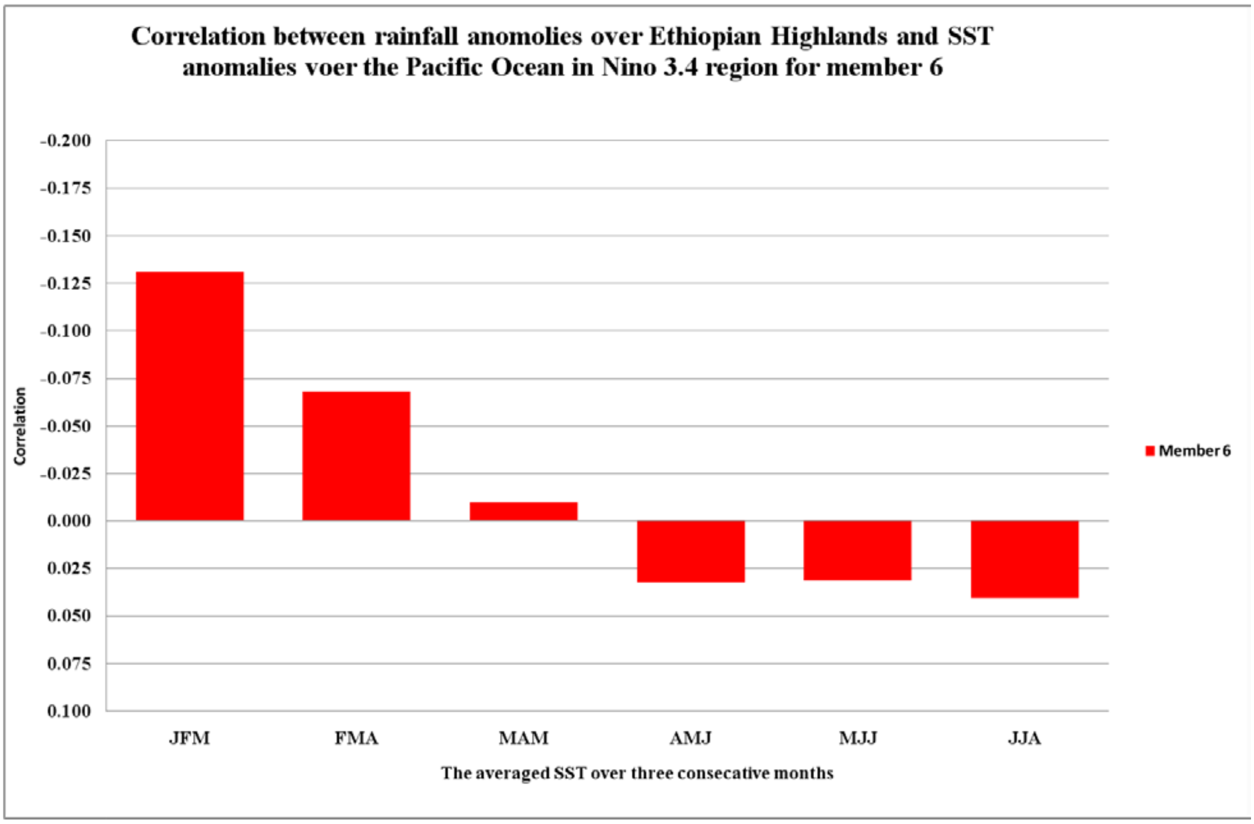

Figure 5-27: The correlation for member 6 between rainfall anomalies over Ethiopian Highlands for 9 averaged members and SST anomalies over the Pacific Ocean in Nino 3.4 region.

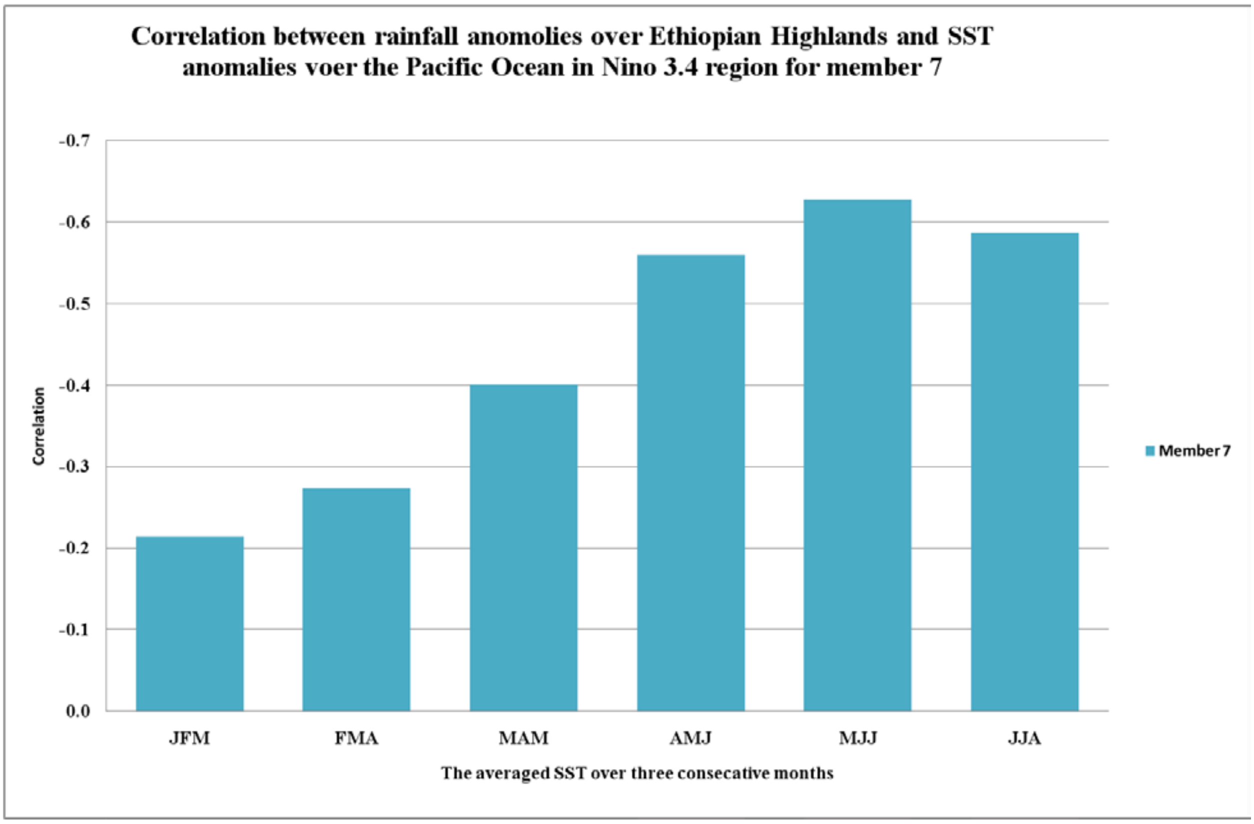

Figure 5-28: The correlation for member 7 between rainfall anomalies over Ethiopian Highlands for 9 averaged members and SST anomalies over the Pacific Ocean in Nino 3.4 region.

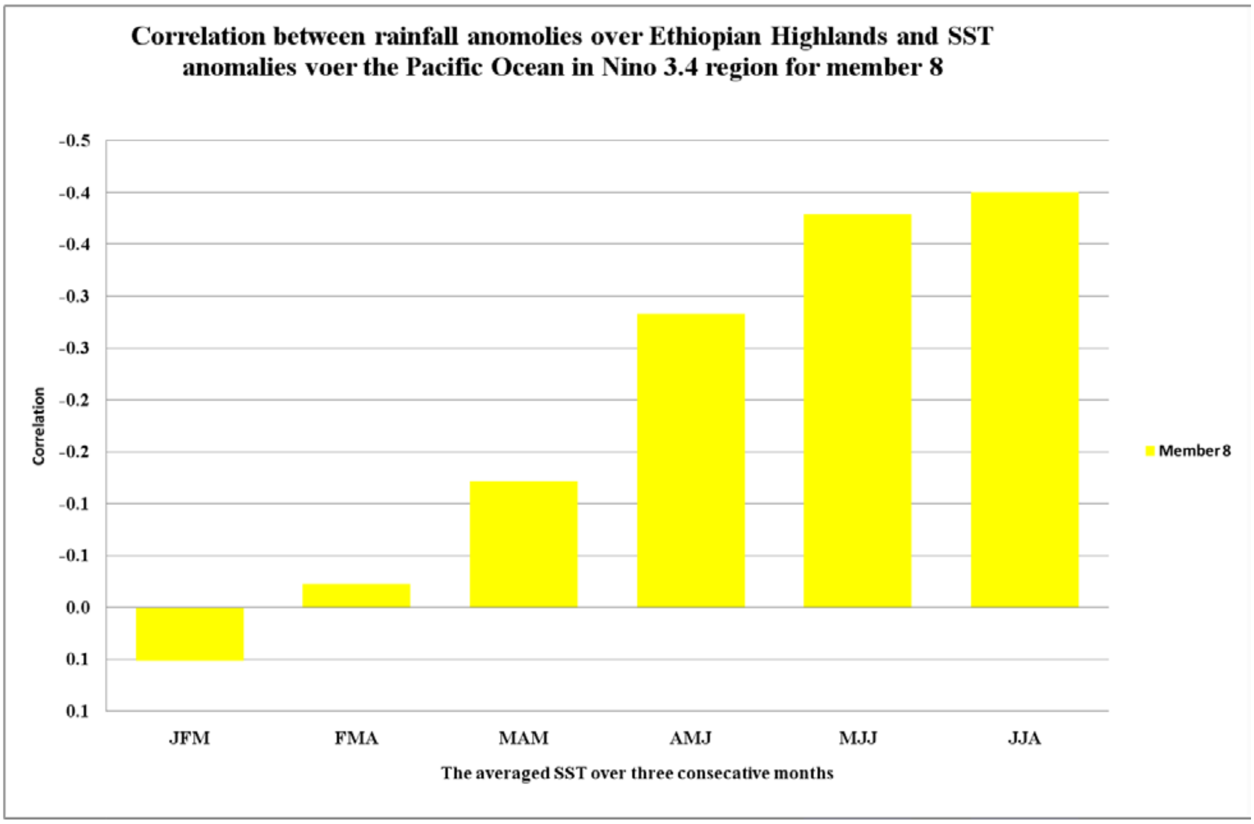

Figure 5-29: The correlation for member 8 between rainfall anomalies over Ethiopian Highlands for 9 averaged members and SST anomalies over the Pacific Ocean in Nino 3.4 region.

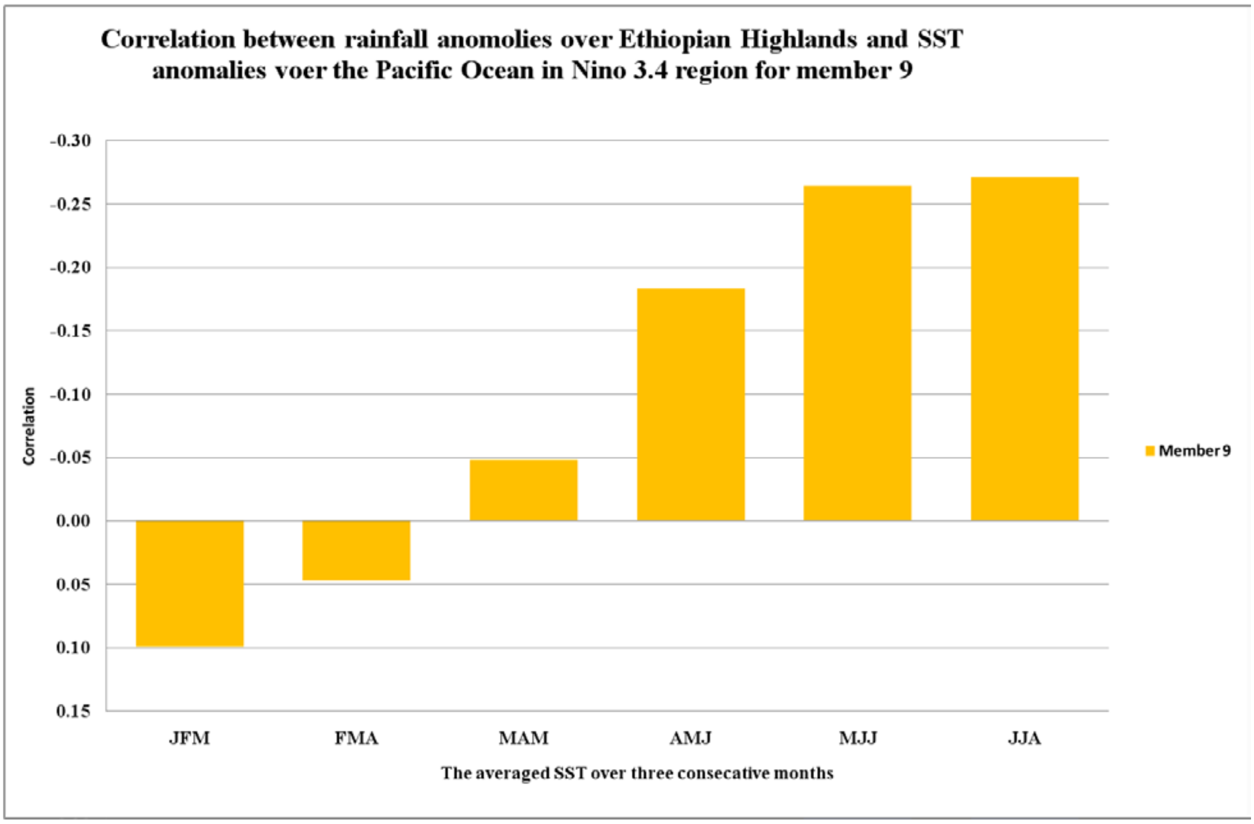

Figure 5-30: The correlation for member 9 between rainfall anomalies over Ethiopian Highlands for 9 averaged members and SST anomalies over the Pacific Ocean in Nino 3.4 region.

The negative correlation between the SST anomalies in Pacific Ocean in Nino 3.4 region and the rainfall in the upper catchment of the Blue Nile during JJAS is apparent in Figure 5-31. The left axis represents the SST anomalies during AMJ, and the right axis the ensemble mean JJAS rainfall anomaly. Similar analyses for each ensemble member were made (not shown).

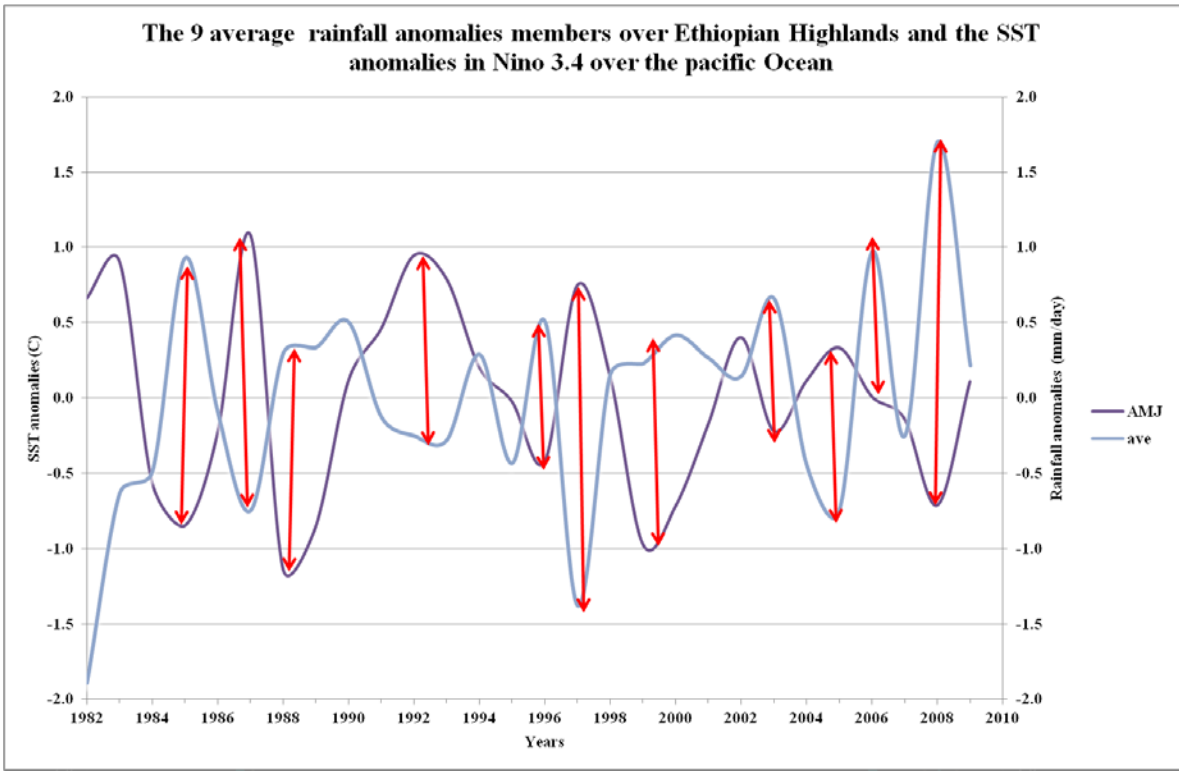

Figure 5-31: The SST anomalies during AMJ in Nino 3.4 region and the rainfall anomalies in the upper catchment of the Blue Nile for 9 averaged members.

5.4.3 Correlation between rainfall anomalies over Ethiopian Highlands and the late season of SST anomalies over the Pacific Ocean in Nino 3.4 region for 9 averaged members

The correlation was calculated also for the late season of SST with the rainfall from 9 averaged members during JJAS as shown in Table 5-1, it reduced gradually. In JAS the correlation was – 0.44, in ASO it was – 0.41, in SON it was – 0.38 and OND it was – 0.347. This result is compatible with the observational data.

Table 5-1: The correlation between the late season of SST anomalies in Nino 3.4 region and the upper catchment of the Blue Nile in Ethiopian Highlands

SST anomalies	Rainfall over Ethiopian Highland from 9 members	Correlation
JAS	JJAS	-0.44
ASO	JJAS	-0.41
SON	JJAS	-0.38
OND	JJAS	-0.347

Regression analysis of DJF and JJA for Nino 3.4 index onto RegCM rainfall for 9 members (1982 -2009)

In this section we present a regression analysis between Nino 3.4, in different seasons (DJF and JJA), and the GPCP and model rainfall. The upper panel of Figure 5-32 represents the regression of DJF Nino 3.4 index onto DJF GPCP rainfall from 1982 to 2009, while the lower panel of Figure 5-32 shows the regression of JJA Nino 3.4 index onto JJA GPCP.

a) Regression of DJF Nino 3.4 index onto DJF GPCP rainfall 1982–2009

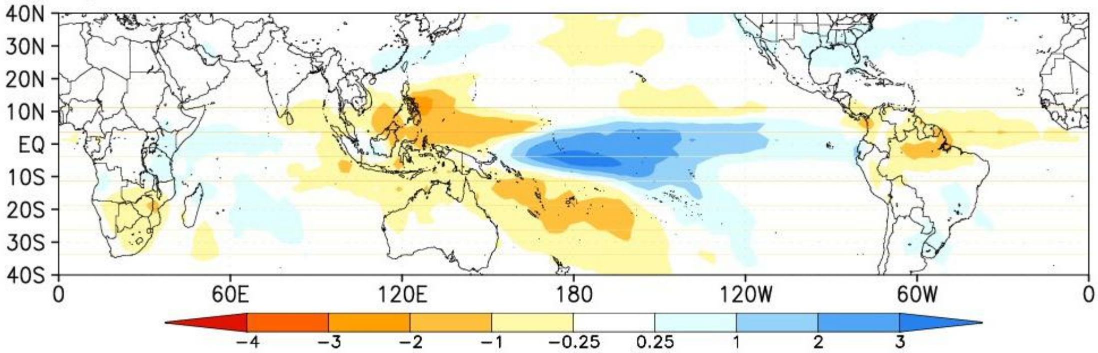

b) Regression of JJA Nino 3.4 index onto JJA GPCP rainfall 1982–2009

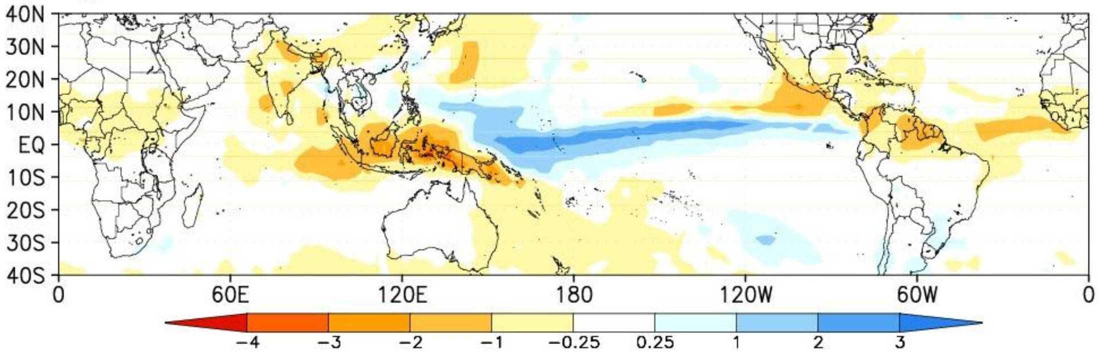

Figure 5-32: Regression of DJF and JJA of Nino 3.4 index onto DJF and JJA for GPCP rainfall for (1982-2009).

Figure 5-33 shows the same analysis in Figure 5-32. It shows a magnified picture for North Africa for the regression of Nino 3.4 onto the GPCP rainfall in North Africa for DJF and JJA. Kenya showed a positive signals of regression analysis as shown in Figure 5-33a, almost the whole ITCZ showed negative signals. The Ethiopian Highland showed the higher negative signals.

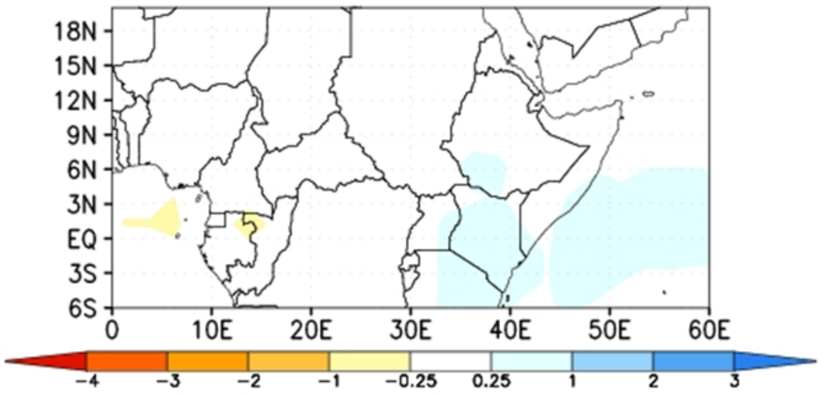
a) Regression of DJF Nino 3.4 onto DJF GPCP rainfall

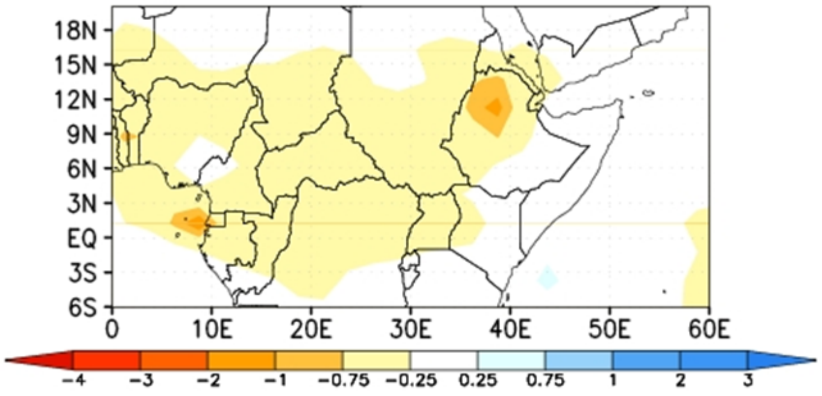
b) Regression of JJA Nino 3.4 onto JJA GPCP rainfall

Figure 5-33: Regression of DJF and JJA of Nino 3.4 index onto DJF and JJA for GPCP rainfall for (1982-2009) in North Africa.

The same analysis was performed on the ensemble mean for the two seasons (DJF and JJA). The model results agree with the observational based regression, showing no effect on the rainfall during the low flow in the upper catchment of the Blue Nile as shown in the top panel of Figure 5-34. The lower panel of Figure 5-34 shows a negative signal of the regression in Ethiopian Highland during JJA (around -1). However the band and the length of the negative regression is small compare to the observational based results.

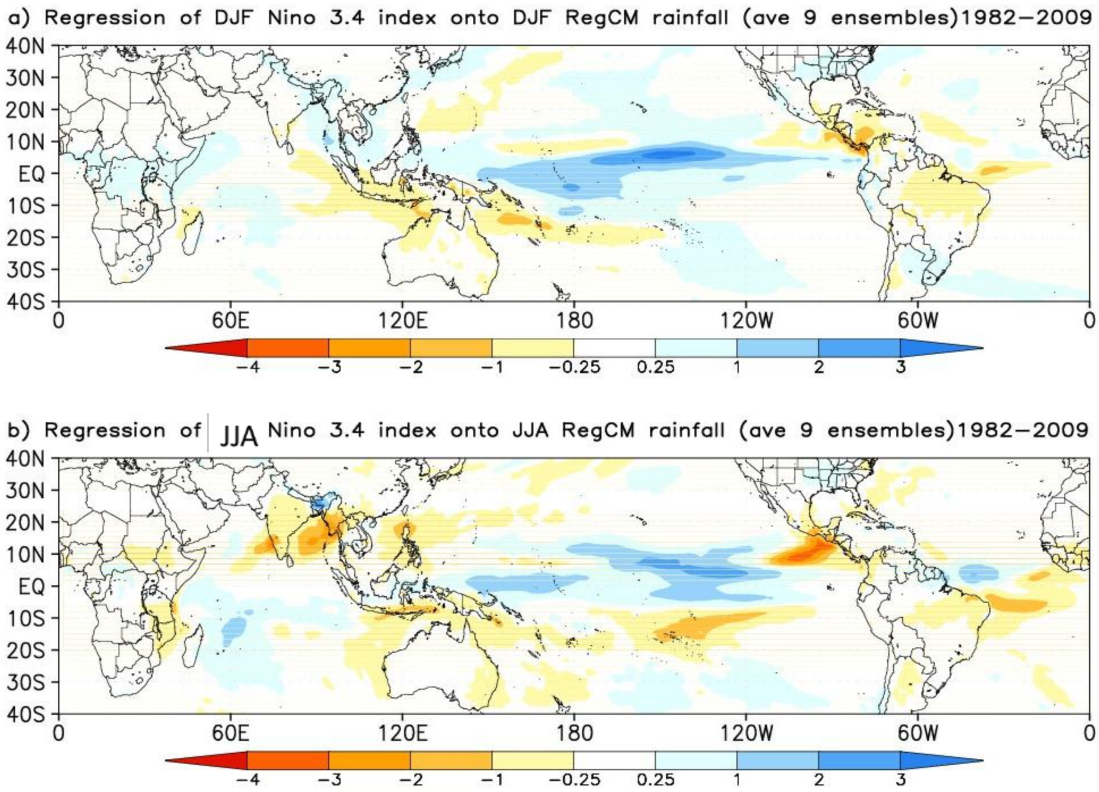
a) Regression of DJF Nino 3.4 index onto DJF RegCM rainfall (ave 9 ensembles)1982–2009

b) Regression of JJA Nino 3.4 index onto JJA RegCM rainfall (ave 9 ensembles)1982–2009

Figure 5-34: Regression of DJF and JJA of Nino 3.4 index onto DJF and JJA rainfall for 9 averaged members for (1982-2009).

Figure 5-35 shows the same analysis in Figure 5-34. It shows a magnified picture for North Africa for the regression of Niño 3.4 onto the 9 averaged members' rainfall in North Africa for DJF and JJA. Part of Kenya, and part of Uganda and the Congo Basin showed positive signals during DJF as shown in Figure 5-35 a, the Ethiopian highland and central Sudan showed negatives signals.

5.4.4 Future ENSO

The El Niño Southern Oscillation (ENSO) phenomenon plays an important role in medium to long range forecast for the Nile River (Wang and Eltahir, 1999). Monitoring and predicting ENSO can lead to disaster risk reduction through early warning. The orbital variations could affect the ENSO behaviour (Jansen et al., 2007) and the 11 year sun cycle can affect ocean temperatures associated with ENSO (Meehl et al., 2009). A study found that the long term changes in the behaviour of ENSO might happen without forcing from radiative changes (Wittenberg, 2009), wherea another study found that the change of the phenomenon could be stimulated by seasonal changes in solar insolation (Cane, 2005). Vecchi and Wittenberg, (2010) found that the variations in ENSO frequency and intensity are due to chaotic behaviour resulting from external radiative forcings. The Niño 3.4 region in the Pacific Ocean

(120 W, 170 W, 5 N, 5 S) has trend towards more frequent or stronger El Niño episodes over the past 50 to 100 years (Vecchi and Wittenberg, 2010).

a) Regression of DJF Nino 3.4 onto DJF RegCM rainfall

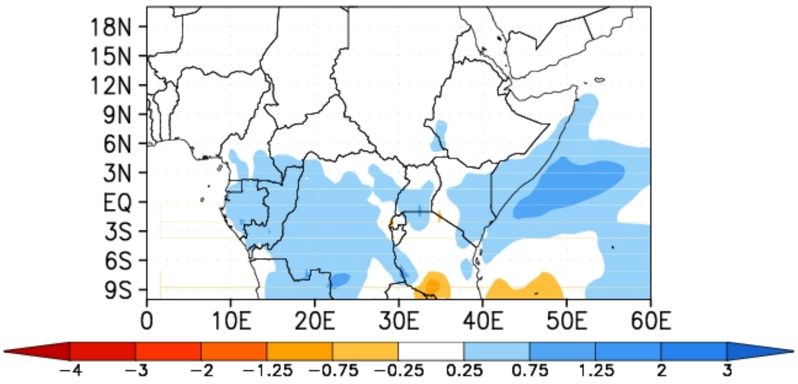

b) Regression of JJA Nino 3.4 onto JJA RegCM rainfall

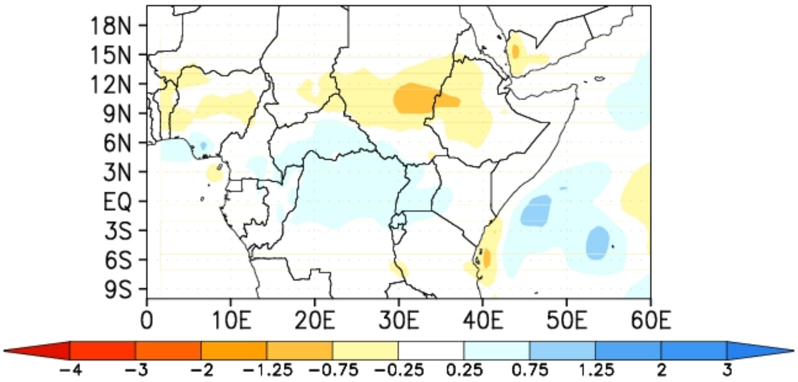

Figure 5-35: Regression of DJF and JJA of Nino 3.4 index onto DJF and JJA rainfall for 9 averaged members for (1982-2009) in North Africa.

The tendency for recent SST El Niño episodes to be centred in the equatorial Pacific more in the central equatorial Pacific than in the east Pacific (Yeh et al., 2009), and increasing in intensity for these central Pacific episodes (Lee and McPhaden, 2010). These changes in El Niño episodes may explain the extreme drought in remote areas like Horn of Africa in the recent years.

The effect of changes in greenhouse gases on the behaviour of ENSO over the past 50 to 100 years is uncertain. Yeh et al., (2009) attribute the change of the behaviour of El Niño to the changes in the temperature which, associated with increases in greenhouse gases, whereas Power and Smith, (2007) suggest that changes in the El Niño behaviour is within the range of natural variability.

The IPCC AR4 report mentions that the projected behaviour of the ENSO variability differs between models; however, all the models exhibited continued ENSO interannual variability in projections through the 21st century (Seneviratne et al., 2012).

The current limitation of understanding the ENSO activity leads to lack of confidence to predict whether ENSO activity will be enhanced or damped due to anthropogenic climate change, or even if the frequency of El Niño or La Niña episodes will change (Collins et al., 2010). This results in low confidence in projections of changes in the phenomenon. However there is some agreement by most GCMs in projecting increase of the frequency of central equatorial Pacific events (Seneviratne et al., 2012).

5.5 CONCLUSION

In this study we investigate the impact of ENSO on the upper catchment of the Blue Nile. Towards this purpose a series of 9 long simulations were made for a domain covering the entire globe between 43°S and 43°N, with only upper and lower boundary conditions from the ERA-Interim reanalysis.

The RegCM4.1 is first evaluated against observations and the reanalysis. It is shown that the model performs reasonably well in reproducing the observed climatology of temperature, precipitation, outgoing long wave radiation and large scale atmospheric circulation features. For example, the model captures well the rain belt, as well as the peaks in Ethiopian Highlands, Guinea Highlands, and Cameroon Highlands. In general, the temperature biases are approximately between -2° C and 2° C. This new simulation outperforms the previous application of this model over the region (Sylla et al. 2010b, Zaroug et al. 2012). In addition, the lower level and large-scale circulation features affecting the monsoon (TEJ, AEJ) are realistically captured.

The model (9 average members) was able to reproduce the negative correlation and showed the highest correlation also during AMJ (62%). So, this season could be used in the seasonal forecasting of the Blue Nile.

6. EARLY WARNING WITH A STATISTICAL SEASONAL FORECASTING MODEL FOR BLUE NILE SUMMER RUNOFF AT THE KHARTOUM STATION

6.1 INTRODUCTION

The task of this part of the deliverable is to present results from an analysis of the variability of hydrological drought. Improving understanding of drought variability in the case study region serves as a preliminary step for the following work on a statistical forecasting model. The statistical analyses results built the basis for the setup of statistical models of hydrological drought by providing the necessary information for the model setup. The genesis of hydrological droughts is complex with a long chain of causes and many factors. A hydrological drought can start with a shortage in precipitation but water management and water usage can often cause hydrological drought as well. The statistical approach here disregarded the management factors by relating runoff in the Blue Nile directly to atmospheric factors, hence circumventing the whole complex hydrological processes in the basin. Hence, the result can serve for two purposes: First, the pure atmospheric linkage can be analysed and second a baseline of drought forecasting can be produced. The statistical analysis investigated the complex relationship of drought in the Nile basin with climate anomalies. Since these atmospheric anomalies are known to cause drought they are the basis for various statistical methods of rainfall prediction and were employed here for early warning of hydrological drought.

In this study three forecasting schemes were tested with different models to compare the methods. The results presented here are only for the Blue Nile station in Khartoum which has the annual peak flow in August and rainy season flow lasting from June to November (Figure 6-1). The station Khartoum lays at the confluence of the Blue and White Nile (Figure 6-2). Hence, the first forecasting scheme was established for June to August at a one month lead time. The second scheme was forecasting the flow of September to November at a one month lead time. The last forecasting scheme forecasted the runoff of the whole rainy season at a three month lead time.

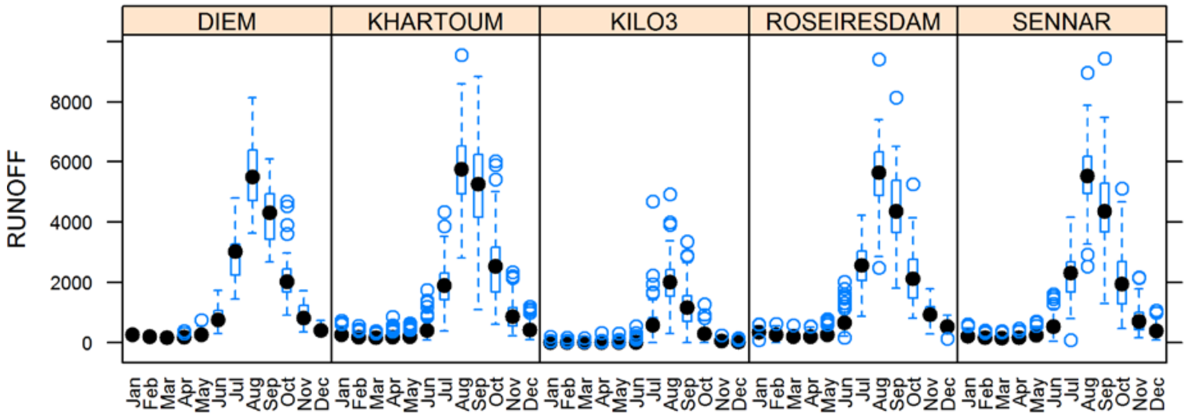

Figure 6-1: Boxplot of runoff at the stations in Blue Nile (DIEM, KHARTOUM, ROSEIRES, SENNAR) and Atbara (KILO3).

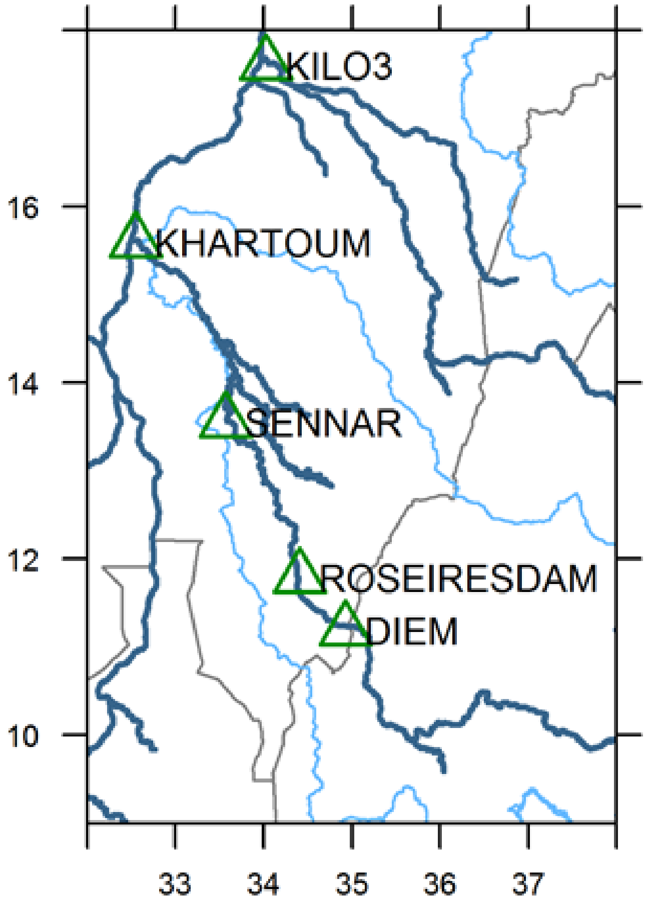

Figure 6-2 : Runoff gauges (GRDC, NFC) at the Blue Nile and Atbara with data availability in this study.

6.2 DATA AND METHODS

Table 6-1: Climate indexes used in correlation analyses

Variable / Data set	Covered period	Source
Southern Oscillation Index (SOI)	01.1951 - now	Climate Prediction Center of NOAA: ftp://ftp.cpc.ncep.noaa.gov/wd52dg/data/indices/soi
ENSO indexes (ERSST)	01.1950 - now	Climate Prediction Center of NOAA: http://www.cpc.ncep.noaa.gov/data/indices/ersst3b.nino.mth.ascii
ENSO indexes (OISST)	01.1982 - now	Climate Prediction Center of NOAA: http://www.cpc.ncep.noaa.gov/data/indices/sstoi.indices
Darwin sea level pressure (SLP)	01.1951 - now	Climate Prediction Center of NOAA: http://www.cpc.ncep.noaa.gov/data/indices/darwin
Tahiti SLP	01.1951 - now	Climate Prediction Center of NOAA: http://www.cpc.ncep.noaa.gov/data/indices/tahiti
North Atlantic Oscillation (NAO)	01.1950 - now	Climate Prediction Center of NOAA: ftp://ftp.cpc.ncep.noaa.gov/wd52dg/data/indices/nao_index.tim
Indian Ocean Dipole Mode Index (DMI)	11.1981 - now	Based on NOAA OISST Ver.2 http://www.jamstec.go.jp/frcgc/research/d1/iod/DATA/dmi.monthly.ascii
Oceanic Nino Index (ONI)	02.1950 - now	Based on ERSST.v3b of Climate Prediction Center of NOAA: http://www.cpc.ncep.noaa.gov/products/analysis_monitoring/ensostuff/ensoyears.shtml
Trans Nino Index (TNI)	03.1870 - now	HadSST1.1 until Nov 1981 and NCEP NOAA OI after: http://www.esrl.noaa.gov/psd/gcos_wgsp/Timeseries/Data/tni.long.data
NINO3.4 (HadSST)	1871 - 2011	http://www.esrl.noaa.gov/psd/gcos_wgsp/Timeseries/Data/nino34.long.data

6.2.1 Wavelet Analysis

Continuous Wavelet analysis was applied as described in (Torrence & Compo, 1998). Continuous Wavelet analysis is a common established tool for the analysis of variability in time series. It is particularly suited for signals which are caused by underlying non-stationary processes. It decomposes a signal locally (in time) into its frequency components. The signal decomposition is a powerful tool to understand the components present in a time series in which different frequencies overlay and in which frequencies change over time. Changes in the dominant frequencies can provide insight into the dynamics of a signal.

The power of a frequency at a point in time resembles the strength of this frequency at this point in time. However, similar to the Heisenberg uncertainty principle there is a trade off between localisation in time or in the frequency domain. The analysis can be either accurate in the frequency domain or in the time domain. Furthermore, in this context it is essential what type of mother wavelet function is chosen. There are several options available, which have a certain advantage in either frequency or time detection. Wavelet bases such as the Mexican hat are more accurate in the temporal domain and less accurate in the frequency domain. Hence, the Mexican hat is appropriate for example in peak detection applications. Though, detection of events was of minor interest in this study, but rather the detection of frequencies present in the runoff signal. Thus, in the present analysis the common Morlet wavelet base was applied, for it is an excellent compromise between time and frequency detection. Furthermore it has a good resemblance to the standardized time series.

In the result and discussion section 6.3 the analysis results of the Blue Nile Standardized Runoff Index (SRI) based on the Khartoum station is presented in a wavelet power spectrum. The plots show the wavelet power which is the squared amplitude for a specific frequency and time.

In statistical prediction models external predictors are used. The relation to external factors can be complex and non-stationary. The relation and similarity of two variables can be analysed using Wavelet coherence analysis (Grinsted, Moore, & Jevrejeva, 2004). The method analyses common signal properties in the time and frequency domain. Hereby, the relative phase lag between the two time series is analysed, too. Wavelet coherence plots are similar to the wavelet analysis plot. They differ in that the Wavelet coherence plots show the frequencies that both time series have in common over time. Wavelet coherence can be interpreted as a localized correlation coefficient in time frequency space (Grinsted et al., 2004). Wavelet analysis algorithms require complete records and cannot deal with missing data. The analysis was focused on records without long gaps. In some cases, gaps were filled with zeros after SRI was calculated. It is indicated in the figure captions when time series are presented, which had to be manipulated in this way.

The analysis was performed in R using the packages “dplR” and “biwavelet”.

6.2.2 Statistical forecasting

The statistical forecasting approach followed here employed two different methods: multiple linear models (MLM) and artificial neural networks (ANN). All these methods have in common that they are able to relate multiple predictors (input) to one predictand (output) variable[1]. Hence, the first step was to identify potential predictors for drought in the Blue Nile basin. Second, best predictors were chosen. Third, the models were set up with these predictors and drought forecasting performance was compared.

For the identification of potential predictors a number of climate and circulation anomaly indices were compiled. In addition, teleconnected sea surface regions were selected based on composites analysis. For example, composites were calculated for conditions during the 12 months preceding drought in early rainy season (JJA) and late rainy season (SON). See Table 6-2 for an overview of the applied composite definitions. Here, the analysis was focused on the main peak in runoff at station Khartoum, which lasts from June to November. Droughts were defined as moments in time, where the Blue Nile SRI was below a threshold of -0.5, which equals the 31 % lowest periods ($P_{standardnormal}(q< -0.5)$).

Table 6-2: Selection criteria for the composites: the Blue Nile SRI threshold regarded as drought (SRI < -0.5), the temporal resolution of a composite (time resolution), the relation of composite time to drought occurrence time (time relation), which can be contemporary or with lead time.

N◦	SPI	time resolution	time relation
C1	$SRI_1 < -0.5$	all	contemporary
C2	$SRI_1 < -0.5$	monthly	contemporary
C3	$SRI^{JJA,SON} < -0.5$	JJA, SON	preceding twelve months (August^{-1} to July and November^{-1} to October)

The set of predictors contained several non-independent variables. Hence it was affected by collinearity. For example, this was the case for the different predictors related to the El-Niño phenomenon (ENSO regions). Therefore, predictors had to be selected carefully and models had to be validated to check for overfitting. We followed a widely established approach which has also been applied by Diro, Black & Grimes (2008) for seasonal forecasting of Ethiopian rainfall. The approach is to build a multiple linear model by a stepwise selection of predictors from the set of potential predictors. The algorithm as it is implemented in the “stats” package

---

[1] ANN can also be adapted to more than one output variable

for the statistical programming environment R (R Development Core Team, 2012) was applied in a manner as follows. In the first step all potential predictors were added to individual models. For every model the Akaike information criterion (AIC) was calculated. It evaluates the model depending on the number of predictors in use. Of all the models the best was chosen based on AIC and then in the second step the remaining potential predictors were added individually to the model. Again, the predictor which gave the best AIC score was kept for the next round. This selection procedure was continued until no potential predictor lead to an improvement to the model. The resulting linear model was then further validated by analysing significance of predictors and the calculation of the root mean squared error (RMSE). The selection of predictors was analysed using a routine by Lindeman et al. (1980). Hereby the importance of the different predictors is compared by estimation of the contributed explained variance. When this is calculated from a linear model the explained variance for each predictor is biased by the set order of the predictors. The method by Lindeman et al. (1980) does approach this issue by averaging over different orders of the predictors. This gives an estimation of the explicative contribution by the predictors.

The general purpose of the seasonal forecasting is to improve drought early warning by supplying additional information to managers and decision makers involved in water resource management. Ideally, operational early warning systems would issue a warning when a forecast is likely to fall below a specific threshold. The warning would then trigger mitigation actions or other action improving preparedness. Therefore, the thresholds have to be set carefully in advance by local early warning experts in respect to the envisaged actions. Hence, the information needed for the early warning system consists of a warning threshold and a related probabilistic forecast. In this study we set the drought warning threshold of the standardized runoff index to -0.5. In order to make use of a multiple linear model forecast for early warning, we estimated the average error from the residuals of the calibration data set. Following the assumption inherent to multiple linear models we assumed normally distributed residuals with a standard deviation equaling the residual standard error. This normal distribution was applied to calculate the probability for droughts for the forecasted values. In this way it is possible to transform the deterministic discrete MLM forecast to a probabilistic categorical forecast (Diro, Grimes, & Black, 2011).

Multiple linear models and linear discriminant analysis have one major shortcoming, which is their inability to model non-linear processes. However, atmospheric processes are very likely to be non-linear (Mwale et al., 2007). Hence, Mwale et al. (2007) successfully applied artificial neural networks for the prediction of summer rainfall in southern Africa, since ANN are capable of representing more complex non-linear relationships between variables. Here, we applied artificial neural networks, which were trained with the genetic algorithm (ANN-GA). As input layer the predictors from the MLM were chosen. This step of the model development shows if the inclusion of non-linearity can improve the model fit. The artificial neural networks as they were employed here consisted of three layers: one input layer, one hidden layer and one output layer. Each layer contained a number of neurons, which had to be predefined before the training procedure. The input layer contained as many neurons as there are variables in the predictor data set. Every neuron handled the data of one of these variables. The number of neurons in the hidden layer determined the complexity of the model. When networks are designed with a high number of neurons, they also have many parameters, which generally increase the risk of overfitting. However, Lawrence et al. (1997) found that ANN are not very prone to overfitting even when set up with a higher degree than necessary. Nevertheless, here the available data was small, so chances of overfitting are high. In order to check the influence of the number of neurons, two different designs were set up: one ANN with three and one ANN with 10 neurons in the hidden layer. The output layer contained one neuron only which was the predictand. Prior to the training procedure all input and output data was scaled to the range 0 to 1.

The algorithm employed for network training is called “genetic algorithm” and it applies the principles in genetic evolution for training of neural networks. The algorithm used here is implemented in the R package “ANN” (Roy-Desrosiers, 2012). The principle of the training algorithm is that a population of neural networks moves from one generation to the next, a process during which survival of the fittest, mutation and crossover (gene transfer) apply. Initially, a population of neural networks is created, where all parameters (weights and biases) are set at random. Here, the initial population size was set to 3000. The fitness of the networks is measured by the sum of squares of the residuals. The mutation rate was set to 5% and crossover rate was set to 0.8.

From each generation 5% were kept unaltered for the next generation. The least fittest 5% of a generation are removed and replaced by mutated –randomized – individuals in the next generation (mutation rate). For the rest of the individuals a one-point crossover representing a gene transfer is processed by randomly selecting a parameter within two networks which are exchanged between the two parents to create the two children networks for the next generation.

Following the calibration and training, the models were validated. The fit of any given model was evaluated by the coefficient of determination (R^2), the mean squared error (MSE) and the root mean squared error (RMSE). When calculated based on the training data, these measures indicate the quality of fit of a model. However, the ability to represent the training data does not lead directly to good generalization performance by the model. In order to test the generalisation ability a leave-one-out cross validation scheme was applied. With this approach, both MLM and ANN-GA were analysed, for it was an applicable way to validation.

Cross validation provides an estimate of the model error for independent data. For a dataset of length n it does so by splitting the calibration data set in n parts and train the model n times by excluding one value in each turn. Then, each model is validated with the single independent value. The resulting MSE is then averaged for all runs to obtain MSE_{cv}. It is possible then to compare the RMSE based on the complete calibration data with the $RMSE_{cv}$ from the cross validation. A perfect model would result in no difference between the two errors. Although normally, there is a difference, and the more $RMSE_{cv}$ exceeds RMSE, the weaker is the generalisation performance of a model. Reasons for this can be overfitting or unsuitable predictors.

The models compared here were evaluated in an early warning setting. As already mentioned (see above) this involves the selection of a threshold for a warning. For demonstration purpose in the report the threshold was set to SRI < -0.5, which approximates 31 % of the driest values. By application of the threshold the observation time series was transformed to a binary variable, which indicated drought and non-drought events. A warning is issued when the forecasted probability for the value is high to fall below the threshold. If warnings are issued at very high drought probabilities only, then on the one hand most warnings would be correct, on the other hand it would be likely that some drought events are missed. In contrast, if warnings are issued at low probabilities already, then more events would be detected early but at the price of a higher false alarm rate.

Missed events and false alarms both lower the credibility of an early warning system. Decision makers can set the alarm triggering probability depending on the importance of hits versus false alarms. Depending on the circumstances of the decision maker or the early warning institution false alarms are regarded differently. Here, we analysed the early warning systems performance of models with receiver operating characteristics (ROC), which is a plot that displays the hit rate vs the false alarm rate depending on different levels of forecast probability. Hereby, the plot eases the definition of the early warning trigger. The diagonal resembles a random forecast of no skill since hit rate and false alarm rate are always equal and independent of the probability trigger threshold. If a forecasting model has any value then the curve is higher than the diagonal. ROC analysis also offers the so called ROC score to compare different models. The ROC score is the area below the curve and ranges between 0 and 1. The no skill diagonal already reaches an area of 0.5 so that models have skill only when they have ROC scores higher than 0.5.

The analyses in this report used hydrological and sea surface temperature data of the HAD ISST1.1 data set (Rayner, 2003). Runoff data sources analysed here are from the Global Runoff Data Centre (GRDC, http://www.bafg.de/GRDC), and provided by the DEWFORA partner NFC (Nile forecast center). Runoff data was available for the stations Khartoum, Sennar, Roseires and El Diem in the Blue Nile (Figure 7-2). Furthermore, metadata such as catchment boundaries and rivers were taken from the free HydroSHEDS data set (http://hydrosheds.cr.usgs.gov/). Country boundaries were used from the Global Administrative Areas database version 2.0 (GADM, http://www.gadm.org/) or as available in the R package "maps" which builds upon the CIA World Data Bank II (http://www.evl.uic.edu/pape/data/WDB/).

The available runoff for the stations did not cover the complete available period in either of the data sources; hence runoff timeseries were created by combining the GRDC and the NFC data. Then, the Standardized Runoff Index (Shukla & Wood, 2008) was calculated for the runoff time series. See DEWFORA deliverable 4.6 (Seibert and Apel, 2012) for details on the preprocessing procedure. The station Khartoum was focused since it had highest data coverage.

6.3 WAVELET ANALYSIS: VARIABILITY ANALYSIS OF STANDARDIZED RUNOFF INDEX

Runoff in the Blue Nile naturally shows seasonality which was presented in Figure 6-1. Droughts are anomalies during which runoff is lower than the longtime averages. The strength of these anomalies was calculated by the standardized runoff index (SRI). The SRI series is normally distributed and shows the runoff anomaly at a monthly aggregation. We focused the analysis of runoff variability on the anomalies in the runoff signal at the station Khartoum. From the start of the time series in 1900 until 1920 the SRI signal showed power on three bands: periods 1, 2-3 and the 5-8 year (Figure 6-3). From 1920 on the wavelet power decreased which was caused by lower variability with the effect that only few regions in the wavelet power spectrum were still significant. Until 1950 periods of 10 years were still significant at the 95% level. However, over the complete record power in the range of 5 to 10 years was still high and from 1970 on the wavelet power increased again up to a significant level. The power on the band 2-3 years which was strong until 1920 was still high until 1950. From 1950 on the power was only present for short periods. Periods of one year were also only significant for short periods with an extended gap from 1930 to 1950.

The signal properties are characterized by non-stationarity with a decreased variability from 1920 to 1980. However, the presence of 5-10 year periods throughout the whole signal indicated that factors of variability were very stable and should be predictable. The ENSO signals also had frequencies in that range so it is likely that the wavelet power on these 5 -10 years band are caused by the connection to El Niño as was depicted in sections 5 and 6.

The relationship of ENSO to precipitation in Ethiopia is relatively strong and the wavelet analysis of the SRI signal indicated this as well. During El Niño events the sea surface temperature is elevated in the NIÑO regions of the Pacific and precipitation is lower than normal.

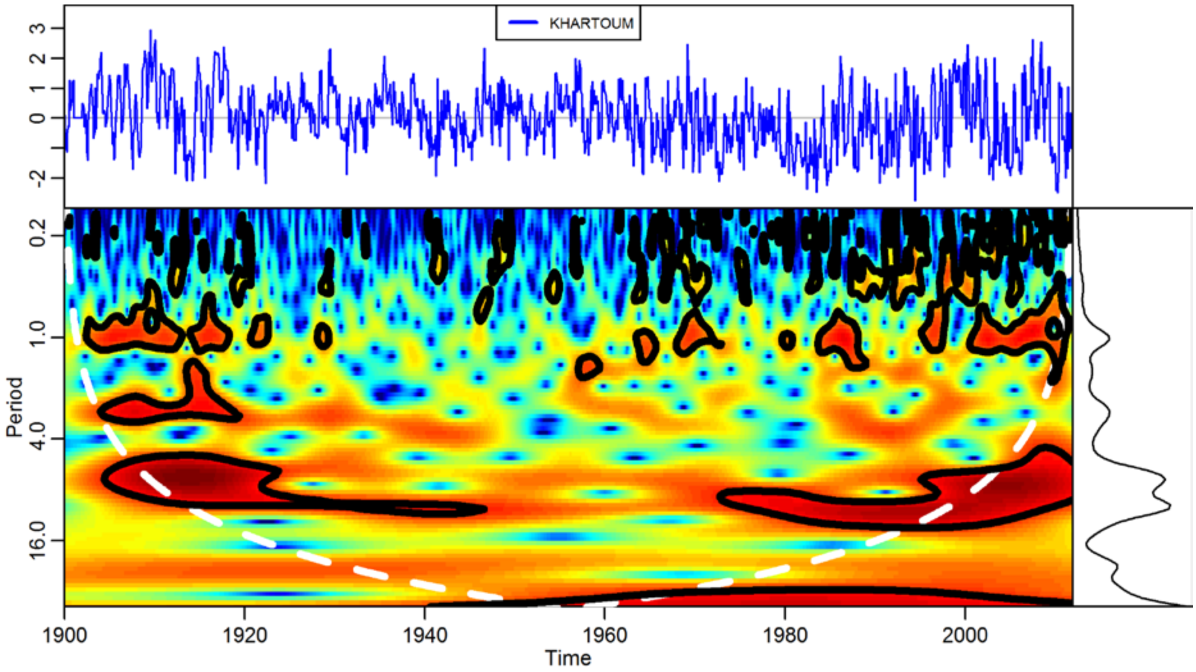

Figure 6-3: Khartoum (Blue Nile): Standardised runoff index time series (upper), wavelet power spectra (lower) and the global wavelet spectrum (right); contours show significance at 0.05 level.

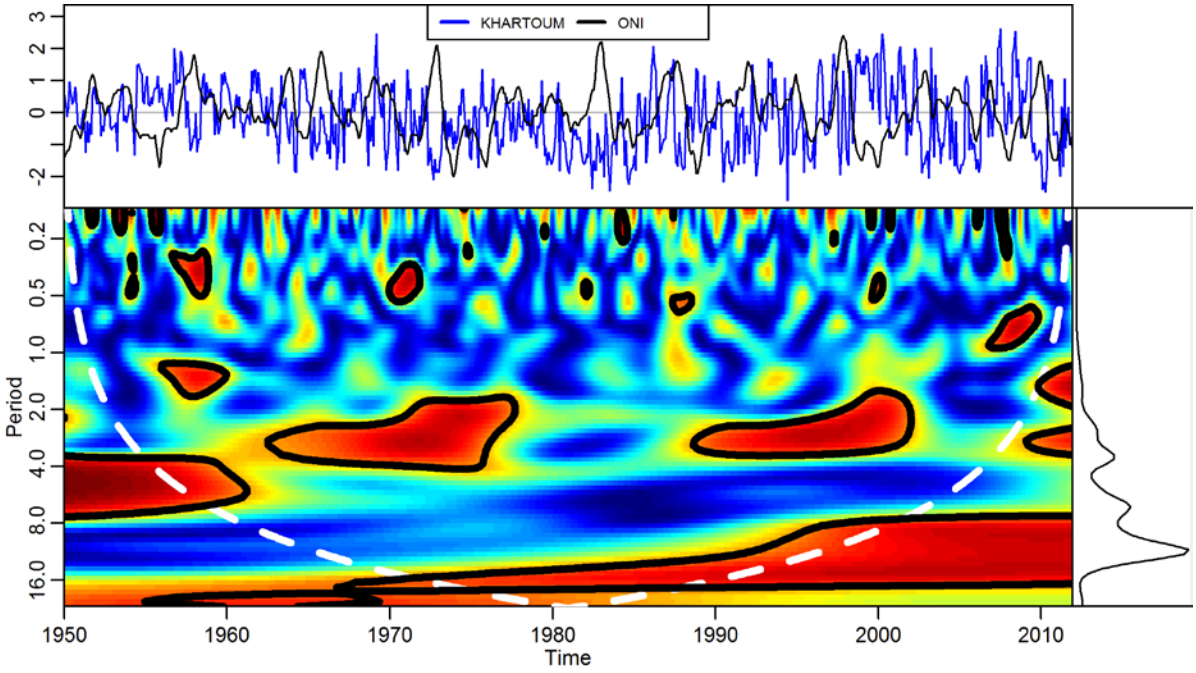

Figure 6-4: Khartoum (Blue Nile): Standardized runoff index and Oceanic NINO Index (ONI) time series (upper), wavelet coherence plot (lower) and global power spectrum (right); contours show significance at 0.05 level.

The signal properties of the ENSO and the Khartoum SRI can be compared using wavelet coherence analysis to highlight common properties. The Oceanic Niño index is a modified index of the NIÑO3.4 SST in the equatorial Pacific which is available since 1950 with good reliability and consistency in the data basis. The wavelet coherence indicated common signal properties in the 2-4 year band during two time spans of ca. 10 years (Figure 6-4). The coherent wavelet power was significant from 1965 to 1975 and from 1990 to 2000. During the first period one of the strongest El Niño events occurred and coincided with one of the major and extended droughts (1973/1974). The signal coherence was high since the dynamics of the event were very similar with a similar duration. Approximately 10 years later in the early 80's a very strong El-Niño event developed rapidly. At the same time the low SRI values indicated a long period of hydrological drought. However, the dynamic of the two signals did not match well and caused the absence of wavelet coherence in the 80's. The wavelet coherence on longer decadal periods of ca. 16 years was strong though and developed since the late 60's. These examples demonstrate the complexity of the relationship between ENSO and the runoff signal.

6.4 POTENTIAL PREDICTORS

Seasonal prediction of Ethiopian precipitation was presented in several publications (Diro et al. (2008)) which employed the relationship to El-Niño in the region. Hence, the attempt presented here also included the El-Niño southern oscillation indices (ENSO) and a number of other indices which are presented in Table 6-1 (NAO, DMI). These climate anomalies are propagated through the atmosphere and influence the regional atmospheric dynamic (Diro et al., 2011). The impact on precipitation anomalies is then established by changes in the atmospheric moisture transport trajectories or atmospheric moisture content. The most important oceanic moisture sources for the Horn of Africa are the Red Sea, the Mediterranean Sea and the Indian Ocean (Gimeno et al., 2010). Additionally, the Congo basin is an important continental moisture source. Sea surface temperatures in the oceanic moisture source regions influence the local evaporation and then the available moisture in the atmosphere. Hence, the list of potential predictors was extended by several predictors based on Ocean regions that were related to droughts in the Blue Nile basin. These regions were defined by analyses of composites.

6.4.1 Teleconnections with Indian Ocean and Atlantic sea surface temperature

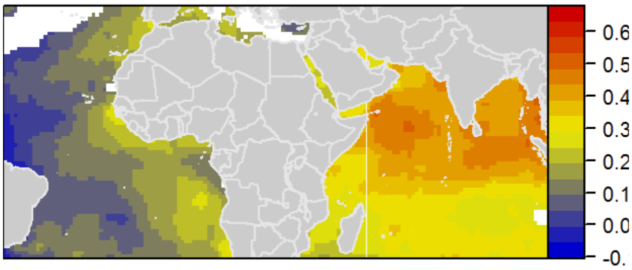

Figure 6-5: Composite (1) of sea surface temperature anomalies for hydrological drought in the Nile basin (Khartoum), significant anomalies displayed, only.

Sea surface temperature composites of drought in the Blue Nile basin were calculated to identify Ocean region with significant anomalies. Droughts occurred generally when temperatures in the northern Indian Ocean were higher than normal (Figure 6-5 to the right). In the composite of all droughts (composites 1) the temperature anomalies in the Atlantic were close to normal or slightly below zero. The conditions during droughts differ depending on the time of the season. In order to analyse this aspect, composites were calculated for every month of the year separately (Figure 6-6). There was a well pronounced difference in sea surface temperature anomalies between the months April, May, July and the rest of the months. The majority of months had positive temperature anomalies in the Indian and Atlantic Ocean. Spots with highest anomalies lay in the northern Indian Ocean, along the eastern African shoreline, the southern Indian Ocean and the southwestern Atlantic. From March to August, these anomalies are much weaker and even absent due to non-significance in April, May and July. In May the coastal region from the Gulf of Guinea to the Angolan Coast had colder than normal temperatures. From June to August the sea surface temperatures in the Mediterranean and Red Sea were colder than normal. Even though the Red Sea is an important source of oceanic moisture for the Ethiopian highlands, the sea surface temperature in the Red Sea only showed very few significant anomalies. In addition to the cold anomalies in July and August there were positive anomalies in January and October.

The results of the composites consecutive to hydrological drought conditions are surprising. During the peak runoff season from June to November the SST anomaly patterns change very much and do not show consistent temperature anomalies. Reasons may be either very complex atmospheric processes which cannot be represented by composites or the period of monthly composites may be too short since runoff may depend on longer lasting anomalies.

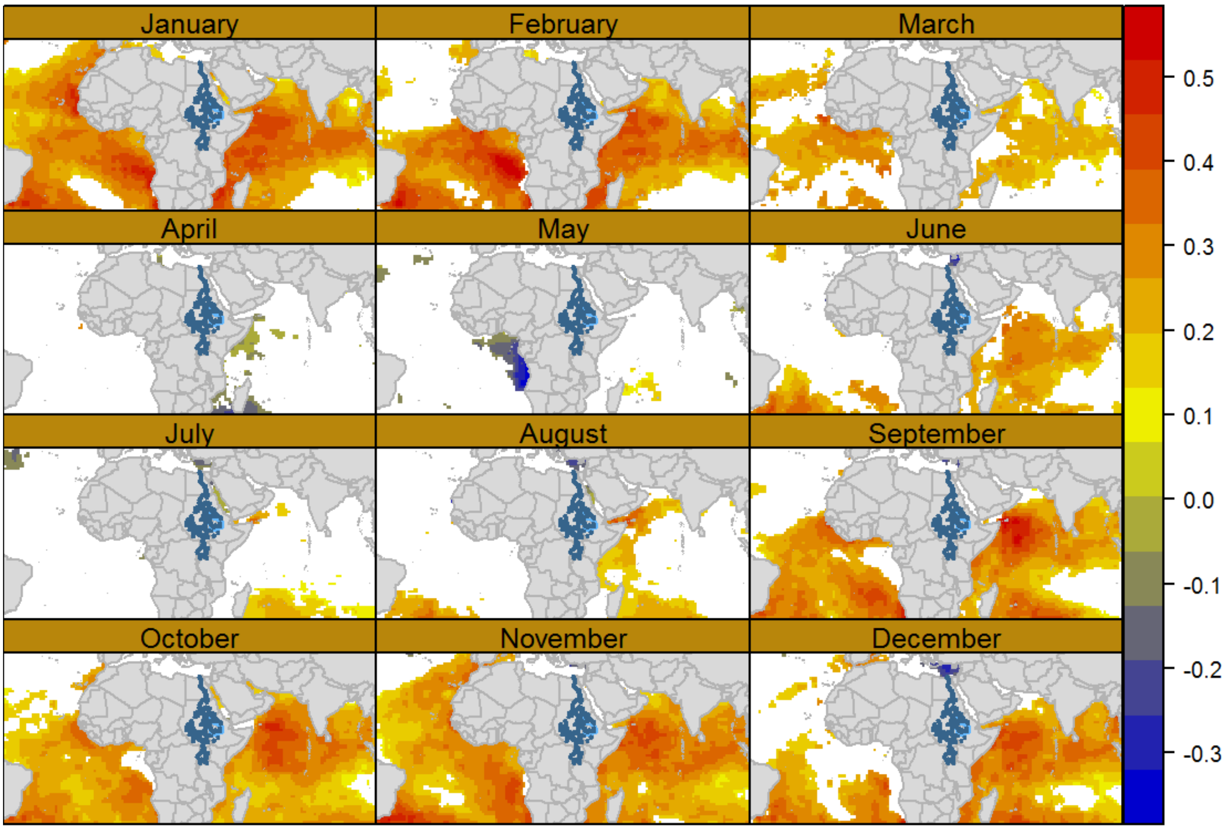

Figure 6-6: Composite (2) of sea surface temperature anomalies for months in hydrological drought in the Nile basin (Khartoum), significant anomalies displayed, only.

In order to focus the composites analysis on the forecasting approach in this study, composites class no. 3 was calculated for the preceding 12 months of droughts early in the rainy season (JJA) and late in the rainy season (SON). Hereby, regions with potential predictive capability could be extracted. Preceding to hydrological droughts for June to August SRI_{JJA} the northern Indian Ocean was warmer than normal (Figure 6-7). From January to June the Atlantic showed a positive anomaly at the Coast of Angola in the Southern Atlantic. Cold anomalies were present in the Mediterranean and Red Sea, although not consistently. Droughts in the second half of the rainy season (September to November) were also preceded by positive SST anomalies at the Angolan shore and by negative anomalies in the Mediterranean Sea and the Red Sea (Figure 6-8). The complete list of selected regions is presented in Table 6-3 and Figure 6-9 presents the position of the regions.

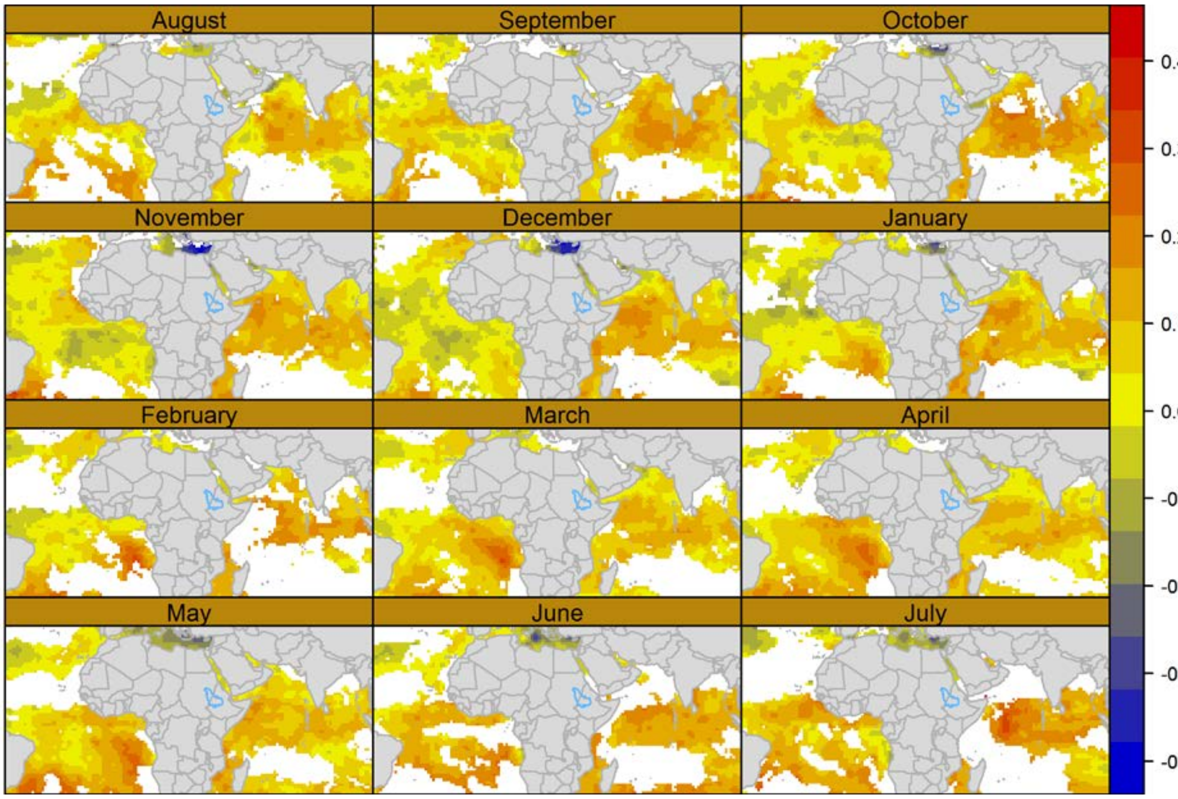

Figure 6-7: Composite (3) of sea surface temperature anomalies for the 12 months preceding a hydrological drought from June to August in the Nile basin (SRI_{JJA} in Khartoum), significant anomalies displayed, only.

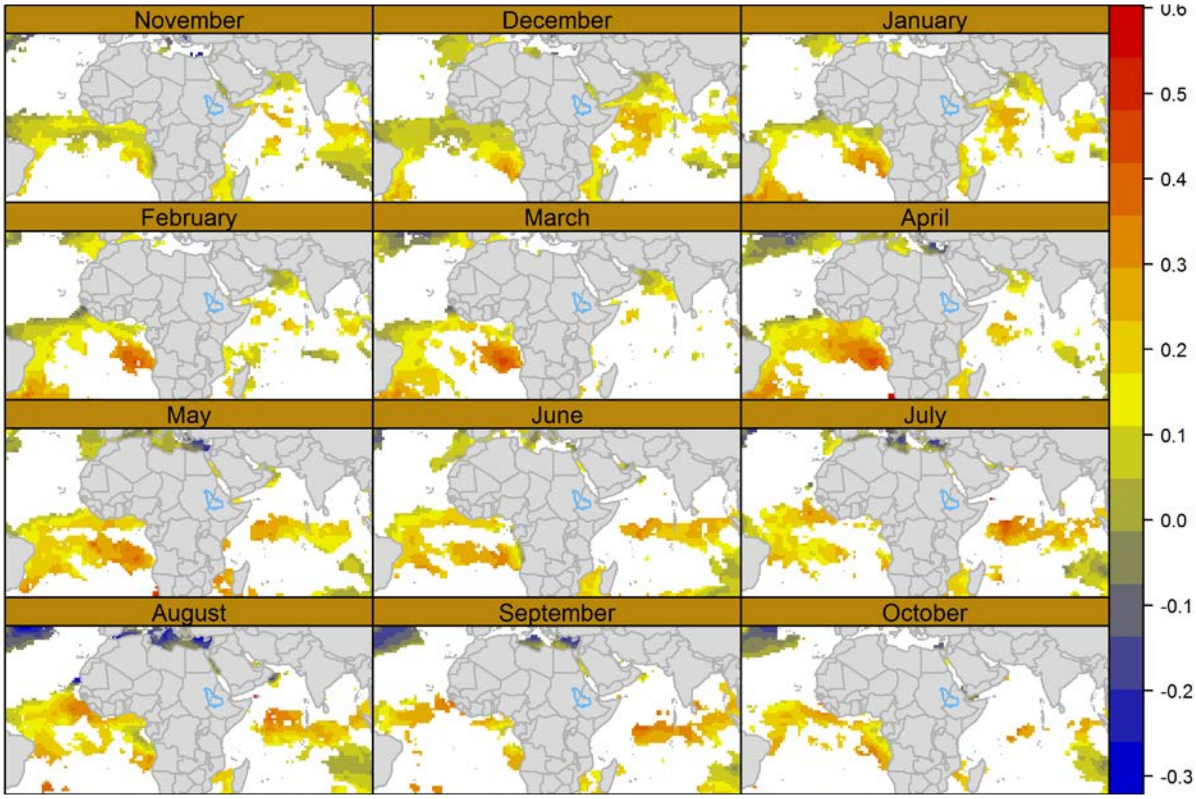

Figure 6-8: Composite (3) of sea surface temperature anomalies for the 12 months preceding a hydrological drought from September to November in the Nile basin (SRI_{SON} in Khartoum), significant anomalies displayed, only.

Table 6-3: Potential predictors for precipitation variability in the Blue Nile basin, detected by composites analysis. Parameters are sea surface temperature (SST), the types of the reference composites (see Table 6-2) are indicated in the last column with the months and respective lead time.

Ocean	Region	Latitude (min, max)	Longitude (min, max)	Composite (lead time)	Abbreviation
Atlantic	Angola shore	-18 -3	-2, 10	$C2_{J,F,O,N,D}$, $C3_{JJA}$(2-6), $C3_{SON}$(2,1)	AngolaCoast
	Brasilian shore	-15, -26	-20, -46	$C2_{J,F,N}$, $C3_{JJA}$(1-8), $C3_{SON}$(5-8)	BCoast
	Northern Atlantic	33, 41	-30, -46	$C3_{JJA}$(0), $C3_{SON}$(1-0)	NAtl
Indian Ocean	Horn of Africa	2, 13	45, 65	$C2_{J,F,A,S,O,N,D}$, $C3_{JJA}$(0-10), $C3_{SON}$(8-9)	HoA
	western equatorial	-5, 5	52, 67	$C3_{JJA}$(0,8,9), $C3_{SON}$(0-5)	weqIO
	Mozambique shore	-28, -15	40, 45		Moz
	Tansanian shore	-15, 4	40, 45		TanC
Red Sea	All	32, 44	14, 30	$C2_{Jan,Jun,O}$, $C3_{JJA}$(0-10), $C3_{SON}$(0-4,9,10)	RedSea
Mediterranean Sea	Eastern	22, 36	30, 38	$C2_{J,J,A,D}$, $C3_{JJA}$(0-10), $C3_{SON}$(0-5)	eMedSea
	Western	22, 36	30, 38	$C3_{JJA}$(0-7), $C3_{SON}$(1-4)	wMedSea

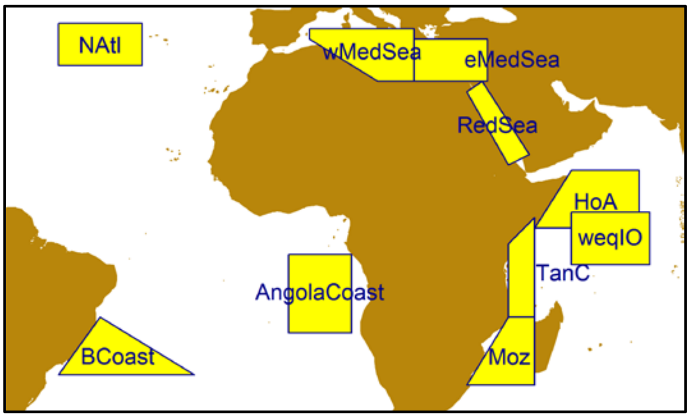

Figure 6-9: Teleconnected regions established by correlation and composites analysis.

6.5 STATISTICAL MODEL SETUP

6.5.1 Predictor selection

Here, the results of the parameter selection and model setup are presented for Khartoum in the Blue Nile at different lead times. The first forecast scheme was a forecast of the early rainy season at one month lead time. This means that a forecast for June to August runoff (JJA) was made in May based on the data of April. The second forecasting scheme was a forecast of the late rainy season at one month lead time, which is in detail a forecast for September to November runoff (SON) in August based on the data of July. The last forecasting scheme presented here was a forecast of the late whole rainy season with a three month lead time, so that June to November runoff (JJASON) was forecasted in April based on the data of February. The selection of predictors from the list of potential predictors was performed with stepwise selection for multiple linear models. The selection is a process which is sensitive to the selection criteria. When selection was performed with the Akaike's information criterion (AIC) the resulting models had a higher coefficient of determination than with the Bayes information criterion (BIC). The BIC is more conservative than the AIC since the penalty for the number of parameters is higher. As a result, less parameters are selected and the coefficient of determination is lower. In cases where this effect is strong it is likely, that some of the parameters only contributed little additional model skill. For all Forecasting schemes the AIC selected model not only reached the highest coefficient of determination, the models also had good generalization properties. For these models interaction between factors was also tested and subjected to the same parameter selection procedure as before. Of the three models the one for the late rainy season had the highest coefficients of determination (Table 6-4). The multiple linear model reached 0.52 and the ANN improved upon this up to a value of 0.8. Interaction between the model parameters did only play a minor role as shown by the small difference in the coefficients of determination. The explained variance in the model for the early rainy season forecast was low with only 0.24. The parameters and their importance will be discussed in the following paragraph.

Table 6-4: Coefficients of determination for the multiple linear model without (MLM), with interaction (MLM-i), the artificial neural network with 10 (ANN-10) and 3 hidden layers (ANN-3) for the forecasts at one month leadtime (lead1) and three months lead time(lead3) of runoff in JJA (SRI3Aug), SON (SRI3Nov) and JJASON (SRI6Nov).

Forecast	**MLM**	**MLM-i**	**ANN-10**	**ANN-3**
SRI3Aug_lead1	0,24	0,26	**0,39**	0,35
SRI3Nov_lead1	0,52	0,55	**0,80**	0,72
SRI6Nov_lead3	0,35	0,35	**0,75**	0,54

All models included one predictor related to ENSO, but all models picked different combinations (Figure 6-10). The estimated explicative contribution presented in Figure 6-10 for all parameters and models is an indicator for the importance of each predictor. In the early rainy season forecast model the Oceanic Niño index was selected, but was only in second place in explicative contribution to the model. The Red Sea SST anomaly did have a higher importance. In model for the late rainy season the NINO 3.4 region was selected and was far most important for the model. In contract to model one the SRI at the time of prediction was selected as well. This indicates that hydrological drought early in the rainy season persists to the late rainy season. The model for forecasting the whole rainy season runoff at 3 month lead time was built with the Niño 4 region index. In this model almost all parameters had equally low explicative contribution of ca. 0.06. The SST of the shore of Angola (SST_KongoCoast_f1) was selected for the late rainy season model and the model for the whole rainy season. Though, the explicative contribution was low in both models. All three interactive models had one interactive parameter. In the model of the whole rainy season this parameter replaced the SST temperature of the ocean region in the western Mediterranean Sea.

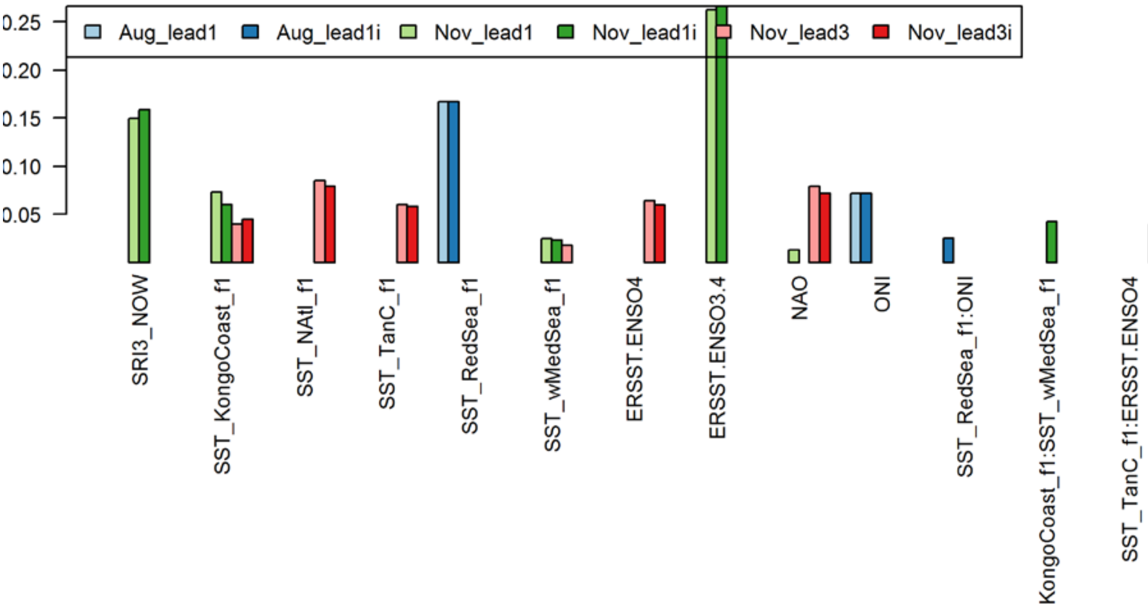

Figure 6-10: Multiple linear models: Estimated explicative contribution of predictors for the three forecasts without interaction and with interaction ("i" appended).

6.5.2 Model validation

In the previous section the predictor selection results and model fit performances were presented. In Figure 6-11 to Figure 6-13 results of the fitted models are presented. For all the stations the artificial neural network with 10 neurons in the hidden layer reached the best fit. Particularly, extreme events were captured much better by the ANN than with the linear model (AIC selection, AMJ predictors). The simulations of all models were missing parameters for the time before 1950 which is why no forecasts were calculated for these months.

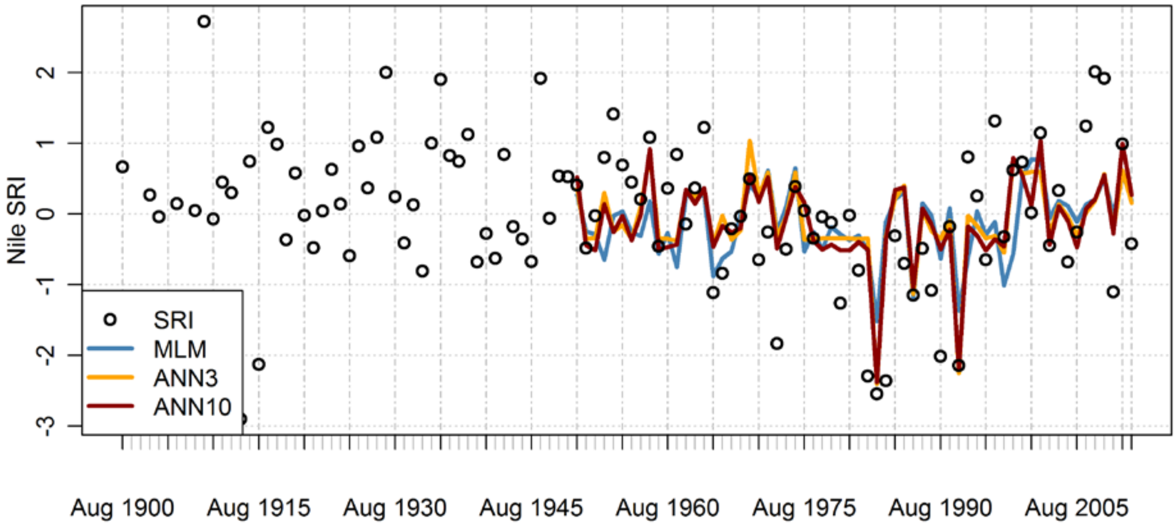

Figure 6-11: One month lead time forecast of early rainy season runoff (SRI_{JJA}) at station Khartoum: Model fits of multiple linear model (MLM) and artificial neural networks (ANN) with two degrees of complexity, one with 3 neurons (ANN3) and the other one with 10 neurons (ANN10) in the hidden layer, first half of the observation period could not be fitted due to missing input data.

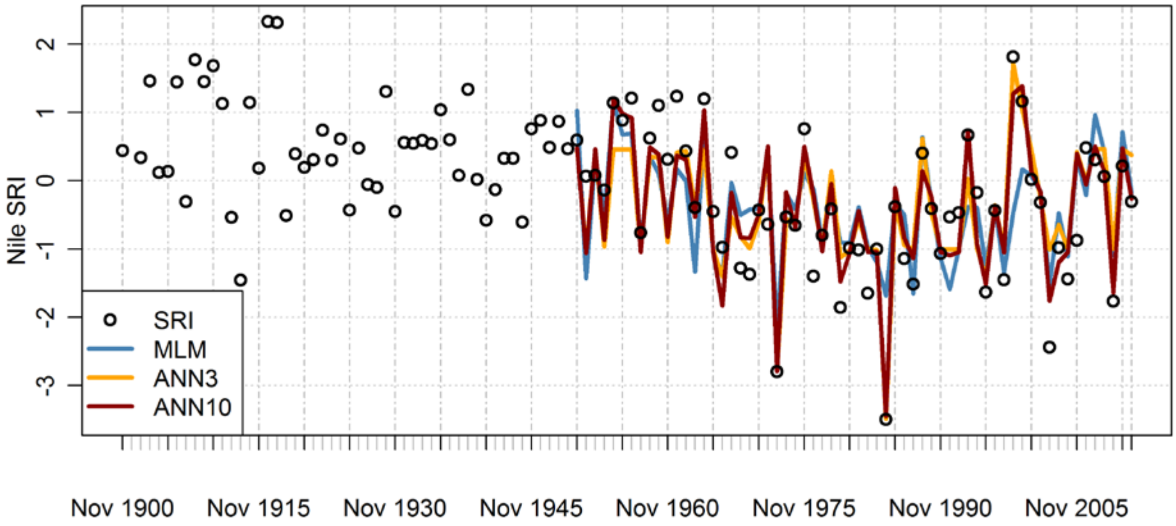

Figure 6-12: One month lead time forecast of late rainy season runoff (SRI_{SON}) at station Khartoum: Model fits of multiple linear model (MLM) and artificial neural networks (ANN) with two degrees of complexity, one with 3 neurons (ANN3) and the other one with 10 neurons (ANN10) in the hidden layer, first half of the observation period could not be fitted due to missing input data.

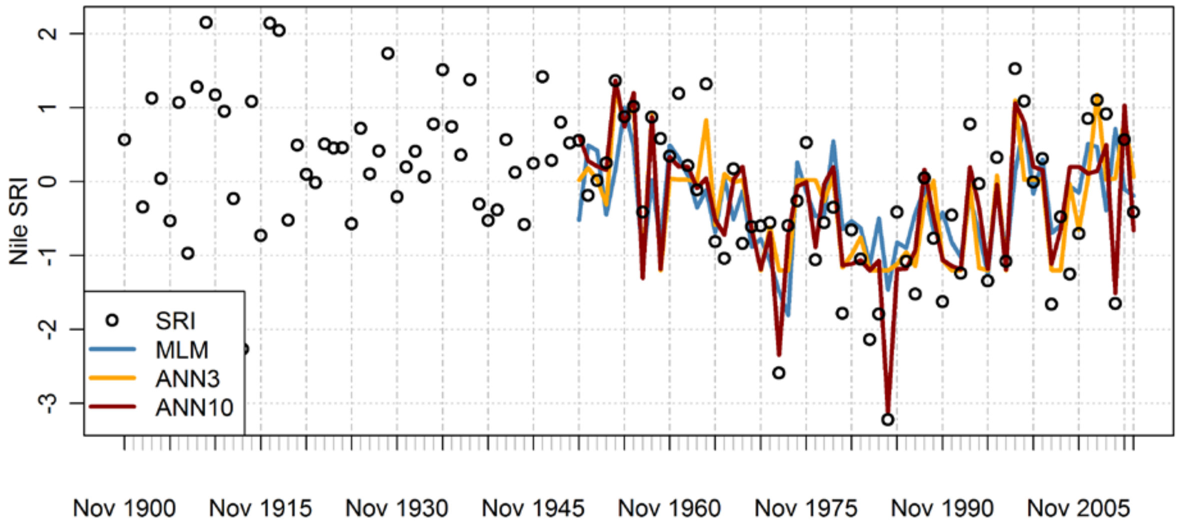

Figure 6-13: Three months lead time forecast of rainy season runoff (SRI_{JJASON}) at station Khartoum: Model fits of multiple linear model (MLM) and artificial neural networks (ANN) with two degrees of complexity, one with 3 neurons (ANN3) and the other one with 10 neurons (ANN10) in the hidden layer, first half of the observation period could not be fitted due to missing input data.

The simulations at all station were improved with the artificial neural networks. The ability for non-linear relationships was capable of representing the extreme values much better than the linear models. However, these results did not give any reliable indication of the generalisation performance of the models. This issue was addressed by applying leave-one-out cross validation. Using cross validation the root mean squared error (RMSE) for independent data can be estimated which gives a good estimation of the forecasting performance of a model. Models for which the RMSE of the cross-validation is much higher than the RMSE of the calibration have only low skill and have weak generalisation performance. As expected from the discussed results so far, the RMSE of the MLM is higher than for both ANNs (Table 6-5). However, the cross-validation showed that for all models the cross-validated RMSE increases by far more in the ANN than for the MLM. The resulting RMSE for the MLM was lowest for the forecast of late rainy season with only 0.60 (interaction MLM). The cross-validated RMSE was highest for the model of the whole rainy season. However, in all three forecasting schemes the MLM with interaction showed a comparatively low cross-validated RMSE. The generalisation was particularly good for the late rainy season forecast. These model errors are very high in regard of the standard deviation of one in the standardised runoff data.

Table 6-5: Root mean squared errors from calibration data (ALL) and from leave-one-out cross validation (CV) for the multiple linear model without (MLM), with interaction (MLM-i), the artificial neural network with 10 (ANN-10) and 3 hidden layers (ANN-3).

Forecast	run	MLM	MLM-i	ANN-10	ANN-3
SRI3Aug_lead1	ALL	0,90	0,72	0,78	0,81
	CV	**0,91**	0,81	0,83	0,93
SRI3Nov_lead1	ALL	0,76	0,60	0,47	0,55
	CV	0,80	**0,60**	0,85	1,06
SRI6Nov_lead3	ALL	0,88	0,75	0,51	0,69
	CV	**0,93**	0,84	1,08	1,26

6.5.3 Model performance for drought Early Warning

Several types of statistical methods were developed, of which the multiple linear models with interaction exhibited the best generalisation performance. For drought early warning it was necessary to calculate probabilities for drought and flood based on the forecasting models. In accordance to tercile forecasts the thresholds for drought and flood were set to -0.5 and 0.5 and the respective probabilities were calculated. In Figure 6-14 to Figure 6-17 the results are presented with a simulated warning for the class with highest probability.

The early warnings of one month lead time forecast of early rainy season runoff did forecast all extreme drought events correctly but many false warnings were issued. In one case there was even a drought warning issued and a flood occurred. The ROC score of the presented MLM with interaction was the same as for the MLM without interaction, which shows that the models early warning performance is the same (Figure 6-16, left). With a ROC score of 0.78 the skill is low.

The linear models for the late rainy season early warning at one month lead time had better skill and reached a ROC score of 0.85, both (Figure 6-16, right). In this case this mean that if the early warning threshold would be set to a drought probability of 50%, then the false alarm rate would be lower than 30 %. This is still a high proportion but the best result of all the statistical models in this study.

The linear models for the seasonal early warning with a lead time of 3 months showed the lowest skill with ROC scores of 0.72. Even though many droughts were early warned correctly, there were several floods where the early warning would have been issuing a drought warning. These kind of false warnings are lethal to the credibility of a warning system and the issuing organization and are hence critical for operational use. Even when the early warning probability thresholds would be set to a high value like 0.5, the false alarm rate would be higher than 0.3 (Figure 6-18).

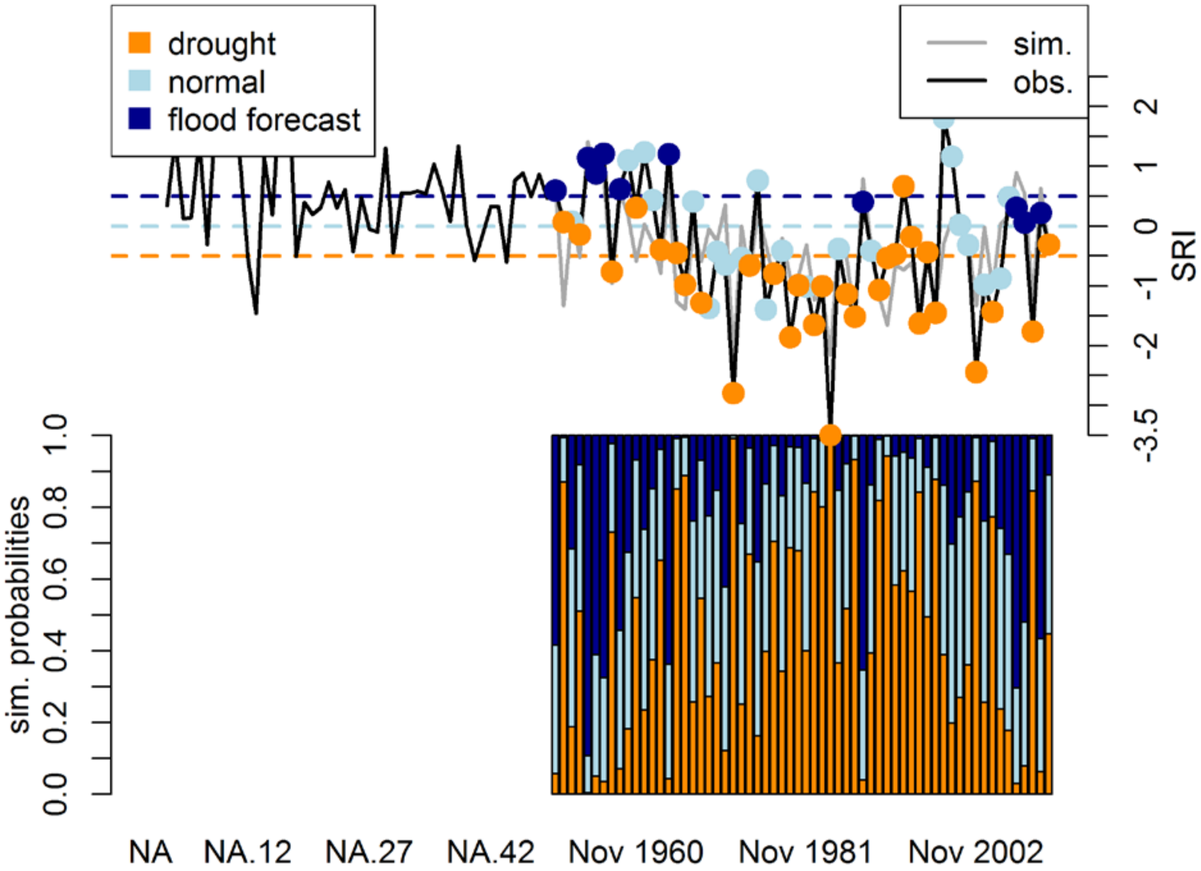

Figure 6-14: One month lead time forecast of early rainy season runoff (SRI_{JJA}) at station Khartoum: Early warnings of the multiple linear model with interaction. Above: simulation (grey line) and observed values (black line) with early warnings one month ahead for class with highest probability (coloured points). Below: Probabilities for flood (dark blue), normal (bright blue) and drought (orange).

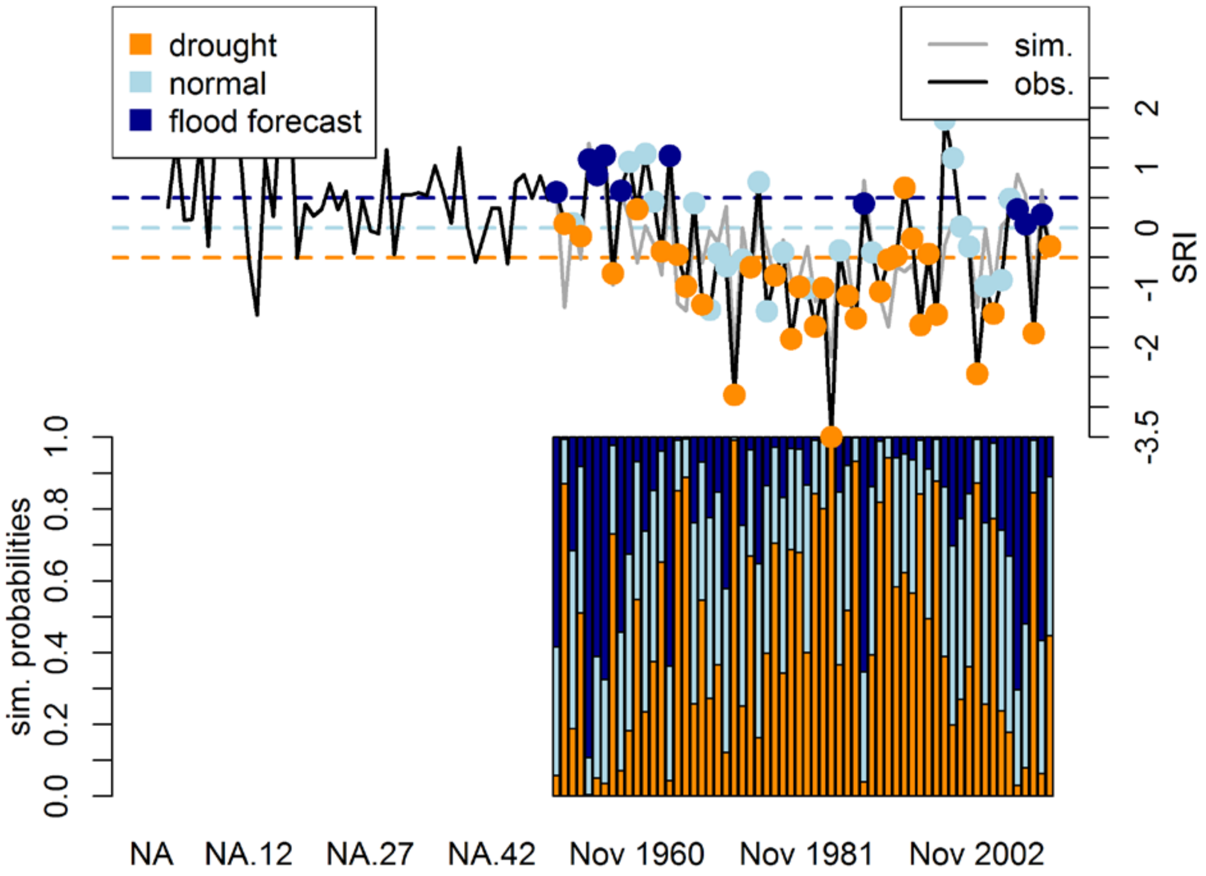

Figure 6-15: One month lead time forecast of late rainy season runoff (SRI_{SON}) at station Khartoum: Early warnings of the multiple linear model with interaction. Above: simulation (grey line) and observed values (black line) with early warnings one month ahead for class with highest probability (coloured points). Below: Probabilities for flood (dark blue), normal (bright blue) and drought (orange).

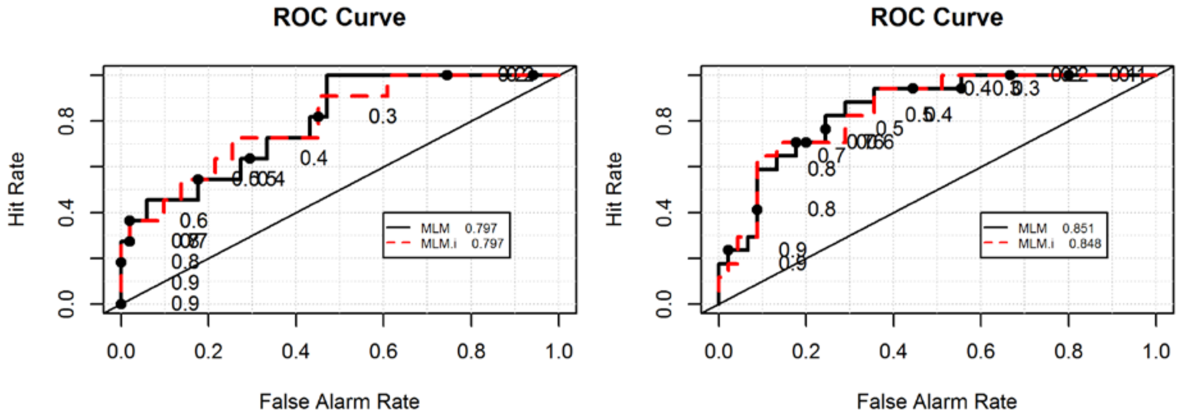

Figure 6-16: Receiver operating characteristic curves of drought early warning with the linear models with and without interaction of one month lead time left for early rainy season runoff (JJA) and right for late rainy season runoff (SON), values next to the model names in the legend show ROC scores.

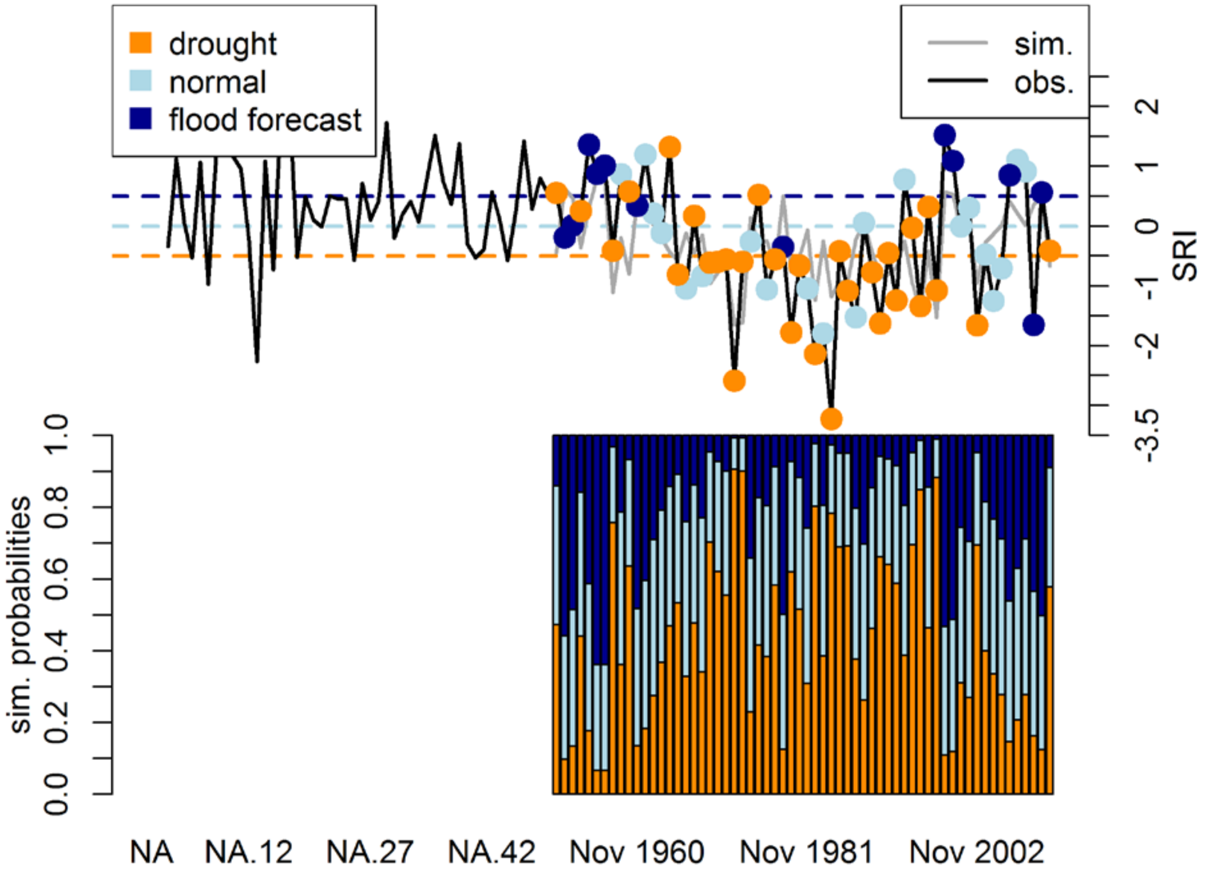

Figure 6-17: Three months lead time forecast of the whole rainy season runoff (SRI_{JJASON}) at station Khartoum: Early warnings of the multiple linear model with interaction. Above: simulation (grey line) and observed values (black line) with early warnings three months ahead for class with highest probability (coloured points). Below: Probabilities for flood (dark blue), normal (bright blue) and drought (orange).

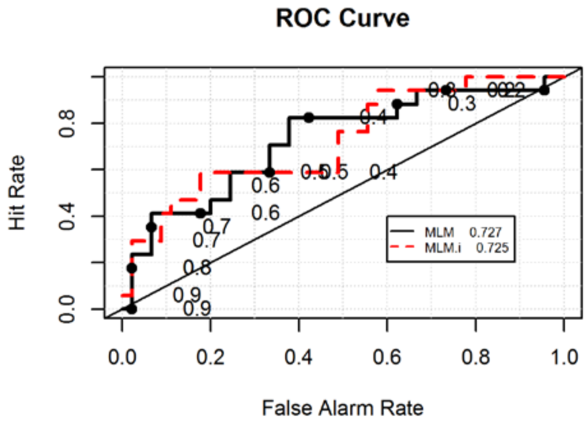

Figure 6-18: Receiver operating characteristic curves of drought early warning with the linear models of three month lead time rainy season runoff (JJASON), values next to the model names in the legend show ROC scores.

6.6 CONCLUSION

The influence of El Niño anomalies on the drought occurrence in Ethiopia and the Blue Nile is known but the relationship is highly complex. By analysis of the signal properties of runoff and the Oceanic Nino index we showed that the two time series share signal properties of longer periods of ca. 16 years. Shorter periods are also common to both series but non-stationary. Both signals are linked but the non-stationarity is an obstacle for statistical seasonal prediction, since statistical models are not able to account for this degree of complexity. The statistical approach presented here was followed to investigate the forecasting quality which can be achieved by building solely upon teleconnections of sea surface temperatures to model runoff in the Blue Nile at the station in Khartoum. The statistical models used several predictors amongst which was the relationship to El Nino, sea surface temperature at the Atlantic shore of Angola, the Red Sea, the Mediterranean Sea and the Indian Ocean.

Three different forecasting schemes were set up with statistical models for the Blue Nile station in Khartoum. The best forecasting skill was achieved for one month ahead forecasts of runoff in the late rainy season from September to November. Forecasts for the early rainy season at one month lead time had lower skill and so did the forecasting models of the whole rainy season at three month lead time. The two latter forecasting schemes reached equally low skills even though they differed in the leading time by two month. This indicated that the predictability does depend on the leading time but also on the time of the season. The predictability for June to August runoff was lower than for September to April in this study.

Due to the low forecasting performance the statistical approach presented here is not suited for operational early warning for the public and can only serve well for specialists and academia. There are two potential reasons for the low prediction performance. First, there are other statistical methods which might be able to reach higher performances. Second, it is possible that for runoff forecasts the hydrological processes cannot be discarded even at the longer time scales. This could be assessed by comparing the statistical forecasting results to a dynamic physical based model approach.

7. REFERENCES

Abtew W, Melesse AM, Dessalegne T (2009) El Niño Southern Oscillation link to the Blue Nile River Basin hydrology. Hydrol Process. doi:10.1002/hyp.7367.

Adler, R.F. and Negri, A.J., 1988. A satellite infrared technique to estimate tropical convective and stratiform rainfall. Journal of Applied Meteorology, 27(1): 30-51.

Amarasekera, K.N., Lee, R.F., Williams, E.R. and Eltahir, E.A.B., 1997. ENSO and the natural variability in the flow of tropical rivers. Journal of Hydrology, 200(1): 24-39.

Arkin, P.A., 1979. The relationship between fractional coverage of high cloud and rainfall accumulations during GATE over the B-Scale array. Monthly Weather Review 107: 1382-1387.

Arnell, N.W., Hudson, D.A. and Jones, R.G., 2003. Climate change scenarios from a regional climate model: Estimating change in runoff in southern Africa. Journal of Geophysical Research-Atmospheres, 108(D16): -.

Barrett, C.B. et al., 1989. Towards an operational system for the use of AVHRR data in Pakistan, Remote Sensing for Operational Applications - Technical Contents of the 15th Annual Conference. Remote Sensing Society, Bristol, UK.

Bellerby, T.J. and Barrett, E.C., 1993. Progressive Refinement - a Strategy for the Calibration by Collateral Data of Short-Period Satellite Rainfall Estimates. Journal of Applied Meteorology, 32(8): 1365-1378.

Cane, M.A., 2005. The evolution of El NiÃ±o, past and future. Earth and Planetary Science Letters, 230(3): 227-240.

Collins, M. et al., 2010. The impact of global warming on the tropical Pacific Ocean and El NiÃ±o. Nature Geoscience, 3(6): 391-397.

Cong, S. and Schaake, J., 1995. The Nile Inverse Distance Method and its Comparison with the Weiner-Kolmogorov Method. No. 0033.1, Nile Forecast Center, Ministry of Water Resources and Irrigation, Cairo, Egypt.

Conway, D., 2000. The Climate and Hydrology of the Upper Blue Nile River. The Geographical Journal, 166(1): 49-62.

Conway, D. and Hulme, M., 1993. Recent fluctuations in precipitation and runoff over the Nile sub-basins and their impact on main Nile discharge. Climatic Change, 25(2): 127-151.

Dezman, L. E., Shafer, B. A., Simpson, H. D. and Danielson, J. A., (1982), ”Development of Surface Water Supply Index- A Drought Severity indicator for Colorado”, Int. Symp. Hydrometeorology, proc., American Water Resource Association (AWRA), Bethesda, Md., 337-341.

DEWFORA project, “White Paper for Definition of Drought Vulnerability Across Africa” WP3, D3.1. April, 2012.

Dickinson, R.E., Henderson-Sellers, A., Kennedy, P.J. and Wilson, M.F., 1993. Biosphere–atmosphere transfer scheme (BATS) version 1e as coupled to the NCAR Community Climate Model. NCAR Tech. Note, NCAR/TN387+ STR.

Dracup, J.A., Lee, K. and Paulson, E.G., 1980. On the definition of droughts. Water Resources Research, 16: 297-302.

Elshamy, M.E., 2008. Assessing the Hydrological Performance of the Nile Forecast System in Long Term Simulations. Nile Basin Scientific Magazine, 1: 22-36.

Elshamy, M.E., Seierstad, I.A. and Sorteberg, A., 2009. Impacts of climate change on Blue Nile flows using bias-corrected GCM scenarios. Hydrol. Earth Syst. Sci., 13(5): 551-565.

Elshamy, M.E.A.M., 2006. Improvement of the Hydrological Performance of Land Surface Parameterization: An Application to the Nile Basin. PhD Thesis Thesis, Imperial College, University of London, London.

Eltahir, E.A.B., 1996. El NiÃ±o and the natural variability in the flow of the Nile River. Water Resources Research, 32(1): 131-137.

Emanuel, K., 1991. A scheme for representing cumulus convection in large-scale models. Journal of the atmospheric sciences, 48(21): 2313–2335.

ENTRO, 2007. Transboundary Analysis Abay-Blue Nile sub-Basin, Eastern Nile Technical Regional Office, Nile Basin Initiative, Addis Ababa.

Fink, A.H. et al., 2004. The 2003 European summer heatwaves and drought-synoptic diagnosis and impacts. Weather, 59(209-216).

Fischlin, A. et al., 2007. Ecosystems, their properties, goods, and services. In: M.L. Parry, O.F. Canziani, P.J. Palutikof, P.J. van der Linden and C.E. Hanson (Editors), Climate Change 2007: Impacts, Adaptation and Vulnerability. Contribution of Working Group II to the Fourth Assessment Report of the Intergovernmental Panel on Climate Change. Cambridge University Press, Cambridge, pp. 211-272.

Garen, D.C., 1993. Revised Surface Water Supply Index for Western United States. ASCE Journal.

Garen, D.C., 2011. The Surface Water Supply Index Formulation and Issues, World Meteorological Organization workshop on hydrological drought indices Geneva, Switzerland, September, 2011.

Giorgi, F. et al., 2012. RegCM4: model description and preliminary tests over multiple CORDEX domains. Climate Research, 2: 7.

Giorgi, F., Marinucci, M.R. and Bates, G.T., 1993a. Development of a second-generation regional climate model (RegCM2). Part I: Boundary-layer and radiative transfer processes.

Gordon, C. et al., 2000. The simulation of SST, sea ice extents and ocean heat transports in a version of the Hadley Centre coupled model without flux adjustments. Climate Dynamics, 16: 147-168.

Green-Newby, J.L., 1992. Nile Hydrid Technique for Version 2.0. No. 0074, Nile Forecast Center, Ministry of Water Resources and Irrigation, Cairo, Egypt.

Green-Newby, J.L., 1993. Satellite Rainfall Estimation Techniques. No. 0075, Nile Forecast Center, Ministry of Water Resources and Irrigation, Cairo, Egypt.

Grell, G.A., 1993. Prognostic evaluation of assumptions used by cumulus parameterizations. Monthly Weather Review;(United States), 121(3).

Holtslag, A.A.M., De Bruijn, E.I.F. and Pan, H.L., 1990. A high resolution air mass transformation model for short-range weather forecasting. Monthly Weather Review, 118(8).

Hurst, H.E., 1950. The Hydrology of the Spbat and White Nile and the Topography of the Blue Nile and Atbara. The Nile Basin, vol. VIII. Government Press, Cairo.

Jansen, E. et al., 2007. Chapter 6. Palaeoclimate. Climate Change 2007: The Physical Science Basis. Contribution of Working Group I to the Fourth Assessment Report of the Intergovernmental Panel on Climate Change: 443-498.

Jones, R.G., Murphy, J.M. and Noguer, M., 1995. Simulation of Climate-Change over Europe Using a Nested Regional-Climate Model .1. Assessment of Control Climate, Including Sensitivity to Location of Lateral Boundaries. Quarterly Journal of the Royal Meteorological Society, 121(526): 1413-1449.

Jury, M.R., 2004. The coherent variability of African river flows: Composite climate structure and the Atlantic circulation. Water Sa, 29(1): 1-10.

Kiehl, J. et al., 1996. Description of the near community climate model (ccm3), National Center for Atmospheric Research.

Knutti, R., Furrer, R., Tebaldi, C., Cermak, J. and Meehl, G.A., 2009. Challenges in Combining Projections from Multiple Climate Models. Journal of Climate, 23(10): 2739-2758.

Lee, T. and McPhaden, M.J., 2010. Increasing intensity of El NiÃ±o in the central-equatorial Pacific. Geophysical Research Letters, 37(14): L14603.

Manoj K., “HYDROLOGICAL DROUGHT INDICES”, Water Technology Centre Indian Agricultural Research Institute New Delhi, INDIA, 2011.

Mckee, T.B., Doesken, N.J. and Kleist, J., 1993. The relationship of drought frequency and duration to time scales, Eight Conference on Applied Climatology, Anahaim, California, pp. 179-184.

McKee, T.B., N.J., D. and Kleist, J., 1995. Drought monitoring with multiple time scales, American Meteorological Society, Boston, pp. 233-236.

Meehl, G.A., Karl, T., Easterling, D.R. and Changnon, S., 2000. An introduction to trends in extreme weather and climate events: observations, socioeconomic impacts, terrestrial ecological impacts, and model projections. Bulletin of the American Meteorological Society, 81: 413-416.

Milford, J.R. and Dugdale, G., 1990. Estimation of rainfall using geostationary satellite data. In: M.D. Steven and J.A. Clark (Editors), Applications of remote Sensing in Agriculture. Proceedings of the 48th Easter School in Agriculture Science, University of Nottingham, Butterworth, London, pp. 97-110.

Mitchell, T.D. and Jones, P.D., 2005. An improved method of constructing a database of monthly climate observations and associated high-resolution grids. International Journal of Climatology, 25(6): 693-712.

Murphy, J.M. et al., 2009. UK Climate Projections Science Report: Climate change projections, Met Office Hadley Centre, Exeter, UK.

Nalbantis, I. and Tsakiris, G., 2009. Assessment of hydrological drought revisited. Water Resources Management, 23(5): 881-897.

New, M., Hulme, M. and Jones, P., 1999. Representing Twentieth-Century Space-Time Climate Variability. Part I: Development of a 1961-90 Mean Monthly Terrestrial Climatology. Journal of Climate, 12(3): 829-856.

New, M., Hulme, M. and Jones, P., 2000. Representing Twentieth-Century Space-Time Climate Variability. Part II: Development of 1901-96 Monthly Grids of Terrestrial Surface Climate. Journal of Climate, 13(13): 2217-2238.

Nicholls, N. and Katz, R.W., 1991. Tele-connections and their implications for long range forecasts. In: M.H. Glantz, R.W. Katz and N. Nicholls (Editors), Teleconnections Linking Worldwide Climate Anomalies: Scientific Basis and Societal Impact. Cambridge Univ. Press, Cambridge, U.K., pp. 511– 525.

Nicholson, S.E., 2001. Climatic and environmental change in Africa during the last two centuries. Climate Research, 17: 123-144.

Nile Forecast Center, 1999a. NFS Operational Manual: Part (4) Rainfall Estimation, Ministry of Water Resources and irrigation, Cairo, Egypt.

Nile Forecast Center, 1999b. NFS Operational Manual: Part (5) Hydrological Modeling of the Nile Basin, Ministry of Water Resources and irrigation, Cairo, Egypt.

Nile Forecast Center, 2007. Nile Forecasting System software version 5.1, Ministry of Water Resources and irrigation, Cairo, Egypt.

Obasi, G.O.P., 1994. WMO`s role in the international decade for natural disaster reduction. Bulletin of the American Meteorological Society, 75: 1655-1661.

Palmer, W. C., 1965: Meteorologic drought. U.S. Weather Bureau, Res. Pap. No. 45, 58 pp.

NASA Goddard Institute for Space Studies. (2008, December 16). Global Temperature Trends: 2008 Annual Summation. Accessed January 20, 2009.

Power, S.B. and Smith, I.N., 2007. Weakening of the Walker Circulation and apparent dominance of El NiÃ±o both reach record levels, but has ENSO really changed? Geophysical Research Letters, 34(18): L18702.

Redmond, K.T., 2002. The depiction of drought. Bulletin of the American Meteorological Society, 83: 1143-1147.

Reynolds, R.W. et al., 2007. Daily high-resolution-blended analyses for sea surface temperature.

Seneviratne, S.I. et al., 2012. Changes in climate extremes and their impacts on the natural physical environment. Managing the Risks of Extreme Events and Disasters to Advance Climate Change Adaptation: 109-230.

Shafer, B.A. and Dezman, L.E., 1982. Development of a Surface Water Supply Index (SWSI) to Assess the Severity of Drought Snowpack Runoff Areas, Western Snow Conference. Colorado State University, Fort Collins, Colorado, pp. 164-175.

Shahin, M., 1985. Hydrology of the Nile Basin. Developments in water science ; 21. Elsevier, Amsterdam ; Oxford.

Shukla, S. and Wood, A.W., 2008. Use of a standardized runoff index for characterizing hydrolog ic drought. Geophys. Res. Letters., 35: L02405.

Sorooshian, S. and Dracup, J.A., 1980. Stochastic Parameter-Estimation Procedures for Hydrologic Rainfall-Runoff Models - Correlated and Heteroscedastic Error Cases. Water Resources Research, 16(2): 430-442.

'http://www.emdat.be/maps2010','84.36.81.132',1371377238)in/var/www/vhosts/emdat.be/httpdocs/includes/database.mysqli.inc on line 128.

Sutcliffe, J.V. and Parks, Y.P., 1999. The hydrology of the Nile. IAHS Special Publication No. 5. International Association of Hydrological Sciences, Wallingford, UK.

Teferi, E., Uhlenbrook, S., Bewket, W., Wenninger, J. and Simane, B., 2010. The use of remote sensing to quantify wetland loss in the Choke Mountain range, Upper Blue Nile basin, Ethiopia. Hydrol. Earth Syst. Sci. Discuss, 7: 6243-6284.

UN, 2008. Trends in sustainable development. Agriculture, rural development, land, desertification and drought, Department of Economic and Social Affairs, United Nations, New York.

Uppala, S. et al., 2004. ERA-40: ECMWF’s 45-year reanalysis of the global atmosphere and surface conditions 1957-2002. ECMWF Newsletter, 101: 2-21.

Vecchi, G.A. and Wittenberg, A.T., 2010. El NiÃ±o and our future climate: where do we stand? Wiley Interdisciplinary Reviews: Climate Change, 1(2): 260-270.

Wang, G. and Eltahir, E.A.B., 1999. Use of ENSO information in medium-and long-range forecasting of the Nile floods. Journal of Climate, 12(6): 1726-1737.

Wilhite, D.A., 1993. Drought assessment, management and planning: Theory and case studies. Kluwer, Boston.

Willmott, C.J. and Robeson, S.M., 1995. Climatologically Aided Interpolation (CAI) of Terrestrial Air-Temperature. International Journal of Climatology, 15(2): 221-229.

Wittenberg, A.T., 2009. Are historical records sufficient to constrain ENSO simulations? Geophysical Research Letters, 36(12): L12702.

Wood, A.W., Lettenmaier, D.P. and Palmer, R.N., 2000. Reply to comment by Kirshen on 'Assessing climate change implications for water resources planning'. Climatic Change, 44(4): 539-541.

Yeh, S.W. et al., 2009. El Niño in a changing climate. Nature, 461(7263): 511-514.